View metadata, citation and similar papers at core.ac.uk

brought to you by CORE

provided by KITopen

PHYSICAL REVIEW D **90,** 052004 (2014)

Measurement of the Higgs boson mass from the $H \to \gamma\gamma$ and $H \to ZZ^* \to 4\ell$ channels in pp collisions at center-of-mass energies of 7 and 8 TeV with the ATLAS detector

G. Aad *et al.*[*]

(ATLAS Collaboration)

(Received 17 June 2014; published 9 September 2014)

An improved measurement of the mass of the Higgs boson is derived from a combined fit to the reconstructed invariant mass spectra of the decay channels $H \to \gamma\gamma$ and $H \to ZZ^* \to 4\ell$. The analysis uses the pp collision data sample recorded by the ATLAS experiment at the CERN Large Hadron Collider at center-of-mass energies of 7 TeV and 8 TeV, corresponding to an integrated luminosity of 25 fb^{-1}. The measured value of the Higgs boson mass is $m_H = 125.36 \pm 0.37(\text{stat}) \pm 0.18(\text{syst})$ GeV. This result is based on improved energy-scale calibrations for photons, electrons, and muons as well as other analysis improvements, and supersedes the previous result from ATLAS. Upper limits on the total width of the Higgs boson are derived from fits to the invariant mass spectra of the $H \to \gamma\gamma$ and $H \to ZZ^* \to 4\ell$ decay channels.

DOI: 10.1103/PhysRevD.90.052004 PACS numbers: 14.80.Bn

I. INTRODUCTION

In 2012, the ATLAS and CMS collaborations published the discovery of a new particle [1,2] in the search for the Standard Model (SM) Higgs boson [3–8] at the CERN Large Hadron Collider (LHC) [9]. In the SM, the Higgs boson mass is not predicted. Its measurement is therefore required for precise calculations of electroweak observables including the production and decay properties of the Higgs boson itself. These calculations are needed to test the coupling structure of the SM Higgs boson, as suggested in Ref. [10] and references therein.

The LHC collaborations have chosen a model-independent approach to measure the Higgs boson mass based on fitting the spectra of the reconstructed invariant masses of the two decay modes $H \to \gamma\gamma$ and $H \to ZZ^* \to 4\ell$.[1] In these two channels the Higgs boson produces a narrow mass peak with a typical experimental resolution of 1.6 GeV to 2 GeV over a smooth background, from which the mass can be extracted without assumptions on the signal production and decay yields. Interference effects are expected between the Higgs boson signal and SM background processes. For the $H \to ZZ^* \to 4\ell$ channel, the impact of this interference on the mass measurement is negligible (< 10 MeV) if the Higgs boson width is close to the SM value [11]. For the $H \to \gamma\gamma$ channel, such effects are larger for widths close to the SM value [12–14], shifting the mass down by a few tens of MeV, but still small compared to the present experimental precision. The interference effects on the mass spectra are neglected in this paper.

Recent measurements of the Higgs boson mass from the ATLAS and CMS collaborations are reported in Refs. [15] and [16]. The ATLAS measurement was based on the same data sample as that analyzed in this paper, corresponding to an integrated luminosity of 4.5 fb^{-1} at $\sqrt{s} = 7$ TeV and of 20.3 fb^{-1} at $\sqrt{s} = 8$ TeV of pp collisions, taken in 2011 and 2012, respectively. The luminosity determination for the 2012 data set has been improved compared to Ref. [15], reaching an accuracy of 2.8% for the 2012 data.

The measurement of the Higgs boson mass is updated in this work with improved analyses of the two channels $H \to \gamma\gamma$ and $H \to ZZ^* \to 4\ell$, as described in Secs. IV and V. The $H \to \gamma\gamma$ channel profits from an improved calibration of the energy measurements of electron and photon candidates, which results in a sizable reduction of the systematic uncertainties on their energy scales. In the $H \to ZZ^* \to 4\ell$ channel both the expected statistical uncertainty and the systematic uncertainty on the mass measurement have been reduced with respect to the previous publication. The improvement of the statistical uncertainty arises primarily from the use of a multivariate discriminant that is designed to increase the separation of the signal from background. The systematic uncertainty reduction comes from both the improved electromagnetic energy calibration and a reduction in the muon momentum scale uncertainty, which was obtained by studying large samples of $Z \to \mu^+\mu^-$ and $J/\psi \to \mu^+\mu^-$ decays.

More information on the general aspects of the $H \to \gamma\gamma$ and $H \to ZZ^* \to 4\ell$ analyses is contained in the concurrent Refs. [17,18], where in particular, the details of the signal and background simulation can be found. The present measurement of the Higgs boson mass relies

[*] Full author list given at the end of the article.

Published by the American Physical Society under the terms of the Creative Commons Attribution 3.0 License. Further distribution of this work must maintain attribution to the author(s) and the published articles title, journal citation, and DOI.

[1] Throughout this paper, the symbol ℓ stands for electron or muon.

 © 2014 CERN, for the ATLAS Collaboration

strongly upon both the calibration of the energy measurement for electrons and photons described in Ref. [19], and the understanding of the muon momentum scale and resolution presented in Ref. [20].

The ATLAS detector [21] is a multipurpose detector with a forward-backward symmetric cylindrical geometry.[2] At small radii, the inner detector (ID), immersed in a 2 T magnetic field produced by a thin superconducting solenoid located in front of the calorimeter, is made up of fine-granularity pixel and microstrip detectors. These silicon-based detectors cover the pseudorapidity range $|\eta| < 2.5$. A gas-filled straw-tube transition radiation tracker (TRT) complements the silicon tracker at larger radii and also provides electron identification based on transition radiation. The electromagnetic (EM) calorimeter is a lead/liquid-argon sampling calorimeter with accordion geometry. The calorimeter is divided into a barrel section covering $|\eta| < 1.475$ and two end-cap sections covering $1.375 < |\eta| < 3.2$. For $|\eta| < 2.5$ it is divided into three layers in depth, which are finely segmented in η and ϕ. A thin presampler layer, covering $|\eta| < 1.8$, is used to correct for fluctuations in upstream energy losses. Hadronic calorimetry in the region $|\eta| < 1.7$ uses steel absorbers and scintillator tiles as the active medium. Liquid argon calorimetry with copper absorbers is used in the hadronic end-cap calorimeters, which cover the region $1.5 < |\eta| < 3.2$. A forward calorimeter using copper or tungsten absorbers with liquid argon completes the calorimeter coverage up to $|\eta| = 4.9$. The muon spectrometer (MS) measures the deflection of muon tracks with $|\eta| < 2.7$, using three stations of precision drift tubes, with cathode strip chambers in the innermost layer for $|\eta| > 2.0$. The deflection is provided by a toroidal magnetic field with an integral of approximately 3 Tm and 6 Tm in the central and end-cap regions of ATLAS, respectively. The muon spectrometer is also instrumented with separate trigger chambers covering $|\eta| < 2.4$.

The outline of this paper is the following. In Secs. II and III, the improvements in the measurement of the physics objects used for the mass measurement (photons, electrons and muons) are described. In Secs. IV and V a brief description of the analyses used to measure the Higgs boson mass in the $H \to \gamma\gamma$ and $H \to ZZ^* \to 4\ell$ channels is presented, with emphasis on the improvements with respect to the analysis published in Ref. [15]. The statistical procedures used for the measurement of the mass and the contributions of the different systematic uncertainties are discussed in Sec. VI. The results of the combined mass measurement and the compatibility of the individual measurements of the two channels are reported in Sec. VII.

[2]ATLAS uses a right-handed coordinate system with its origin at the nominal interaction point (IP) in the center of the detector and the z axis along the beam pipe. The x axis points from the IP to the center of the LHC ring, and the y axis points upward. Cylindrical coordinates (r, ϕ) are used in the transverse plane, ϕ being the azimuthal angle around the beam pipe. The pseudorapidity is defined in terms of the polar angle θ as $\eta = -\ln \tan(\theta/2)$.

II. PHOTON AND ELECTRON RECONSTRUCTION, ENERGY SCALE CALIBRATION AND SYSTEMATIC UNCERTAINTIES

The calibration strategy for the energy measurement of electrons and photons is described in detail in Ref. [19]. In this section, the definitions of photon and electron objects are given, followed by a description of their energy scale calibration. To achieve the best energy resolution and to minimize systematic uncertainties, the calibration and stability of the calorimeter cell energy measurement are optimized, the relative calibration of the longitudinal layers of the calorimeter is adjusted, and a determination of the amount of material in front of the calorimeter is performed. The global calorimeter energy scale is then determined *in situ* with a large sample of $Z \to e^+e^-$ events, and verified using $J/\psi \to e^+e^-$ and $Z \to \ell^+\ell^-\gamma$ events. The calibration analysis uses a total of 6.6 million $Z \to e^+e^-$ decays, 0.3 million $J/\psi \to e^+e^-$ decays, and 0.2 million radiative Z boson decays. Compared to the previous publication [15], the uncertainties in the calibration are significantly reduced by using data-driven measurements for the intercalibration of the calorimeter layers and for the estimate of the material in front of the calorimeter, as well as by improving the accuracy of the *in situ* calibration with $Z \to e^+e^-$ events [19]. The expected range for transverse energy of photons from $H \to \gamma\gamma$ decays is from 40 GeV to about 100 GeV. The range for electrons from $H \to ZZ^* \to 4\ell$ decays is from 7 GeV to about 50 GeV.

A. Definition of photon and electron objects

Photon and electron candidates are reconstructed from clusters of energy deposited in the EM calorimeter. Candidates without a matching track or reconstructed conversion vertex in the ID are classified as unconverted photon candidates. Candidates with a matching reconstructed conversion vertex or a matching track consistent with originating from a photon conversion are classified as converted photon candidates. Candidates matched to a track consistent with originating from an electron produced in the beam interaction region are kept as electron candidates.

The measurement of the electron or photon energy is based on the energy collected in calorimeter cells in an area of size $\Delta\eta \times \Delta\phi$ of 0.075×0.175 for electrons and converted photons in the barrel, 0.075×0.125 for unconverted photons in the barrel, and 0.125×0.125 for electrons and photons in the end caps. The choice of a different area for electrons and unconverted photons in the barrel is driven by the deflection of charged particles in the magnetic field and

bremsstrahlung in upstream material. A multivariate regression algorithm to calibrate electron and photon energy measurements was developed and optimized using simulation. Corrections are made for the energy deposited in front of the calorimeter (typically between a few % and 20% of the electron energy for 100 GeV energy electrons [21]) and outside of the cluster (around 5%), as well as for the variation of the energy response as a function of the impact point on the calorimeter. The inputs to the energy calibration algorithm are the measured energy per calorimeter layer, including the presampler, η of the cluster, and the local position of the shower within the second-layer cell corresponding to the cluster centroid. In addition, for converted photons, the track transverse momenta and the conversion radius are used as input to the regression algorithm to further improve the energy resolution, especially at low energy. This calibration procedure gives a 10% improvement in the expected mass resolution for $H \to \gamma\gamma$ compared to the calibration used in the previous publication. For electron and photon candidates, the associated tracks are fitted with a Gaussian-sum filter to account for bremsstrahlung energy losses [22]. For $H \to ZZ^* \to 4\ell$ candidates, the resulting momentum measurement is combined with the energy measured in the calorimeter to improve the electron energy measurement, especially at low energy or in the transition region between the barrel and end-cap calorimeters, where the calorimeter and ID have similar resolution.

B. Cell energy calibration and stability

The raw signal from each calorimeter cell is converted into a deposited energy using the electronics calibration of the EM calorimeter [23]. The calibration coefficients are determined periodically using dedicated electronics calibration runs and are stable in time to better than 0.1%. The relative calibration of the different gains used in the readout is investigated by studying the $Z \to e^+e^-$ sample, used for the global energy scale, as a function of the electron energy and categorizing the events according to the electronics gain used for the energy measurement, and small corrections (typically less than a few per mille) are applied. The corrections applied to the few percent of channels operated at non-nominal high voltage values are verified using data. The stability of the calorimeter response for data, both as a function of time and of instantaneous luminosity, is monitored using electrons from W or Z decays and is found to be better than 0.05%.

C. Intercalibration of the different calorimeter layers

Accurate relative intercalibration of the different layers of the EM calorimeter is critical to achieve good linearity of the energy response. The relative calibration of the first two layers of the EM calorimeter, which contain most of the energy deposited by electrons and photons, is performed using muons from Z boson decays by comparing their measured energy loss in data and simulation. The use of muons allows the determination of the intrinsic relative layer calibration, independently of uncertainties on the material in front of the EM calorimeter. Small corrections, around 2% on average, for the relative calibration of the two layers are derived. The uncertainty on the relative calibration of the first two layers of the EM calorimeter varies between 1% and 2% as a function of η and is dominated by the uncertainties on the exact amount of liquid argon traversed by the muons and by the accuracy of the simulation of the cross-talk between calorimeter cells. The relative calibration of the presampler layer is derived from electrons, by comparing the presampler energy in data and simulation as a function of the longitudinal shower development measured in the calorimeter. The accuracy of this calibration, which does not depend on knowledge of the material in front of the presampler, is better than 5%.

D. Determination of the material in front of the EM calorimeter

Accurate knowledge of the material in front of the EM calorimeter is required to properly correct for the energy lost upstream of the calorimeter, which also depends on the nature of the particle (electron, unconverted photon, converted photon) and its energy. The total amount of material in front of the presampler layer varies from two radiation lengths (for $|\eta| < 0.6$) to about five radiation lengths (for $|\eta| \sim 1.7$). The amount of material in front of the calorimeter is verified using collision data by studying the longitudinal development of electromagnetic showers, measured using the first two layers of the calorimeter, which are intercalibrated as described above, without any assumption about the material in front of the calorimeter. The uncertainties given below result from the statistical accuracy of the data and from the uncertainties in the modeling of the longitudinal shower profiles in the calorimeter.

The material between the presampler and the first calorimeter layer is measured using unconverted photons with low energy deposition in the presampler. Comparison of data and simulation shows that this material is well described in the simulation with an accuracy between 0.03 and 0.05 radiation lengths.

The integral of the material in front of the presampler is determined using the difference between electron and unconverted photon longitudinal shower profiles. The accuracy of this measurement is between 0.02 and 0.10 radiation lengths, depending on η. Over most of the calorimeter acceptance, the simulation is found to reproduce the data well, after some improvements in the description of the material in front of the end-cap calorimeter, with the exception of a few small localized regions where differences of up to 0.3 radiation lengths remain. The relative calibration of electron and photon energy measurements also depends on the radial position of detector

material in front of the presampler, which cannot be directly probed using longitudinal shower profiles measured in the calorimeter. The uncertainty on the amount of material in the ID active area is estimated from a comparison between a bottom-up inventory of the ID components and the measured weight of different ID subdetector units [21]. A 5% relative uncertainty, corresponding to 0.02 to 0.10 radiation lengths depending on the detector region, in the amount of material in the ID active area is derived from this comparison. Measurement of the rates of hadronic interactions [24] and of photon conversions with collision data are consistent with (albeit less precise than) this *a priori* knowledge. The determination of the integral of the material in front of the presampler is then used together with knowledge of the material in the ID active area to constrain the material in the detector services beyond the active part of the ID and in the calorimeter cryostats.

E. Global calorimeter energy scale adjustment

The global calorimeter energy scale is determined from $Z \to e^+e^-$ decays by comparing the reconstructed mass distributions in data and simulation. This is done in bins of η of the electrons. The energy scale correction factors are typically of the order of 1%–3% and are consistent with the uncertainties on the initial energy scale derived from test-beam data. The uncertainty in the measurement of these factors from the Z sample is less than 0.1% on average, and up to 0.3% for $|\eta| \sim 1.5$ at the transition region between the barrel and end-cap calorimeters. The uncertainty is significantly reduced compared to Ref. [25], owing to the improved detector description discussed above, to improved simulation, to the intercalibration corrections, and to a larger Z boson decay sample. No variation of the energy scale correction factors with pileup was observed. At the same time, an effective constant term for the calorimeter energy resolution is extracted by adjusting the width of the reconstructed Z mass distribution in simulation to match the distribution in data. This constant term is, on average, 0.7% for $|\eta| < 0.6$, and between 0.7% and 1.5% in the remainder of the calorimeter acceptance, except in the transition region between barrel and end-cap calorimeters where it is 3.5% and at the end of the end-cap acceptance ($|\eta| > 2.3$) where it is 2.5%. This constant term is used to adjust the energy resolution in simulated samples. The extraction of the energy scale and of the effective constant term is done separately for the 7 TeV and 8 TeV data. The effective constant term is about 0.2%–0.3% larger in the 8 TeV data.

F. Systematic uncertainties on the energy scale and cross-checks

The calorimeter energy scale adjustment with Z events determines the scale for electrons with transverse energy (E_{T}) close to that of $Z \to e^+e^-$ events ($E_{\mathrm{T}} \sim 40$ GeV on average). Any systematic uncertainty thus has minimal impact for 40 GeV E_{T} electrons but can lead to residual nonlinearities and differences between the electron, unconverted photon, and converted photon energy scales.

In addition to the uncertainty on the overall energy scale adjustment, the uncertainties affecting the energy measurement of electrons and photons can be classified as follows. The impact of these systematic uncertainties on the photon energy scale is detailed for photons from Higgs boson decays, as the impact of energy scale systematic uncertainties is larger for this decay channel.

(i) Uncertainty on the nonlinearity of the energy measurement at the cell level: this arises mostly from the relative calibration of the different gains used in the calorimeter readout. The uncertainty on the nonlinearity of the cell energy calibration contributes an uncertainty of about 0.1% to the energy scale of photons from Higgs boson decays (up to 1% for $1.5 < |\eta| < 1.7$).

(ii) Uncertainty on the relative calibration of the different calorimeter layers: these contribute an uncertainty of about 0.10% to 0.15% to the energy scale of photons from Higgs boson decays.

(iii) Uncertainty on the amount of material in front of the calorimeter: these contribute between 0.1% and 0.3% as a function of η for unconverted photons from Higgs boson decays. This uncertainty is typically 2 times smaller for converted photons that have an energy loss before the calorimeter closer to that of the Z decay electrons used in the energy scale adjustment.

(iv) Uncertainty in the reconstruction of photon conversions: unconverted and converted photons are calibrated differently to take into account the difference in the energy loss before the calorimeter. Converted photons misidentified as unconverted photons, or vice versa, are typically reconstructed with an energy shifted by 2%. The uncertainty in the modeling of the efficiency to properly classify converted or unconverted photons is a few percent. This translates into an uncertainty on the photon energy scale of 0.02%–0.04% for both the converted and unconverted photons.

(v) Uncertainty in the modeling of the lateral shower shape: differences between data and simulation for the lateral development of electromagnetic showers contribute to the uncertainty on the energy scale if they depend on energy or particle type. These differences are compared for photons and electrons using a sample of radiative Z decays. They are found to be consistent. The resulting uncertainty on the photon energy scale is 0.05%–0.3% depending on η and whether or not the photon converted.

At an E_{T} of about 60 GeV, the total uncertainty on the photon energy scale is between 0.2% and 0.3% for $|\eta| < 1.37$ or $|\eta| > 1.82$; for $1.52 < |\eta| < 1.82$, the uncertainty

is 0.9% and 0.4% for unconverted and converted photons, respectively. The energy dependence of the photon energy scale uncertainty is weak. The uncertainty on the electron energy scale at an E_T of 40 GeV is, on average, 0.04% for $|\eta| < 1.37$, 0.2% for $1.37 < |\eta| < 1.82$ and 0.05% for $|\eta| > 1.82$. At an E_T of about 10 GeV, the electron energy scale uncertainty ranges from 0.4% to 1% for $|\eta| < 1.37$, is about 1.1% for $1.37 < |\eta| < 1.82$, and again 0.4% for $|\eta| > 1.82$. The largest uncertainty for electrons is in the transition region between the barrel and end-cap calorimeters, which is not used for photons. These uncertainties are modeled using 29 independent sources to account for their η dependence, and are almost fully correlated between the 7 TeV and 8 TeV samples. These 29 uncertainty sources are assigned in the following way:

(i) one for the uncertainty in the extraction of the calorimeter energy scale from $Z \to e^+e^-$ events,
(ii) three for the uncertainty on the nonlinearity of the energy measurement at the cell level,
(iii) four for the uncertainty on the ID material in different eta regions,
(iv) six for the uncertainties affecting the relative calibration of the different calorimeter layers covering uncertainties in the muon measurement as well as in the modeling of muon energy loss in the simulation,
(v) ten for the uncertainties affecting the determination of the material after the ID volume and between the presampler and the first calorimeter layer covering uncertainties in the data measurement and in the modeling of longitudinal shower profiles in the simulation,
(vi) three for uncertainties in the modeling of the conversion reconstruction performance in the simulation,
(vii) two for the uncertainties in the modeling of the lateral shower shapes, separating converted and unconverted photons.

An independent verification of the energy scale is performed using samples of $J/\psi \to e^+e^-$ and $Z \to \ell^+\ell^-\gamma$ decays. The latter sample allows, for instance, a direct measurement of the photon energy scale in the low transverse energy range (typically between 7 GeV and 35 GeV). The results are in good agreement with the energy scale determined from the $Z \to e^+e^-$ sample, taking into account the systematic uncertainties discussed above. With the $Z \to \ell^+\ell^-\gamma$ sample, the energy scale of photons with

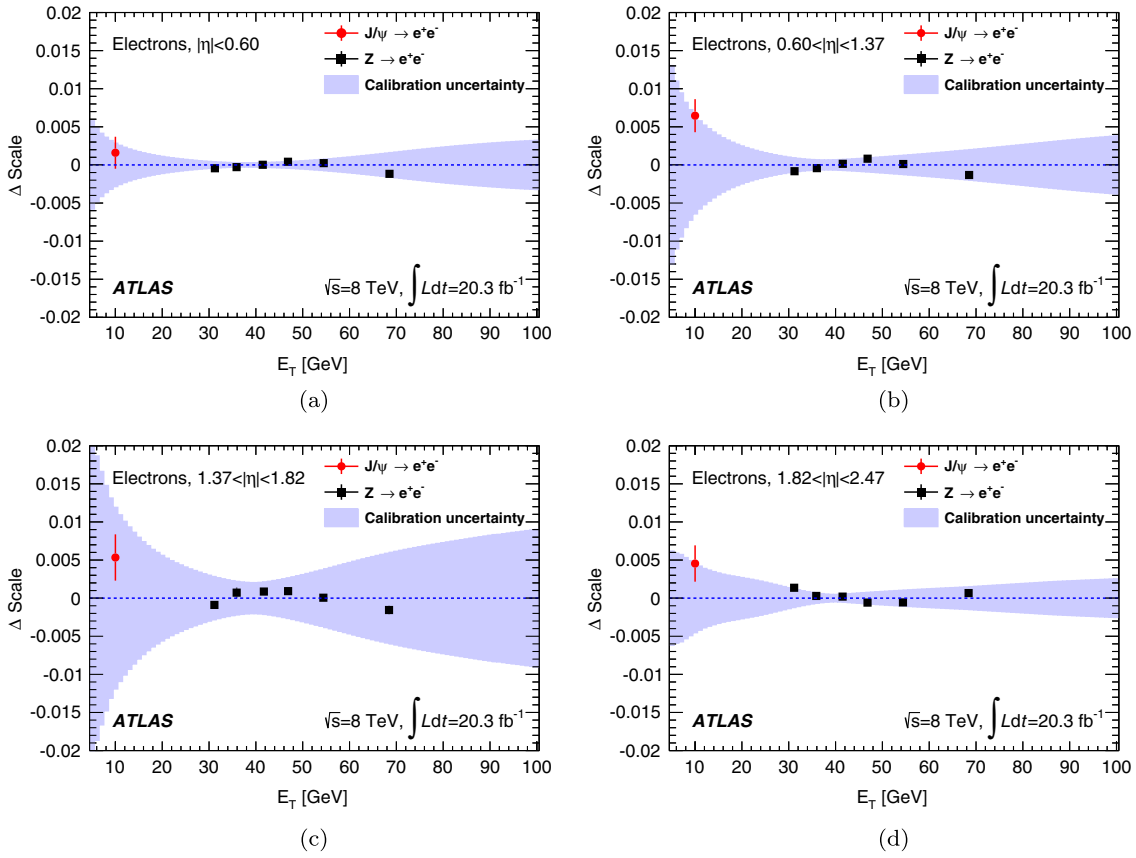

FIG. 1 (color online). Relative scale difference, Δ Scale, between the measured electron energy scale and the nominal energy scale, as a function of E_T using $J/\psi \to e^+e^-$ and $Z \to e^+e^-$ events (points with error bars), for four different η regions: (a) $|\eta| < 0.6$, (b) $0.6 < |\eta| < 1.37$, (c) $1.37 < |\eta| < 1.82$ and (d) $1.82 < |\eta| < 2.37$. The uncertainty on the nominal energy scale for electrons is shown as the shaded area. The error bars include the systematic uncertainties specific to the $J/\psi \to e^+e^-$ measurement.

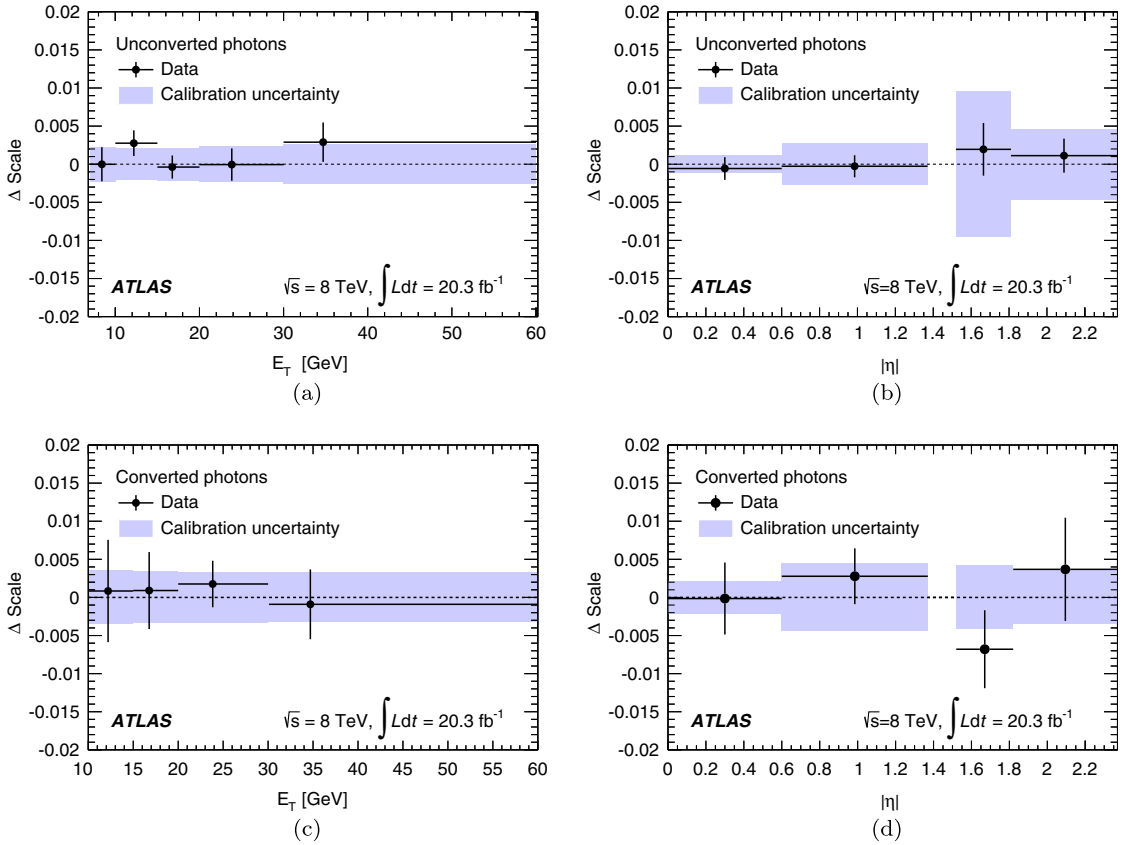

FIG. 2 (color online). Relative scale difference, Δ Scale, between the measured photon energy scale using $Z \to \ell\ell\gamma$ events and the nominal energy scale: (a) as a function of E_{T} for unconverted photons, (b) as a function of η for unconverted photons, (c) as a function of E_{T} for converted photons and (d) as a function of η for converted photons. Photons reconstructed in the transition region between the barrel and end-cap calorimeters are not considered. The $Z \to \ell\ell\gamma$ measurements are the points with error bars. The uncertainty on the nominal energy scale for photons is shown as the shaded area. The error bars include the systematic uncertainties specific to the $Z \to \ell\ell\gamma$ measurement.

transverse energy around 30 GeV is probed with an accuracy of about 0.3%. Figures 1 and 2 summarize the verifications of the electron and photon energy scales from these samples using the 8 TeV data set, after the full calibration procedure is applied. In addition to the $J/\psi \to e^+e^-$ and $Z \to \ell^+\ell^-\gamma$ samples, the nonlinearity in the electron energy scale is also probed by dividing the $Z \to e^+e^-$ sample into bins of electron E_{T}. These figures also show the total systematic uncertainty on the electron and photon energy scales as a function of E_{T} and η. The same verifications are performed using the 7 TeV data set with results consistent within uncertainties.

G. Uncertainties on the calorimeter energy resolution

Systematic uncertainties on the calorimeter energy resolution arise from uncertainties in the modeling of the sampling term and on the measurement of the constant term in Z boson decays, from uncertainties related to the amount of material in front of the calorimeter, which affect electrons and photons differently, and from uncertainty in the modeling of the small contribution to the resolution from fluctuations in the pileup from other proton-proton interactions in the same or neighboring bunch crossings. The uncertainty on the calorimeter energy resolution is typically ~10% for photons from Higgs boson decays, and varies from 10% to 5% for electrons in the E_{T} range from 10 GeV to 45 GeV.

III. MUON RECONSTRUCTION, MOMENTUM SCALE AND RESOLUTION SYSTEMATIC UNCERTAINTIES

The muon momentum is measured independently by the ID and the MS detector systems. Four types of muon candidates are reconstructed, depending on the available information from the ID, the MS, and the calorimeters. Most muon candidates are identified by matching a reconstructed ID track with either a complete or a partial (local segment) track reconstructed in the MS [20,26]. If a complete MS track is present, the two independent momentum measurements are combined (CB muons); otherwise the momentum is measured using the ID, and the partial MS track serves as identification (segment-tagged muons). The muon reconstruction and identification coverage is extended by using tracks reconstructed in the

forward region ($2.5 < |\eta| < 2.7$) of the MS, which is outside the ID coverage (standalone muons). The parameters of the muon track reconstructed in the MS are expressed at the interaction point by extrapolating the track back to the point of closest approach to the beam line, taking into account the energy loss of the muon in the calorimeters. In the center of the barrel region ($|\eta| < 0.1$), which lacks MS geometrical coverage, ID tracks with transverse momentum $p_{\mathrm{T}} > 15$ GeV are identified as muons if their calorimetric energy deposits are consistent with a minimum ionizing particle (calorimeter-tagged muons). The combination of the track measurements provided by the ID and MS ensures excellent momentum resolution across 3 orders of magnitude, from a few GeV up to a few TeV.

The muon reconstruction in simulation is corrected to match the momentum scale and resolution measured from collision data as described in detail in Ref. [20]. About 6 million $J/\psi \to \mu^+\mu^-$ events[3] and about 9 million $Z \to \mu^+\mu^-$ events were used to extract the corrections to be applied to the simulated data. They consist of scale corrections for the ID and MS, a p_{T}-independent momentum correction for the MS and a p_{T}-dependent smearing correction to be applied to reproduce the resolution observed in data. The corrections for the ID and MS momentum measurements were derived separately. For the momentum of CB muons, the individual corrections from the ID and MS momentum are combined according to their relative weight in the measurement of the combined muon.

To extract the ID corrections, template fits to the $J/\psi \to \mu^+\mu^-$ and $Z \to \mu^+\mu^-$ invariant mass distributions are performed in bins of η and p_{T}. The MS corrections are extracted by fitting the $J/\psi \to \mu^+\mu^-$ and $Z \to \mu^+\mu^-$ invariant mass distributions and the difference between the momentum measured in the ID and MS. The MS corrections are derived in bins of p_{T} and η, and follow the sector granularity of the MS in the azimuthal coordinate ϕ. The systematic uncertainties on the corrections are estimated by varying several ingredients of the fit procedure: the parametrization and the normalization of the backgrounds, the fit ranges, and the parametrization of the resonances and their kinematic distributions. The systematic uncertainties on the resolution are varied independently for the ID and MS, whereas the ID and MS systematic scale uncertainties are treated as fully correlated, hence maximizing the impact of the scale variation on the CB muons.

The major improvement with respect to the previous publication is the use of $J/\psi \to \mu^+\mu^-$ events in addition to the $Z \to \mu^+\mu^-$ sample in the simulation correction procedure. This allows a significant reduction of the momentum scale uncertainty in the low momentum range that is relevant for the $H \to ZZ^* \to 4\ell$ mass measurement. In previous studies, the $J/\psi \to \mu^+\mu^-$ sample was used only for the evaluation of the systematic uncertainties.

The ID momentum scale corrections are below 0.1%. The systematic uncertainties on the ID scale increase with $|\eta|$, starting from 0.02% at $\eta = 0$ and rising to about 0.2% for $|\eta| > 2$. The MS scale corrections vary from −0.4% to +0.3% depending on the η and ϕ regions. The p_{T}-independent momentum correction to the MS measurement takes into account the difference between the muon energy loss in the calorimeters in data and simulation, is of the order of a few tens of MeV and has a negligible impact on the Higgs boson mass measurement. Typical systematic uncertainties on the MS momentum scale range from less than 0.1% to about 0.2%. The systematic uncertainties on the CB momentum scale are 0.04% in the barrel region and increase to about 0.2% for $|\eta| > 2$.

These results were checked by separately fitting the dimuon invariant mass distribution to extract the peak position and the width of the J/ψ, Z and Υ resonances in data and in the simulation, with and without corrections. For this study 17 million J/ψ events were used. The Υ sample, about 5 million events, was not used in the simulation correction procedure and therefore provides an independent validation performed in bins of p_{T}, η and ϕ. Figure 3(a) shows the ratio of the reconstructed dimuon invariant mass for data to the corrected mass in simulation for J/ψ, Υ and Z events as a function of η of the higher-p_{T} muon. Figure 3(b) shows the same ratio as a function of the average transverse momentum, $\langle p_{\mathrm{T}} \rangle$, of the two muons. The error bars on data points show the combined statistical and systematic uncertainties. The systematic uncertainty is extracted by varying the fitted dimuon mass range and, in the case of J/ψ, by taking into account the uncertainty on the background. These studies demonstrate the validity of the corrections and of the associated systematic uncertainties in the range $6 < p_{\mathrm{T}} \lesssim 100$ GeV.

IV. MASS AND WIDTH MEASUREMENT IN THE $H \to \gamma\gamma$ CHANNEL

The $H \to \gamma\gamma$ channel provides good sensitivity to the Higgs boson mass, due to the excellent mass resolution in the diphoton final state, allowing the observation of a narrow mass peak over a smooth background which can be determined directly from data. The EM calorimeter provides a measurement of the photon energy and direction (photon pointing), utilizing its longitudinal segmentation. The typical mass resolution is 1.7 GeV for a 125 GeV Higgs boson mass. The main background is continuum $\gamma\gamma$ production with smaller contributions, of about 20%, from the $\gamma +$ jet and dijet processes. A more complete

[3]Only J/ψ events with a muon with $p_{\mathrm{T}} > 8$ GeV are used to derive the muon momentum corrections, to avoid any bias in the corrections from nonlinearities in the momentum scale in the low momentum range.

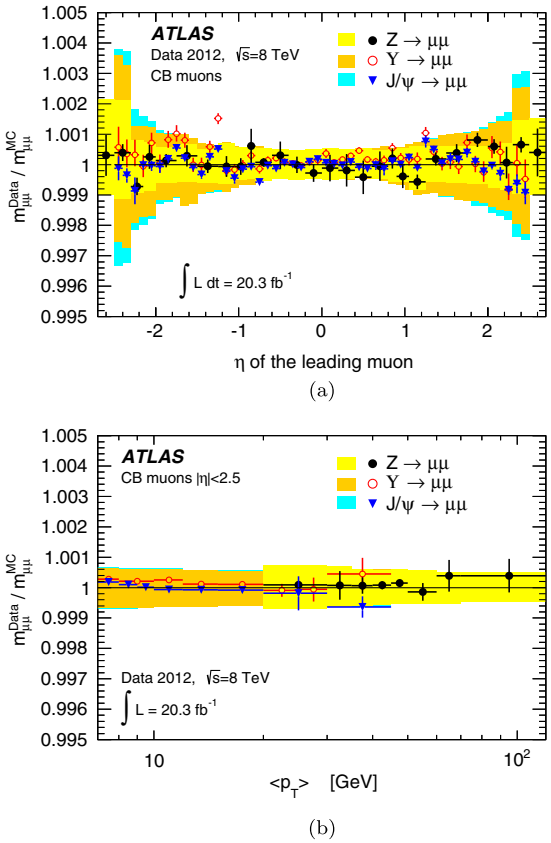

FIG. 3 (color online). Ratio of the reconstructed dimuon invariant mass for data to the corrected mass in simulation for J/ψ, Υ and Z events: (a) as a function of η of the higher-p_{T} muon and (b) as a function of $\langle p_{\mathrm{T}} \rangle$ of the two muons, as defined in the text. The shaded areas show the systematic uncertainty on the simulation corrections for each of the three samples. The error bars on the points show the combined statistical and systematic uncertainties as explained in the text. In (a), the two large $|\eta|$ bins have measurements only from Z events due to trigger limitations above $|\eta| = 2.4$.

description of the selection criteria and background modeling is reported in Ref. [17].

A. Event selection

Events are selected using a diphoton trigger. For the 7 TeV data, an E_{T} threshold of 20 GeV is applied to both photons at the trigger level. For the 8 TeV data, the E_{T} threshold at the trigger level is 35 GeV for the photon with the highest E_{T} and 25 GeV for the photon with the next-highest E_{T}. Loose photon identification cuts are applied at the trigger level, which is more than 99% efficient for events fulfilling the final analysis selection.

Only photon candidates with $|\eta| < 2.37$ are considered, removing the transition region $1.37 < |\eta| < 1.56$ between the barrel and end-cap calorimeters. The calorimeter granularity in the transition region is reduced, and the presence of significant additional inactive material affects the identification capabilities and energy resolution.

Two photons are required to fulfill tight identification criteria that are based primarily on shower shapes in the EM calorimeter [27]. For the 7 TeV data, a neural network discriminant is built from shower shape variables to suppress the contamination from jets misidentified as photon candidates. For the 8 TeV data, a set of cuts optimized for the pileup conditions of the 2012 data taking are applied. The efficiency of the photon identification selection ranges between 85% and 95% as a function of the photon E_{T}.

To further reject background from jets misidentified as photons, the photon candidates are required to be isolated using both the calorimeter isolation and track isolation requirements. The calorimeter isolation is defined as the sum of the E_{T} of clusters of energy deposited in a cone of size $\Delta R = \sqrt{(\Delta\eta)^2 + (\Delta\phi)^2} = 0.4$ around the photon candidate, excluding an area of size $\Delta\eta \times \Delta\phi = 0.125 \times 0.175$ centered on the photon cluster; the expected photon energy deposit outside the excluded area is subtracted. The pileup and underlying event contribution to the calorimeter isolation is subtracted event by event [28]. The calorimeter isolation is required to be smaller than 5.5 GeV for the 7 TeV data and smaller than 6 GeV for the 8 TeV data. The track isolation is defined as the scalar sum of the transverse momenta of the tracks in a cone of $\Delta R = 0.2$ around the photon candidate. The tracks are required to have $p_{\mathrm{T}} > 0.4(1.0)$ GeV, for the 7 (8) TeV data, and to be consistent with originating from the diphoton primary vertex, defined below. In the case of converted photons, the tracks associated with the photon conversion are excluded from the track isolation. The track isolation is required to be smaller than 2.2 GeV for the 7 TeV data and smaller than 2.6 GeV for the 8 TeV data. The efficiency of the isolation requirement is about 95% per photon for both 7 TeV and 8 TeV data.

Identifying which reconstructed primary vertex corresponds to the pp collision that produced the diphoton candidate is important for the mass reconstruction. The correct identification of the tracks coming from the pp collision producing the diphoton candidate is also necessary to avoid pileup contributions to the track isolation. To keep the contribution of the opening angle resolution to the mass resolution significantly smaller than the energy resolution contribution, a position resolution for the primary vertex of about 15 mm in the z direction is sufficient. Better resolution is needed to correctly match tracks to the pp collision vertex of the diphoton candidate. The directions of the photon candidates are measured using the longitudinal and transverse segmentation of the EM calorimeter, with a resolution of about 60 mrad$/\sqrt{E}$, where E is the photon energy in GeV. An estimate of the diphoton primary vertex z position is obtained by combining the average beam-spot position with this photon pointing, which is enhanced by using the tracks from photon conversions with conversion radii before or in the silicon

detectors. This estimate gives a resolution of about 15 mm in the z direction. In order to select the best reconstructed primary vertex, three additional variables are defined for each reconstructed primary vertex: Σp_{T} of the track transverse momenta, Σp_{T}^2, and the azimuthal angle between the combined photon system and the combined system of the tracks in the transverse plane. A neural network discriminant is constructed using the diphoton primary vertex z position estimated by the photon pointing, its uncertainty and this additional track information to select the best primary vertex candidate for the diphoton event. This algorithm selects a primary vertex within ± 15 mm in z of the true production vertex with an efficiency of 93% for the average pileup conditions in the 8 TeV data set. The contribution of the opening angle resolution to the mass resolution is thus negligible.

The diphoton invariant mass $m_{\gamma\gamma}$ is computed using the measured photon energies and their opening angle estimated from the selected primary vertex and the photon impact points in the calorimeter. The transverse energy is required to be $E_{\mathrm{T}} > 0.35 \times m_{\gamma\gamma}$ for the photon with the highest E_{T} and $E_{\mathrm{T}} > 0.25 \times m_{\gamma\gamma}$ for the photon with the second-highest E_{T}. This selection leads to a smoother background distribution in each of the event categories compared to using fixed cuts on E_{T}. The combined signal reconstruction and selection efficiency for the Higgs boson signal at an assumed mass of 125 GeV is around 40%. In total, 94627 (17225) events are selected in the 8 TeV (7 TeV) data set with $105 < m_{\gamma\gamma} < 160$ GeV.

B. Event categorization

To improve the accuracy of the mass measurement, the selected events are separated into ten mutually exclusive categories that have different signal-to-background ratios, different diphoton invariant mass resolutions and different systematic uncertainties. To keep the analysis simple, the categorization is based only on the two photon candidates. The categorization, which is different from the one used in Ref. [17], is optimized to minimize the expected uncertainty on the mass measurement, assuming a Higgs boson signal produced with the predicted SM yield, while also accounting for systematic uncertainties. Events are first separated into two groups, one where both photons are unconverted and the other where at least one photon is converted. The simulation predicts that the energy resolution for unconverted photons is better than the one for converted photons, and energy scale systematic uncertainties are different for converted and unconverted photons. The events are then classified according to the η of the two photons: the central category corresponds to events where both photons are within $|\eta| < 0.75$, the transition category corresponds to events with at least one photon with $1.3 < |\eta| < 1.75$, and the rest category corresponds to all other diphoton events. The central category has the best mass resolution and signal-to-background ratio, as well as the smallest energy scale uncertainties. The transition category suffers from worse energy resolution, due to the larger amount of material in front of the calorimeter, and also from larger systematic uncertainties. Finally, the central and rest categories are each split into a low p_{Tt} (< 70 GeV) and a high p_{Tt} (> 70 GeV) category, where p_{Tt} is the component of the diphoton transverse momentum orthogonal to the diphoton thrust axis in the transverse plane.[4] The high p_{Tt} categories have better signal-to-background ratios and mass resolution, but have smaller yield. This categorization provides a 20% reduction of the expected statistical uncertainty compared to an inclusive measurement.

C. Signal modeling

The signal mass spectrum is modeled by the sum of a Crystal Ball function for the bulk of the events, which have a narrow Gaussian spectrum in the peak and tails toward lower reconstructed mass, and a wide Gaussian distribution to model the far outliers in the mass resolution. The Crystal Ball function is defined as

$$N \cdot \begin{cases} e^{-t^2/2} & \text{if } t > -\alpha_{\mathrm{CB}} \\ \left(\frac{n_{\mathrm{CB}}}{\alpha_{\mathrm{CB}}}\right)^{n_{\mathrm{CB}}} e^{-\alpha_{\mathrm{CB}}^2/2} \left(\frac{n_{\mathrm{CB}}}{\alpha_{\mathrm{CB}}} - \alpha_{\mathrm{CB}} - t\right)^{-n_{\mathrm{CB}}} & \text{otherwise} \end{cases}$$

where $t = (m_{\gamma\gamma} - \mu_{\mathrm{CB}})/\sigma_{\mathrm{CB}}$, N is a normalization parameter, μ_{CB} is the peak of the narrow Gaussian distribution, σ_{CB} represents the Gaussian resolution for the core component, and n_{CB} and α_{CB} parametrize the non-Gaussian tail.

The σ_{CB} parameter varies from 1.2 GeV to 2.1 GeV depending on the category of the event. The overall resolution can be quantified either through its full width at half maximum (FWHM), which varies from 2.8 GeV to 5.3 GeV, or using σ_{eff}, defined as half of the smallest range containing 68% of the signal events, which varies from 1.2 GeV to 2.4 GeV.

The parameters of the Crystal Ball and Gaussian functions, and their dependence on the Higgs boson mass, are fixed by fits to simulation samples at discrete mass values to obtain a smooth signal model depending only on the assumed Higgs boson mass and yield. The accuracy of this procedure is checked by fitting the Higgs boson mass in simulated samples with this signal model and is found to be better than 0.01% of the Higgs boson mass.

D. Background modeling and estimation

The background is obtained directly from a fit to the diphoton mass distribution in the data over the range 105–160 GeV after final selection. The procedure used to select

[4] $p_{\mathrm{Tt}} = |(\boldsymbol{p}_{\mathrm{T}}^{\gamma_1} + \boldsymbol{p}_{\mathrm{T}}^{\gamma_2}) \times \hat{\mathbf{t}}|$, where $\hat{\mathbf{t}} = \frac{\boldsymbol{p}_{\mathrm{T}}^{\gamma_1} - \boldsymbol{p}_{\mathrm{T}}^{\gamma_2}}{|\boldsymbol{p}_{\mathrm{T}}^{\gamma_1} - \boldsymbol{p}_{\mathrm{T}}^{\gamma_2}|}$ is the thrust axis in the transverse plane, and $\boldsymbol{p}_{\mathrm{T}}^{\gamma_1}$, $\boldsymbol{p}_{\mathrm{T}}^{\gamma_2}$ are the transverse momenta of the two photons.

the analytical form of the function describing the background shape is explained in more detail in Ref. [17]. Different analytical functions are evaluated using a large simulated background sample composed of diphoton events, photon + jet events (with one jet misidentified as a photon) and dijet events (with both jets misidentified as photons). Signal-plus-background fits are performed on this background-only sample; thus, the fitted signal yield should be zero if the functional form used describes the background shape well. The functional form retained to describe the background is required to have a spurious fitted signal less than 20% of the expected statistical uncertainty in the data or less than 10% of the expected Standard Model signal yield over a wide range of Higgs boson mass hypotheses. The functional form satisfying these criteria with the smallest number of free parameters is used to describe the background shape in the fit of the data. In the four high p_{Tt} categories, an exponential function in mass is used. In the six other categories, the exponential of a second-order polynomial in mass is used.

Table I summarizes the expected signal rate, mass resolution and background in the ten categories for the 7 TeV and 8 TeV data samples. Small differences in mass resolution arise from the differences in the effective constant term measured with $Z \to e^+e^-$ events and from the lower pileup level in the 7 TeV data.

E. Mass measurement method

The mass spectra for the ten data categories and the two center-of-mass energies are fitted simultaneously assuming the signal-plus-background hypothesis, using an unbinned maximum likelihood fit with background and signal parametrization described in the previous sections. The fitted parameters of interest for the signal are the Higgs boson mass and the signal strength, defined as the yield normalized to the SM prediction, and applied to all production modes. Using separate signal strength modifiers for vector boson fusion and gluon fusion production has a negligible impact on the mass measurement compared to the statistical uncertainty. The parameters describing the background mass distributions for each category and center-of-mass energy are also free in the fit. The systematic uncertainties are described by a set of nuisance parameters in the likelihood. They include uncertainties affecting the signal mass peak position, modeled as Gaussian constraints, uncertainties affecting the signal mass resolution and uncertainties affecting the signal yield.

TABLE I. Summary of the expected number of signal events in the 105–160 GeV mass range n_{sig}, the FWHM of mass resolution, σ_{eff} (half of the smallest range containing 68% of the signal events), number of background events b in the smallest mass window containing 90% of the signal (σ_{eff90}), and the ratio s/b and $s/\sqrt{b}$ with s the expected number of signal events in the window containing 90% of signal events, for the $H \to \gamma\gamma$ channel. b is derived from the fit of the data in the 105–160 GeV mass range. The value of m_H is taken to be 126 GeV and the signal yield is assumed to be the expected Standard Model value. The estimates are shown separately for the 7 TeV and 8 TeV data sets and for the inclusive sample as well as for each of the categories used in the analysis.

Category	n_{sig}	FWHM [GeV]	σ_{eff} [GeV]	b in $\pm\sigma_{\mathrm{eff90}}$	s/b [%]	$s/\sqrt{b}$
$\sqrt{s} = 8$ TeV						
Inclusive	402.	3.69	1.67	10670	3.39	3.50
Unconverted central low p_{Tt}	59.3	3.13	1.35	801	6.66	1.88
Unconverted central high p_{Tt}	7.1	2.81	1.21	26.0	24.6	1.26
Unconverted rest low p_{Tt}	96.2	3.49	1.53	2624	3.30	1.69
Unconverted rest high p_{Tt}	10.4	3.11	1.36	93.9	9.95	0.96
Unconverted transition	26.0	4.24	1.86	910	2.57	0.78
Converted central low p_{Tt}	37.2	3.47	1.52	589	5.69	1.38
Converted central high p_{Tt}	4.5	3.07	1.35	20.9	19.4	0.88
Converted rest low p_{Tt}	107.2	4.23	1.88	3834	2.52	1.56
Converted rest high p_{Tt}	11.9	3.71	1.64	144.2	7.44	0.89
Converted transition	42.1	5.31	2.41	1977	1.92	0.85
$\sqrt{s} = 7$ TeV						
Inclusive	73.9	3.38	1.54	1752	3.80	1.59
Unconverted central low p_{Tt}	10.8	2.89	1.24	128	7.55	0.85
Unconverted central high p_{Tt}	1.2	2.59	1.11	3.7	30.0	0.58
Unconverted rest low p_{Tt}	16.5	3.09	1.35	363	4.08	0.78
Unconverted rest high p_{Tt}	1.8	2.78	1.21	13.6	11.6	0.43
Unconverted transition	4.5	3.65	1.61	125	3.21	0.36
Converted central low p_{Tt}	7.1	3.28	1.44	105	6.06	0.62
Converted central high p_{Tt}	0.8	2.87	1.25	3.5	21.6	0.40
Converted rest low p_{Tt}	21.0	3.93	1.75	695	2.72	0.72
Converted rest high p_{Tt}	2.2	3.43	1.51	24.7	7.98	0.40
Converted transition	8.1	4.81	2.23	365	2.00	0.38

Figure 4 shows the result of the simultaneous fit to the data over all categories. For illustration, all categories are summed together, with a weight given by the signal-to-background (s/b) ratio in each category.

F. Systematic uncertainties

The dominant systematic uncertainties on the mass measurement arise from uncertainties on the photon energy scale. These uncertainties, discussed in Sec. II, are propagated to the diphoton mass measurement in each of the ten categories, by modifying the peak of the Crystal Ball function and the average of the Gaussian function describing the signal mass spectrum. The total uncertainty on the mass measurement from the photon energy scale uncertainties ranges from 0.17% to 0.57% depending on the category. The category with the lowest systematic uncertainty is the low p_{Tt} central converted category, for which the energy scale extrapolation from $Z \to e^+e^-$ events is the smallest.

Systematic uncertainties related to the reconstruction of the diphoton primary vertex are investigated using $Z \to e^+e^-$ events reweighted to match the transverse momentum distribution of the Higgs boson and the η distribution of the decay products. The primary vertex is reconstructed using the same technique as for diphoton events, ignoring the tracks associated with the electrons, and treating them as unconverted photons. When this procedure is applied to simulated samples, the efficiency to reconstruct the primary vertex is the same in $Z \to e^+e^-$ events and $H \to \gamma\gamma$ events [17]. The dielectron invariant mass is then computed in the same way as the diphoton invariant mass. Comparing the results of this procedure in data and simulation leads to an uncertainty of 0.03% on the position of the peak of the reconstructed invariant mass.

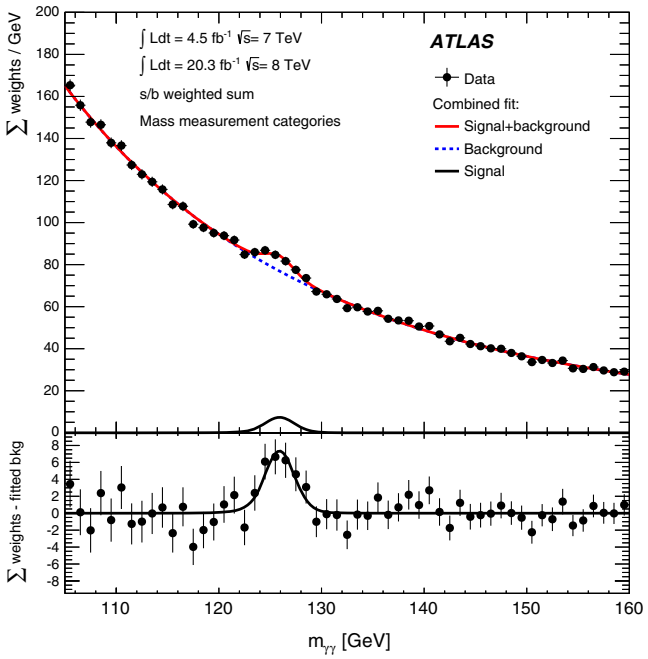

FIG. 4 (color online). Invariant mass distribution in the $H \to \gamma\gamma$ analysis for data (7 TeV and 8 TeV samples combined), showing weighted data points with errors, and the result of the simultaneous fit to all categories. The fitted signal plus background is shown, along with the background-only component of this fit. The different categories are summed together with a weight given by the s/b ratio in each category. The bottom plot shows the difference between the summed weights and the background component of the fit.

Systematic uncertainties related to the modeling of the background are estimated by performing signal-plus-background fits to samples containing large numbers of simulated background events plus the expected signal at various assumed Higgs boson masses. The signal is injected using the same functional form used in the fit, so the fitted Higgs boson mass is sensitive only to the accuracy of the background modeling. The maximum difference between the fitted Higgs boson mass and the input mass over the tested mass range is assigned as a systematic uncertainty on the mass measurement. This uncertainty varies from 0.05% to 0.20% depending on the category. The uncertainties in the different categories are taken as uncorrelated. As a cross-check, to investigate the impact of a background shape in data different than in the large statistics simulated background sample, signal-plus-background pseudo-experiments are generated using a functional form for the background with one more degree of freedom than the nominal background model used in the fit: for the four high p_{Tt} categories, a second-order Bernstein polynomial or the exponential of a second-order polynomial is used; for the six other categories, a third-order Bernstein polynomial is used. The parameters of the functional form used to generate these pseudo-experiments are determined from the data. These pseudo-experiments are then fitted using the nominal background model. This procedure leads to an uncertainty on the mass measurement between 0.01% and 0.05% depending on the category, and smaller than the uncertainties derived from the baseline method using the large sample of simulated background events.

Systematic uncertainties on the diphoton mass resolution due to uncertainties on the energy resolution vary between 9% and 16% depending on the category and have a negligible impact on the mass measurement.

Systematic uncertainties affecting the relative signal yield in each category arise from uncertainties on the photon conversion rate, uncertainties in the proper classification of converted and unconverted photon candidates and uncertainties in the modeling of the transverse momentum of the Higgs boson. These migration systematic uncertainties vary between 3% for the low p_{Tt} categories, dominated by uncertainties on the efficiency for reconstructing photon conversions, and 24% for the gluon fusion production process in the high p_{Tt} categories, dominated by

the uncertainty on the transverse momentum of the Higgs boson. The uncertainty on the transverse momentum of the Higgs boson is estimated by changing the renormalization and factorization scales in the HRes2 [29,30] computation of the Higgs boson transverse momentum distribution as well as the resummation scales associated with t and b quarks. These migration uncertainties have a negligible effect on the mass measurement.

Finally, uncertainties on the predicted overall signal yield are estimated as follows [17]. The uncertainty on the predicted cross section for Higgs boson production is about 10% for the dominant gluon fusion process. The uncertainty on the predicted branching ratio to two photons is 5%. The uncertainty from the photon identification efficiency is derived from studies using several control samples: a sample of radiative Z decays, a sample of $Z \to e^+e^-$ events, where the shower shapes of electrons are corrected to resemble the shower shapes of photons, and a sample of high E_{T} isolated prompt photons. The estimated photon identification uncertainty amounts to 1.0% for the 8 TeV data set, after correcting for small residual differences between simulation and data, and 8.4% for the 7 TeV data set. The uncertainty is larger for the 7 TeV data set because of the stronger correlation of the neural network photon identification with the photon isolation, and because the neural network identification relies more strongly on the correlations between the individual shower shape variables, complicating the measurement and introducing larger uncertainties on the estimate of its performance in data. The uncertainty on the integrated luminosity is 2.8% for the 8 TeV data set and 1.8% for the 7 TeV data set [31]. The uncertainties on the isolation cut efficiency and on the trigger efficiency are less than 1% for both the 7 TeV and 8 TeV data sets. These uncertainties on the overall signal yield also have a negligible effect on the mass measurement.

Table II gives a summary of the systematic uncertainties on the mass measurement for the different categories. For illustration, the 29 sources of uncertainty on the photon energy scale are grouped into seven classes, so the correlations in the uncertainties per class between categories are not 100%.

The total systematic uncertainty on the measured mass is $\pm 0.22\%$, dominated by the uncertainty on the photon energy scale.

G. Result

The measured Higgs boson mass in the $H \to \gamma\gamma$ decay channel is

$$\begin{aligned} m_H &= 125.98 \pm 0.42(\mathrm{stat}) \pm 0.28(\mathrm{syst})\ \mathrm{GeV} \\ &= 125.98 \pm 0.50\ \mathrm{GeV} \end{aligned} \quad (1)$$

where the first error represents the statistical uncertainty and the second the systematic uncertainty. The change in central value compared to the previous result in Ref. [15] of $126.8 \pm 0.2(\mathrm{stat}) \pm 0.7(\mathrm{syst})$ GeV is consistent with the expected change resulting from the updated photon energy scale calibration and its much smaller systematic uncertainty. From the changes in the calibration procedure an average shift of about -0.45 GeV in the measured Higgs boson mass is expected, with an expected statistical spread of about 0.35 GeV from fluctuations in the measured masses of individual events. The average shift between the old and new calibrations is estimated from the distribution of the mass difference of the common events in the mass sidebands outside the signal region.

The mass measurement is performed leaving the overall signal strength free in the fit. The measured signal strength, μ, normalized to the Standard Model expectation is found to be $\mu = 1.29 \pm 0.30$. The most precise results for μ from

TABLE II. Summary of the relative systematic uncertainties (in %) on the $H \to \gamma\gamma$ mass measurement for the different categories described in the text. The first seven rows give the impact of the photon energy scale systematic uncertainties, grouped into seven classes.

	Unconverted					Converted				
	Central		Rest			Central		Rest		
Class	low p_{Tt}	high p_{Tt}	low p_{Tt}	high p_{Tt}	Transition	low p_{Tt}	high p_{Tt}	low p_{Tt}	high p_{Tt}	Transition
$Z \to e^+e^-$ calibration	0.02	0.03	0.04	0.04	0.11	0.02	0.02	0.05	0.05	0.11
LAr cell nonlinearity	0.12	0.19	0.09	0.16	0.39	0.09	0.19	0.06	0.14	0.29
Layer calibration	0.13	0.16	0.11	0.13	0.13	0.07	0.10	0.05	0.07	0.07
ID material	0.06	0.06	0.08	0.08	0.10	0.05	0.05	0.06	0.06	0.06
Other material	0.07	0.08	0.14	0.15	0.35	0.04	0.04	0.07	0.08	0.20
Conversion reconstruction	0.02	0.02	0.03	0.03	0.05	0.03	0.02	0.05	0.04	0.06
Lateral shower shape	0.04	0.04	0.07	0.07	0.06	0.09	0.09	0.18	0.19	0.16
Background modeling	0.10	0.06	0.05	0.11	0.16	0.13	0.06	0.14	0.18	0.20
Vertex measurement					0.03					
Total	0.23	0.28	0.24	0.30	0.59	0.21	0.25	0.27	0.33	0.47

these data are based on an analysis optimized to measure the signal strength [17]. The statistical uncertainties on the mass and signal yield obtained from the data fit are consistent with the expected statistical accuracy in pseudo-experiments generated with this measured signal yield. The average expected statistical uncertainty on the mass for $\mu = 1.3$ is 0.35 GeV and the fraction of pseudo-experiments with a statistical error larger than the one observed in data (0.42 GeV) is about 16%. From these pseudo-experiments, the distribution of fitted masses is compared to the input mass value to verify that the statistical uncertainty from the fit provides 68% coverage. In the previous measurement, the expected statistical uncertainty was about 0.33 GeV for $\mu = 1.55$ and the observed statistical uncertainty (0.24 GeV) was better than expected. The change in expected statistical uncertainty mostly comes from the change in the fitted signal strength, which was slightly larger in the previous measurement, as the statistical uncertainty on the mass measurement is inversely proportional to the signal strength. Changes in the mass resolution and the event categorization also contribute to the change in the expected statistical uncertainty. The increase in the statistical uncertainty between the previous result and this result is consistent with a statistical fluctuation from changes in the measured masses of individual events. Assuming the SM signal yield ($\mu = 1$), the statistical uncertainty on the mass measurement is expected to be 0.45 GeV.

No significant shift in the values of the nuisance parameters associated with the systematic uncertainties is observed in the fit to the data. The result is also stable if a different mass range, 115 GeV to 135 GeV, is used in the fit.

Several cross-checks of the mass measurement are performed, dividing the data into subsamples with different sensitivities to systematic uncertainties. To evaluate the compatibility between the mass measured in a subsample and the combined mass from all other subsamples, a procedure similar to the one used to evaluate the mass compatibility between different channels, described in Sec. VI, is applied. The mass difference Δ_i between the subsample i under test and the combined mass from all other subsamples is added as a parameter in the likelihood, and the value of Δ_i with its uncertainty is extracted from the fit to the data, leaving the combined Higgs boson mass from all other subsamples as a free parameter. With this procedure, the uncertainty on Δ_i correctly accounts for the correlation in systematic uncertainties between the subsample under test and the rest of the data set. The values of Δ_i with their uncertainties are shown in Fig. 5 for three different alternative event categorizations, with three subsamples each: as a function of the conversion status of the two photons, as a function of the number of primary vertices reconstructed in the event and as a function of the photon impact point in the calorimeter (barrel vs end-cap).

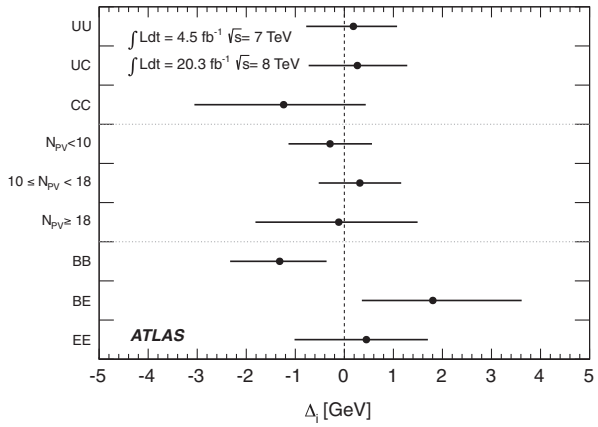

FIG. 5. Difference, Δ_i, between the mass measured in a given $\gamma\gamma$ subsample and the combined $\gamma\gamma$ mass, using three different alternative categorizations to define the subsamples. The top three points show a categorization based on the photon conversion status: UU is the subsample with both photons unconverted, UC the subsample with one converted and one unconverted photon, and CC the subsample with two converted photons. The middle three points show a categorization based on the number of reconstructed primary vertices (N_{PV}) in the event. The bottom three points show a categorization based on the photon impact points on the calorimeter: BB is the subsample with both photons detected in the barrel calorimeter, BE the subsample with one photon in the barrel calorimeter and one photon in the end-cap calorimeter and EE the subsample with both photons in the end-cap calorimeter.

No value of Δ_i inconsistent with zero is found in these checks, or in other categorizations related to the conversion topology, the instantaneous luminosity, the photon isolation and the data taking periods. A similar procedure, fitting simultaneously one Δ_i per subsample, is performed to assess the global consistency of all the different subsamples with a common combined mass. In nine different categorizations, no global inconsistency larger than 1.5σ is observed.

A direct limit on the decay width of the Higgs boson is set from the observed width of the invariant mass peak, under the assumption that there is no interference with background processes. The signal model is extended by convolving the detector resolution with a nonrelativistic Breit-Wigner distribution to model a nonzero decay width. The test statistic used to obtain the limit on the width is a profile likelihood estimator with the width as the main parameter of interest, where the mass and the signal strength of the observed particle are also treated as free parameters. Pseudo-experiments with different assumed widths are performed to estimate the distribution of the test statistic, which does not perfectly follow a χ^2 distribution, and to compute the exclusion level. The observed (expected for $\mu = 1$) 95% confidence level (CL) upper limit on the width is 5.0 (6.2) GeV. For $\mu = 1.3$, the expected upper limit on the width is 4.2 GeV. These limits, properly

calibrated with pseudo-experiments, are about 15% larger than estimates based on a χ^2 distribution of the test statistic.

V. MASS AND WIDTH MEASUREMENT IN THE $H \to ZZ^* \to 4\ell$ CHANNEL

The $H \to ZZ^* \to 4\ell$ channel provides good sensitivity to the measurement of the Higgs properties due to its high signal-to-background ratio, which is about two in the signal mass window 120–130 GeV, and its excellent mass resolution, for each of the four final states: $\mu^+\mu^-\mu^+\mu^-$ (4μ), $e^+e^-\mu^+\mu^-$ ($2e2\mu$), $\mu^+\mu^-e^+e^-$ ($2\mu2e$), and $e^+e^-e^+e^-$ ($4e$), where the first pair is defined to be the one with the dilepton mass closest to the Z boson mass. The typical mass resolution varies from 1.6 GeV for the 4μ final state to 2.2 GeV for the $4e$ final state. For a SM Higgs boson with a mass of about 125 GeV, the dominant background is the $(Z^{(*)}/\gamma^*)(Z^{(*)}/\gamma^*) \to 4\ell$ process, referred to hereafter as ZZ^*. A smaller contribution is expected from the Z + jets and $t\bar{t}$ processes.

Several improvements were introduced in the analysis with respect to Ref. [15]. For the 8 TeV data, the electron identification was changed from a cut-based to a likelihood method, which improves the rejection of light-flavor jets and photon conversions by a factor of 2 for the same signal efficiency [32]. The updated electromagnetic calibration based on multivariate techniques, described in Sec. II, is used for electrons and final-state radiation (FSR) photons. In addition, a new combined fit of the track momentum and cluster energy was introduced. This is applied to electrons with $E_{\mathrm{T}} < 30$ GeV when the track momentum and cluster energy are consistent within their uncertainties, and improves the resolution of the $m_{4\ell}$ invariant mass distribution for the $H \to ZZ^* \to 4e$ and $H \to ZZ^* \to 2\mu2e$ final states by about 4%. Finally, a multivariate discriminant was introduced to separate the signal and ZZ^* background.

The following subsections describe the details of the Higgs mass measurement in the $H \to ZZ^* \to 4\ell$ channel. A more complete discussion of the selection criteria and background determination is reported in Ref. [18].

A. Event selection

Four-lepton events are selected with single-lepton and dilepton triggers. The p_{T} (E_{T}) thresholds for single-muon (single-electron) triggers increased from 18 GeV to 24 GeV (20 GeV to 24 GeV) between the 7 and 8 TeV data sets, due to the increase of the instantaneous luminosity during these two data-taking periods. The dilepton triggers include dimuon, dielectron and mixed electron and muon topologies, and have thresholds starting at 6 GeV (10 GeV) for muons (electrons) for 7 TeV data. For the 8 TeV data, the dilepton trigger thresholds were raised to 13 GeV for the dimuon and to 12 GeV for the dielectron. In addition, for the 8 TeV data, an asymmetric threshold of (8,18) GeV was added for the dimuon trigger. The trigger efficiency for Higgs boson signal events passing the final selection is greater than 97% for the 4μ, $2e2\mu$ and $2\mu2e$ channels and close to 100% for the $4e$ channel.

For the 7 TeV data, electrons are required to satisfy a cut-based selection using tracking and shower profile criteria [33]. The 8 TeV data have an improved electron reconstruction algorithm with higher efficiency, and the likelihood-based electron identification with improved background rejection mentioned above. The four types of muons described in Sec. III are allowed with at most one standalone or calorimeter-tagged muon per event. Muon tracks are required to have a minimum number of hits in the ID, or hits in all muon stations for standalone muons.

Higgs boson candidates are formed by selecting two same-flavor, opposite-sign lepton pairs (a lepton quadruplet) in an event. Each lepton is required to have a longitudinal impact parameter less than 10 mm with respect to the primary vertex, defined as the primary vertex with the largest $\sum p_{\mathrm{T}}^2$, and muons are required to have a transverse impact parameter less than 1 mm to reject cosmic-ray muons. Each muon (electron) must satisfy $p_{\mathrm{T}} > 6$ GeV ($E_{\mathrm{T}} > 7$ GeV) and be measured in the pseudorapidity range $|\eta| < 2.7$ ($|\eta| < 2.47$). The highest p_{T} lepton in the quadruplet must satisfy $p_{\mathrm{T}} > 20$ GeV, and the second (third) lepton in p_{T} order must satisfy $p_{\mathrm{T}} > 15$ GeV ($p_{\mathrm{T}} > 10$ GeV). The leptons are required to be separated from each other by $\Delta R > 0.1\,(0.2)$ for the same (different) flavor. Each event is required to have the triggering lepton(s) matched to one or two of the selected leptons.

Multiple quadruplets within a single event are possible: for four muons or electrons there are two ways to pair the leptons, and for five or more leptons there are multiple ways to choose the leptons. Quadruplet selection is done separately in each channel: 4μ, $2e2\mu$, $2\mu2e$, $4e$, keeping only a single quadruplet per channel. For each channel, the lepton pair with the mass closest to the Z boson mass is selected as the leading dilepton pair and its invariant mass m_{12} is required to be between 50 GeV and 106 GeV. The second, subleading, pair of each channel is chosen as the pair with its invariant mass m_{34} closest to the Z mass, and also satisfying $m_{\mathrm{min}} < m_{34} < 115$ GeV. Here m_{min} takes the value of 12 GeV for $m_{4\ell} < 140$ GeV, increases linearly between 12 and 50 GeV for $140 < m_{4\ell} < 190$ GeV, and is 50 GeV for $m_{4\ell} > 190$ GeV. Finally, if the event contains a quadruplet passing the selection in more than one channel, the quadruplet from the channel with the highest expected rate is taken; i.e., the first is taken from the order: 4μ, $2e2\mu$, $2\mu2e$, $4e$.

The Z + jets and $t\bar{t}$ background contributions are further reduced by applying impact parameter and track- and calorimeter-based isolation requirements to the leptons. The impact parameter significance, $|d_0|/\sigma_{d_0}$, for all muons (electrons) is required to be less than 3.5 (6.5). The normalized track isolation discriminant, defined as the sum of the transverse momenta of tracks inside a cone

of size $\Delta R = 0.2$ around the lepton, excluding the lepton track, divided by the lepton p_{T}, is required to be smaller than 0.15. The normalized calorimetric isolation is computed from the energy in the electromagnetic and hadronic calorimeters within a cone of $\Delta R < 0.2$ around the lepton, excluding the cells containing the lepton energy. This energy is corrected, event by event, for the ambient energy deposition in the event from pileup as well as for the underlying event, and then divided by the lepton p_{T}. The normalized calorimetric isolation is required to be smaller than 0.2 (0.3) for electrons in the 7 TeV (8 TeV) data, and smaller than 0.3 for muons (0.15 for standalone muons).

The effect of photon emission from FSR on the reconstructed invariant mass is well modeled in the simulation. In addition, some FSR recovery is performed allowing at most one photon to be added per event. Leading dimuon candidates with m_{12} in the range 66–89 GeV, below the Z boson mass, are corrected for collinear FSR by including in the invariant mass any reconstructed photon lying close to one of the muon tracks, as long as the corrected mass $m_{\mu\mu\gamma}$ remains below 100 GeV. In a second step, for events without collinear FSR, noncollinear FSR photons with a significant E_{T} are included for both the leading dimuon and dielectron candidates, an improvement introduced since Ref. [15]. The expected number of events with a collinear or noncollinear FSR correction is 4% and 1%, respectively. Full details are discussed in Ref. [18].

For the 8 TeV data, the combined signal reconstruction and selection efficiency for $m_H = 125$ GeV is 39% for the 4μ channel, 27% for the $2e2\mu/2\mu2e$ channel and 20% for the $4e$ channel.

Finally, a kinematic fit is used to constrain the mass of the leading lepton pair to the Z pole mass within the experimental resolution, including any FSR photon, as in the analysis of Ref. [15]. This improves the $m_{4\ell}$ resolution by about 15%.

B. Background estimation

The ZZ^* background is estimated from simulation and normalized to NLO calculations [34]. The reducible $Z+$ jets and $t\bar{t}$ backgrounds are estimated with data-driven methods, separately for the two final states with subleading muons, $\ell\ell + \mu\mu$, and the two final states with subleading electrons, $\ell\ell + ee$. For the $\ell\ell + \mu\mu$ reducible background, the $Z+$ jets background mostly consists of $Z + b\bar{b}$ events with heavy-flavor semileptonic decays and, to a lesser extent, π/K in-flight decays. The $Z+$ jets and $t\bar{t}$ backgrounds can be distinguished in the m_{12} distribution where the former background peaks at the Z boson mass, and the latter has a broad distribution. Four control regions, with relaxed impact parameter and isolation selection on the subleading muons, are fit simultaneously to extract the different components of the reducible background. The four control regions are defined by the following: at least one subleading muon with inverted impact parameter significance to enhance the heavy-flavor contribution, at least one subleading muon with inverted isolation significance to enhance the π/K in-flight decays, same-sign subleading muons to include all contributions, and finally a leading $e\mu$ pair with either a same-sign or an opposite-sign subleading muon pair, which removes the $Z+$ jets contribution. The fitted yields in the control regions are extrapolated to the signal region using efficiencies obtained from simulation. A small contribution from WZ decays is estimated using simulation.

The electron background contributing to the $\ell\ell + ee$ final states arises mainly from jets misidentified as electrons, occurring in three ways: light-flavor hadrons misidentified as electrons, photon conversions reconstructed as electrons, and nonisolated electrons from heavy-flavor hadronic decays. The electron background is evaluated by three data-driven methods where the selection is relaxed or inverted for one or two of the subleading electrons. The final estimate is obtained using a "$3\ell + X$" control region, and the other methods, which are used as cross-checks, are described in Ref. [18]. The $3\ell + X$ control region requires the three highest p_{T} leptons (3ℓ) to satisfy the full selection, with the third ℓ an electron, and the remaining electron (X) to have the electron identification fully relaxed except for the requirement on the number of hits in the silicon tracker—at least seven silicon hits with at least one in the pixel detector. In addition, the X is required to have the same sign as the other subleading electron to minimize the contribution from the ZZ^* background. The yields of the background components of X are extracted with a fit to the number of hits in the first pixel layer (B layer) and the high-threshold to low-threshold TRT hit ratio. Most photons have no B-layer hit, and the TRT threshold distinguishes between the hadrons misidentified as electrons and the photon-conversion and heavy-flavor electrons. The fitted yields in the control region are extrapolated to the signal region using efficiencies obtained from a large sample of Z bosons produced with a single additional electron candidate satisfying the relaxed selection.

To evaluate the background in the signal region, the $m_{4\ell}$ shape is evaluated using simulated events for the $\ell\ell + \mu\mu$ final states and with data using the $3\ell + X$ method for the $\ell\ell + ee$ final states. The estimates for the ZZ^* and the reducible backgrounds in the $120 < m_{4\ell} < 130$ GeV mass window are provided in Table III.

C. Multivariate discriminant

The multivariate discriminant used to reduce the impact of the ZZ^* background on the fitted mass is based on a boosted decision tree (BDT) [35]. The BDT classifier (BDT_{ZZ^*}) is trained using simulated signal events generated with $m_H = 125$ GeV and simulated ZZ^* background events that pass the event selection and have $115 < m_{4\ell} < 130$ GeV, the mass window that contains over 95% of the signal. The variables used in the training

are the transverse momentum and the pseudorapidity of the four-lepton system, plus a matrix-element-based kinematic discriminant (D_{ZZ^*}) defined as

$$D_{ZZ^*} = \ln\left(\frac{|\mathcal{M}_{\rm sig}|^2}{|\mathcal{M}_{ZZ}|^2}\right), \quad (2)$$

where $\mathcal{M}_{\rm sig}$ and $\mathcal{M}_{ZZ}$ are the matrix elements for the signal and ZZ^* background processes, respectively, computed at leading order using MadGraph [36].

D. Signal and background model

Several methods are used to measure the Higgs boson mass in the $H \to ZZ^* \to 4\ell$ decay channel. The two-dimensional (2D) fit to $m_{4\ell}$ and the BDT_{ZZ^*} output ($O_{\mathrm{BDT}_{ZZ^*}}$) is chosen as the baseline because it has the smallest expected uncertainty among the different methods. The one-dimensional (1D) fit to the $m_{4\ell}$ spectra used for the previous measurement [15] serves as a cross-check. For both the 1D and 2D fits, the signal model is based on simulation distributions that are smoothed using a kernel density estimation method [37]. These distributions are generated at 15 different m_H values in the range $115 < m_H < 130$ GeV and form templates that are parametrized as a function of m_H using B-spline interpolation [38]. These simulation samples at different masses are normalized to the expected SM cross section times branching ratio [10] to derive the expected signal yields after acceptance and selection. For all of the methods, the $m_{4\ell}$ range used for the fit is 110 GeV to 140 GeV.

The signal probability density function (PDF) in the 2D fit is modeled as

$$\begin{aligned}\mathcal{P}(m_{4\ell}, O_{\mathrm{BDT}_{ZZ^*}}|m_H) &= \mathcal{P}(m_{4\ell}|O_{\mathrm{BDT}_{ZZ^*}}, m_H)\mathcal{P}(O_{\mathrm{BDT}_{ZZ^*}}|m_H) \\ &\simeq \left(\sum_{n=1}^{4} \mathcal{P}_n(m_{4\ell}|m_H)\theta_n(O_{\mathrm{BDT}_{ZZ^*}})\right)\mathcal{P}(O_{\mathrm{BDT}_{ZZ^*}}|m_H) \quad (3)\end{aligned}$$

where θ_n defines four equal-sized bins for the value of the BDT_{ZZ^*} output, and $\mathcal{P}_n$ represents the 1D PDF for $m_{4\ell}$ for the signal in the corresponding $O_{\mathrm{BDT}_{ZZ^*}}$ bin. The variation of the $m_{4\ell}$ shape within a single $O_{\mathrm{BDT}_{ZZ^*}}$ bin is found to be negligible, and studies indicate that the binning approximation does not bias the mass measurement. The background model, $\mathcal{P}_{\rm bkg}(m_{4\ell}, O_{\mathrm{BDT}_{ZZ^*}})$, is described using a full 2D PDF that is derived from simulation for the ZZ^* background, and by using data-driven techniques for the reducible background. The 2D template fit method reduces the expected statistical error on the measured mass with respect to the simple fit to the $m_{4\ell}$ spectra (1D method) by about 8%.

Extensive studies were performed in order to validate the signal and background PDFs using a 2D fit to fully simulated signal and background events normalized to the SM expectation. No bias was found between the input and resulting 2D fit values for the Higgs mass and signal strength, tested for different m_H values in the range 120 GeV to 130 GeV. Different values for the parameter used to control the amount of smoothing for both the signal and background PDFs were tested and no biases on the fitted m_H and signal strength were found. An additional check for a possible bias due to a small dependence of the BDT_{ZZ^*} output on m_H for the signal, included in Eq. (3), is performed by fitting a sample of background-only simulated data. No dependence of the likelihood scan on m_H was observed.

In addition to the 2D fit method, described above, and the 1D fit method used in Ref. [15], a third approach is used. This approach combines an analytic description of the signal mass spectra with the BDT_{ZZ^*} output and can be used both for the mass measurement and to provide a direct limit on the width of the Higgs boson. In this method, the signal $m_{4\ell}$ PDF is computed event by event by convolving the estimated detector response for each of the four leptons with the nonrelativistic Breit-Wigner function describing the generated Higgs mass line shape. The advantage of this method is that the typical detector response for each data candidate is taken into account in the signal modeling. This is referred to as the per-event-error method. In this fit the Z mass constraint is not applied. The muon and electron response functions are modeled by the sum of two or three Gaussian distributions, respectively, to provide a better description of the responses. This parametrization is performed in bins of η and $p_{\rm T}$. These response functions are validated with several simulation samples and with data. One validation consists of comparing the Z boson mass distribution measured in collision data with the convolution of the generator-level Z boson resonance with the detector response, constructed using the single-lepton response. The ratio of the two distributions agrees to better than 2% for $Z \to \mu\mu$ and 5% for $Z \to ee$. In addition, the per-event-error model is checked by fitting the four-lepton invariant mass from the Z decay in the $Z \to 4\ell$ process. The fit results are in agreement with the world average values of the Z boson mass and width [39]. The per-event-error fit is used both as a cross-check for the mass measurement and as the baseline method to set an upper limit on the Higgs boson total width Γ_H.

For the mass measurement, the $m_{4\ell}$ (and $O_{\mathrm{BDT}_{ZZ^*}}$) data distributions for eight sets of events, one for each final state for the 7 TeV and 8 TeV data, are simultaneously fitted using an unbinned maximum likelihood assuming the signal and background models described above. The backgrounds are set in the fit to their estimated values, and the associated normalization and shape uncertainties are treated as nuisance parameters, as discussed in Sec. VI.

E. Systematic uncertainties

The main sources of systematic uncertainties on the mass measurement are the electron energy scale and the muon momentum scale. The expected impact of these uncertainties on the mass measurement corresponds to about 60 MeV for both the $4e$ and the 4μ channels, obtained from the 2D fit to simulation. When all the final states are combined together, this translates to an observed $\pm 0.03\%$ uncertainty on m_H for both the electron energy scale and the muon momentum scale.

Systematic uncertainties on the measurement of the inclusive signal rate are also included in the model. The uncertainty on the inclusive signal strength due to the identification and reconstruction efficiency for muons and electrons is $\pm 2\%$. The dominant theory systematic uncertainties arise from QCD scale variations of the $gg \to H$ process ($\pm 7\%$), parton distribution function variations ($\pm 6\%$) and the decay branching ratio ($\pm 4\%$). The uncertainty on the Higgs boson transverse momentum, evaluated as described in Sec. IV F, has a negligible impact on the mass and the inclusive signal rate measurements. The uncertainty on the integrated luminosity is given in Sec. IV F, and it has a negligible impact on the mass measurement.

F. Results

Figure 6(a) shows the $m_{4\ell}$ distribution of the selected candidates for 7 TeV and 8 TeV collision data along with the expected distributions for a signal with a mass of 124.5 GeV and the ZZ^* and reducible backgrounds. The expected signal is normalized to the measured signal strength, given below. Figure 6(b) shows the BDT_{ZZ^*} output versus $m_{4\ell}$ for the selected candidates in the $m_{4\ell}$ range 110–140 GeV. The compatibility of the data with the expectations shown in Fig. 6(b) has been checked using pseudo-experiments generated according to the expected two-dimensional distributions and good agreement has been found. Table III presents the observed and expected number of events for $\sqrt{s} = 7$ TeV and $\sqrt{s} = 8$ TeV, in a mass window of 120–130 GeV, corresponding to about $\pm 2\sigma_{m_{4\ell}}$.

The measured Higgs boson mass in the $H \to ZZ^* \to 4\ell$ decay channel obtained with the baseline 2D method is

$$m_H = 124.51 \pm 0.52(\mathrm{stat}) \pm 0.06(\mathrm{syst})\ \mathrm{GeV} = 124.51 \pm 0.52\ \mathrm{GeV} \quad (4)$$

where the first error represents the statistical uncertainty and the second the systematic uncertainty. The systematic uncertainty is obtained from the quadrature subtraction of the fit uncertainty evaluated with and without the systematic uncertainties fixed at their best-fit values. Due to the large difference between the magnitude of the statistical and systematic uncertainties, the numerical precision on the quadrature subtraction is estimated to be of the order of 10 MeV. The measured signal strength for this inclusive selection is $\mu = 1.66^{+0.45}_{-0.38}$, consistent with the SM expectation of 1. The most precise results for μ from these data are

TABLE III. The number of events expected and observed for a $m_H = 125$ GeV hypothesis for the four-lepton final states. The second column shows the number of expected signal events for the full mass range. The other columns show the number of expected signal events, the number of ZZ^* and reducible background events, and the signal-to-background ratio (s/b), together with the numbers of observed events, in a window of $120 < m_{4\ell} < 130$ GeV for 4.5 fb^{-1} at $\sqrt{s} = 7$ TeV and 20.3 fb^{-1} at $\sqrt{s} = 8$ TeV as well as for the combined sample.

Final state	Signal Full mass range	Signal	ZZ^*	Z + jets, $t\bar{t}$	s/b	Expected	Observed
$\sqrt{s} = 7$ TeV							
4μ	1.00 ± 0.10	0.91 ± 0.09	0.46 ± 0.02	0.10 ± 0.04	1.7	1.47 ± 0.10	2
$2e2\mu$	0.66 ± 0.06	0.58 ± 0.06	0.32 ± 0.02	0.09 ± 0.03	1.5	0.99 ± 0.07	2
$2\mu 2e$	0.50 ± 0.05	0.44 ± 0.04	0.21 ± 0.01	0.36 ± 0.08	0.8	1.01 ± 0.09	1
$4e$	0.46 ± 0.05	0.39 ± 0.04	0.19 ± 0.01	0.40 ± 0.09	0.7	0.98 ± 0.10	1
Total	2.62 ± 0.26	2.32 ± 0.23	1.17 ± 0.06	0.96 ± 0.18	1.1	4.45 ± 0.30	6
$\sqrt{s} = 8$ TeV							
4μ	5.80 ± 0.57	5.28 ± 0.52	2.36 ± 0.12	0.69 ± 0.13	1.7	8.33 ± 0.6	12
$2e2\mu$	3.92 ± 0.39	3.45 ± 0.34	1.67 ± 0.08	0.60 ± 0.10	1.5	5.72 ± 0.37	7
$2\mu 2e$	3.06 ± 0.31	2.71 ± 0.28	1.17 ± 0.07	0.36 ± 0.08	1.8	4.23 ± 0.30	5
$4e$	2.79 ± 0.29	2.38 ± 0.25	1.03 ± 0.07	0.35 ± 0.07	1.7	3.77 ± 0.27	7
Total	15.6 ± 1.6	13.8 ± 1.4	6.24 ± 0.34	2.00 ± 0.28	1.7	22.1 ± 1.5	31
$\sqrt{s} = 7$ TeV and $\sqrt{s} = 8$ TeV							
4μ	6.80 ± 0.67	6.20 ± 0.61	2.82 ± 0.14	0.79 ± 0.13	1.7	9.81 ± 0.64	14
$2e2\mu$	4.58 ± 0.45	4.04 ± 0.40	1.99 ± 0.10	0.69 ± 0.11	1.5	6.72 ± 0.42	9
$2\mu 2e$	3.56 ± 0.36	3.15 ± 0.32	1.38 ± 0.08	0.72 ± 0.12	1.5	5.24 ± 0.35	6
$4e$	3.25 ± 0.34	2.77 ± 0.29	1.22 ± 0.08	0.76 ± 0.11	1.4	4.75 ± 0.32	8
Total	18.2 ± 1.8	16.2 ± 1.6	7.41 ± 0.40	2.95 ± 0.33	1.6	26.5 ± 1.7	37

based on an analysis optimized to measure the signal strength [18]. The expected statistical uncertainty for the 2D fit with the observed μ value of 1.66 is 0.49 GeV, close to the observed statistical uncertainty. With the improved uncertainties on the electron and muon energy scales, the mass uncertainty given above is predominantly statistical with a nearly negligible contribution from systematic uncertainties. The mass measurement performed with the 1D model gives $m_H = 124.63 \pm 0.54$ GeV, consistent with the 2D result where the expected difference has a root mean square (RMS) of 250 MeV estimated from Monte Carlo pseudo-experiments. These measurements can be compared to the previously reported result [15] of $124.3^{+0.6}_{-0.5}(\text{stat})^{+0.5}_{-0.3}(\text{syst})$ GeV, which was obtained using the 1D model. The difference between the measured values arises primarily from the changes to the channels with electrons—the new calibration and resolution model, the introduction of the combined track momentum and cluster energy fit, and the improved identification, as well as the recovery of noncollinear FSR photons, which affects all channels. In the 120–130 GeV mass window, there are four new events and one missing event as compared to Ref. [15]. Finally, as a third cross-check, the measured mass obtained with the per-event-error method is within 60 MeV of the value found with the 2D method.

Figure 7 shows the scan of the profile likelihood, $-2\ln\Lambda(m_H)$, for the 2D model as a function of the mass of the Higgs boson for the four final states, as well as for all of the channels combined. The signal strength and all the nuisance parameters are profiled (allowed to float to the values that maximize the likelihood) in the scan. The compatibility among the mass measurements from the four final states is estimated to be about 20% using a χ^2 test.

Using the per-event-error method a direct limit on the total width of the Higgs boson of $\Gamma_H < 2.6$ GeV at

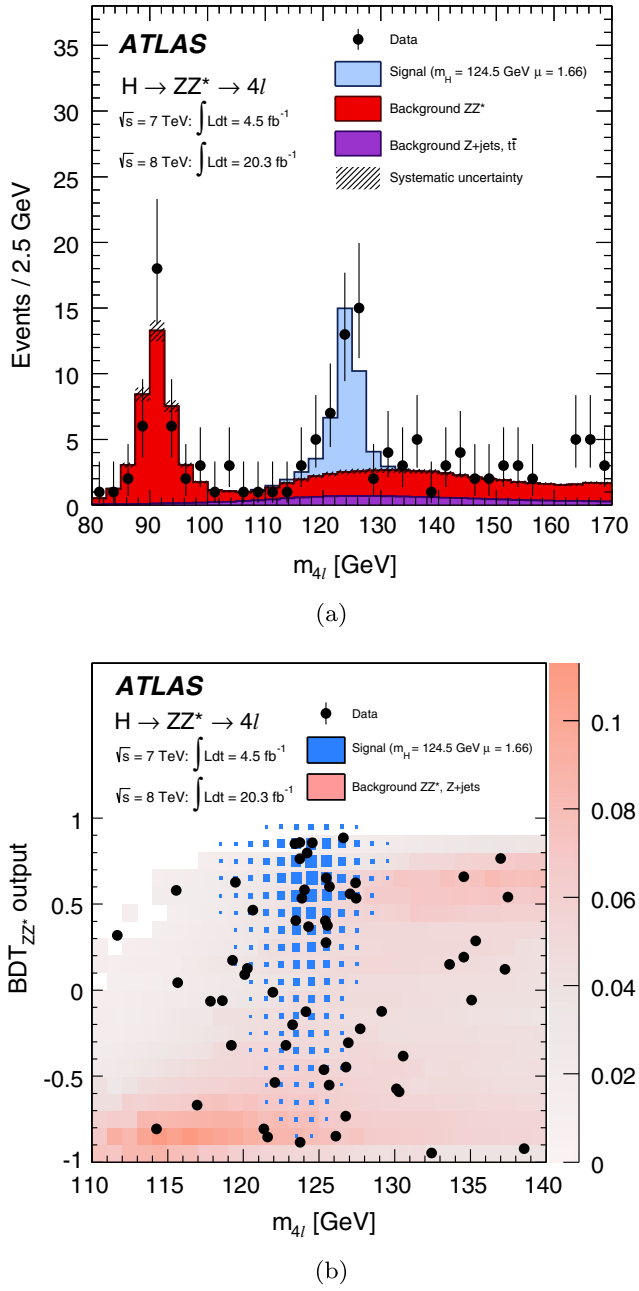

FIG. 6 (color online). (a) Distribution of the four-lepton invariant mass for the selected candidates in the $m_{4\ell}$ range 80–170 GeV for the combined 7 TeV and 8 TeV data samples. Superimposed are the expected distributions of a SM Higgs boson signal for $m_H = 124.5$ GeV normalized to the measured signal strength, as well as the expected ZZ^* and reducible backgrounds. (b) Distribution of the BDT_{ZZ^*} output versus $m_{4\ell}$ for the selected candidates in the 110–140 GeV $m_{4\ell}$ range for the combined 7 TeV and 8 TeV data samples. The expected distribution for a SM Higgs with $m_H = 124.5$ GeV is indicated by the size of the blue boxes, and the total background is indicated by the intensity of the red shading.

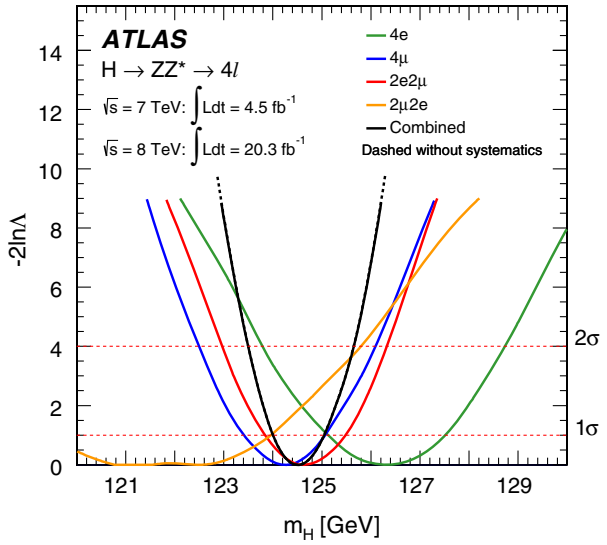

FIG. 7 (color online). The profile likelihood as a function of m_H for the combination of all $H \to ZZ^* \to 4\ell$ channels and for the individual channels for the combined 7 TeV and 8 TeV data samples. The combined result is shown both with (solid line) and without (dashed line) systematic uncertainties, and the two results are almost indistinguishable.

95% CL is obtained. The expected limit is $\Gamma_H < 6.2$ GeV at 95% CL for a signal at the SM rate and $\Gamma_H < 3.5$ GeV at 95% CL for the observed signal rate. The difference between the observed and expected results arises from the higher signal strength observed in the data, as well as from the measured $m_{4\ell}$, $O_{\mathrm{BDT}_{ZZ^*}}$ and mass resolution values for the selected candidate events. These limits are estimated under the asymptotic assumption, described in Sec. VI, and a cross-check with Monte Carlo ensemble tests provides consistent results. The limit on the total width was cross-checked with a 2D fit using signal templates parametrized as a function of the Higgs boson width and found to be in agreement.

VI. STATISTICAL PROCEDURE AND TREATMENT OF SYSTEMATIC UNCERTAINTIES

The statistical treatment of the data is described in Refs. [40–44]. Confidence intervals are based on the profile likelihood ratio $\Lambda(\boldsymbol{\alpha})$ [45]. The latter depends on one or more parameters of interest $\boldsymbol{\alpha}$, such as the Higgs boson mass m_H or production yields normalized to the SM expectation μ, as well as on the nuisance parameters $\boldsymbol{\theta}$:

$$\Lambda(\boldsymbol{\alpha}) = \frac{L(\boldsymbol{\alpha}, \hat{\hat{\boldsymbol{\theta}}}(\boldsymbol{\alpha}))}{L(\hat{\boldsymbol{\alpha}}, \hat{\boldsymbol{\theta}})}. \quad (5)$$

The likelihood functions in the numerator and denominator of the above equation are built using sums of signal and background PDFs in the discriminating variables, such as the $\gamma\gamma$ mass spectra for the $H \to \gamma\gamma$ channel and the $m_{4\ell}$ and BDT_{ZZ^*} output distributions for the $H \to ZZ^* \to 4\ell$ channel. The PDFs are derived from simulation for the signal and from both data and simulation for the background, as described in Secs. IV and V. Likelihood fits to the observed data are carried out for the parameters of interest. The vector $\hat{\boldsymbol{\theta}}$ denotes the unconditional maximum likelihood estimate of the parameter values, and $\hat{\hat{\boldsymbol{\theta}}}$ denotes the conditional maximum likelihood estimate for given fixed values of the parameters of interest $\boldsymbol{\alpha}$. Systematic uncertainties and their correlations [40] are modeled by introducing nuisance parameters $\boldsymbol{\theta}$ described by likelihood functions associated with the estimate of the corresponding effect. The choice of the parameters of interest depends on the test under consideration, with the remaining parameters treated as nuisance parameters, i.e., set to the values that maximize the likelihood function ("profiled") for the given fixed values of the parameters of interest.

For the combined mass measurement, hypothesized values of m_H are tested using the profile likelihood ratio defined in terms of m_H and treating $\mu_{\gamma\gamma}(m_H)$ and $\mu_{4\ell}(m_H)$ as independent nuisance parameters, so as to avoid making any assumptions about the Higgs boson couplings:

$$\Lambda(m_H) = \frac{L(m_H, \hat{\hat{\mu}}_{\gamma\gamma}(m_H), \hat{\hat{\mu}}_{4\ell}(m_H), \hat{\hat{\boldsymbol{\theta}}}(m_H))}{L(\hat{m}_H, \hat{\mu}_{\gamma\gamma}, \hat{\mu}_{4\ell}, \hat{\boldsymbol{\theta}})}. \quad (6)$$

The leading source of systematic uncertainty on the mass measurement comes from the energy and momentum scale uncertainties on the main physics objects used in the two analyses, namely, photons for the $H \to \gamma\gamma$ and muons and electrons for the $H \to ZZ^* \to 4\ell$ final state. They are detailed in Secs. II and III. The correlation between the two measurements stems from common systematic uncertainties and is modeled in the combination by correlating the corresponding nuisance parameters. For the mass measurement this correlation comes mainly from the uncertainty on the energy scale calibration with $Z \to e^+e^-$ events, which affects both the electron and photon energy scale uncertainties. This source of uncertainty is greatly reduced with respect to the previous publication and has a small impact on the total mass uncertainty for both channels. For this reason, the correlation between the two measurements is now almost negligible.

To directly quantify the level of consistency between the measurements of $m_H^{\gamma\gamma}$ and $m_H^{4\ell}$, the profile likelihood used for the mass combination is parametrized as a function of the difference in measured mass values $\Delta m_H = m_H^{\gamma\gamma} - m_H^{4\ell}$, with the common mass m_H profiled in the fit. Specifically, the observable $m_H^{4\ell}$ is fit to the parameter m_H while the observable $m_H^{\gamma\gamma}$ is fit to the parameter $m_H + \Delta m_H$. The two measurements are compatible if the fitted value of Δm_H is compatible with zero. The original model used to combine the two measurements is recovered by fixing the parameter Δm_H to zero.

The signal strengths $\mu_{\gamma\gamma}$ and $\mu_{4\ell}$ are treated as independent nuisance parameters in this approach, as is the common mass m_H. The variation of $-2\ln\Lambda(\Delta m_H)$ between its minimum and the $\Delta m_H = 0$ point is used as an estimate of the compatibility of the two masses, with all other fit parameters profiled to the data. This result relies on the assumption that the statistical observable $-2\ln\Lambda$ behaves as a χ^2 distribution with 1 degree of freedom, referred to as the asymptotic assumption. This result is also cross-checked with Monte Carlo ensemble tests that do not rely on this assumption. All sources of energy and momentum scale systematic uncertainty are treated assuming Gaussian PDFs.

VII. COMBINED MASS MEASUREMENT

The measured masses from the $H \to \gamma\gamma$ and $H \to ZZ^* \to 4\ell$ channels reported in Secs. IV and V are combined following the method described in Sec. VI. For the $H \to ZZ^* \to 4\ell$ channel the 2D method discussed in Sec. V is used. The combined mass measurement is

$$\begin{aligned} m_H &= 125.36 \pm 0.37(\mathrm{stat}) \pm 0.18(\mathrm{syst})\ \mathrm{GeV} \\ &= 125.36 \pm 0.41\ \mathrm{GeV} \end{aligned} \quad (7)$$

where the first error represents the statistical uncertainty and the second the systematic uncertainty. The statistical component is determined by repeating the likelihood scan with all nuisance parameters related to systematic uncertainty fixed to their best-fit value. The systematic component is then derived by subtracting in quadrature the statistical one from the total error. The $-2\ln\Lambda$ value as a function of m_H for the individual $H \to \gamma\gamma$ and $H \to ZZ^* \to 4\ell$ channels and their combination is shown in Fig. 8.

With respect to the previously published value [15] of $m_H = 125.49 \pm 0.24(\text{stat})^{+0.50}_{-0.58}(\text{syst})$ GeV, the observed statistical error has increased. This is due to the increase of the observed statistical error in the $H \to \gamma\gamma$ channel as discussed in Sec. IV G. The systematic uncertainty is significantly reduced thanks to the improvements in the calibration of the photons and electrons and the reduction in the uncertainty on the muon momentum scale, as detailed in Secs. II and III, respectively.

In order to check that the fitted signal yield is not significantly correlated with the measured mass, the profile likelihood ratio as a function of both m_H and the normalized signal yield S, $\Lambda(S, m_H)$ is used. The normalized signal yield is defined as $S = \sigma/\sigma_{\text{SM}}(m_H = 125.36\ \text{GeV})$. It is similar to the signal strength $\mu = \sigma/\sigma_{\text{SM}}(m_H)$, except the m_H dependence of the expected SM cross sections and branching ratios that enter into the denominator, principally for the $H \to ZZ^* \to 4\ell$ channel, is removed by fixing m_H to the combined best-fit mass. Asymptotically, the test statistic $-2\ln\Lambda(S, m_H)$ is distributed as a χ^2 distribution with 2 degrees of freedom. The resulting 68% and 95% CL contours are shown in Fig. 9. No significant correlation between the two fitted variables is observed, confirming the model independence of the mass measurement described in this paper.

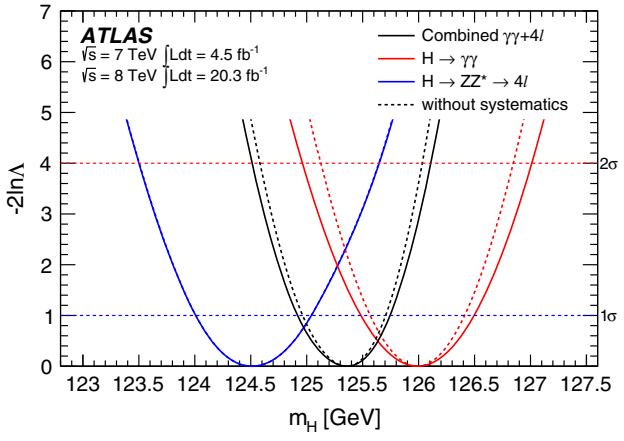

FIG. 8 (color online). Value of $-2\ln\Lambda$ as a function of m_H for the individual $H \to \gamma\gamma$ and $H \to ZZ^* \to 4\ell$ channels and their combination, where the signal strengths $\mu_{\gamma\gamma}$ and $\mu_{4\ell}$ are allowed to vary independently. The dashed lines show the statistical component of the mass measurements. For the $H \to ZZ^* \to 4\ell$ channel, this is indistinguishable from the solid line that includes the systematic uncertainties.

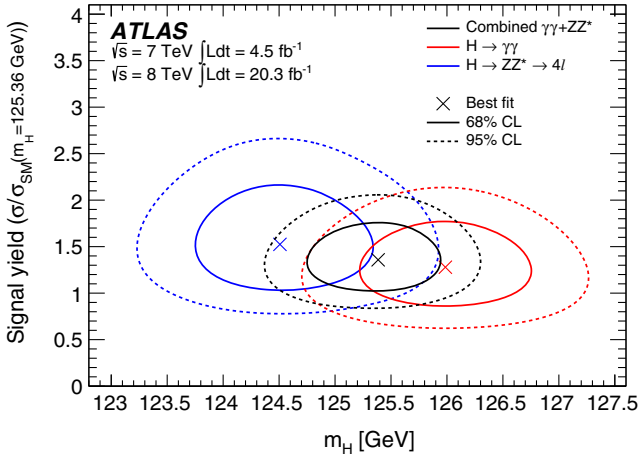

FIG. 9 (color online). Likelihood contours $-2\ln\Lambda(S, m_H)$ as a function of the normalized signal yield $S = \sigma/\sigma_{\text{SM}}(m_H = 125.36\ \text{GeV})$ and m_H for the $H \to \gamma\gamma$ and $H \to ZZ^* \to 4\ell$ channels and their combination, including all systematic uncertainties. For the combined contour, a common normalized signal yield S is used. The markers indicate the maximum likelihood estimates in the corresponding channels.

As a cross-check, the mass combination was repeated by fixing the values of the two signal strengths to the SM expectation $\mu = 1$. The mass measurement only changes by 80 MeV, demonstrating that the combined mass measurement is quite insensitive to the fitted values of the individual channel signal strengths.

The contributions of the main sources of systematic uncertainty to the combined mass measurement are shown in Table IV. In the mass measurement fit, the post-fit values of the most relevant nuisance parameters, which are related to the photon energy scale, do not show significant deviations from their pre-fit input values.

In order to assess the compatibility of the mass measurements from the two channels, a dedicated test statistic that takes into account correlations between the two measurements is used, as described in Sec. VI. A value of

$$\begin{aligned}\Delta m_H &= 1.47 \pm 0.67(\text{stat}) \pm 0.28(\text{syst})\ \text{GeV} \\ &= 1.47 \pm 0.72\ \text{GeV}\end{aligned} \tag{8}$$

is derived. From the value of $-2\ln\Lambda$ at $\Delta m_H = 0$, a compatibility of 4.8%, equivalent to 1.98σ, is estimated under the asymptotic assumption. This probability was cross-checked using Monte Carlo ensemble tests. With this approach a compatibility of 4.9% is obtained, corresponding to 1.97σ.

As an additional cross-check, some of the systematic uncertainties related to the photon energy scale, namely, the inner detector material uncertainty and the uncertainty in the modeling of the photon lateral leakage, were modeled

TABLE IV. Principal systematic uncertainties on the combined mass. Each uncertainty is determined from the change in the 68% CL range for m_H when the corresponding nuisance parameter is removed (fixed to its best-fit value), and it is calculated by subtracting this reduced uncertainty from the original uncertainty in quadrature.

Systematic	Uncertainty on m_H [MeV]
LAr syst on material before presampler (barrel)	70
LAr syst on material after presampler (barrel)	20
LAr cell nonlinearity (layer 2)	60
LAr cell nonlinearity (layer 1)	30
LAr layer calibration (barrel)	50
Lateral shower shape (conv)	50
Lateral shower shape (unconv)	40
Presampler energy scale (barrel)	20
ID material model ($\lvert\eta\rvert < 1.1$)	50
$H \to \gamma\gamma$ background model (unconv rest low p_{Tt})	40
$Z \to ee$ calibration	50
Primary vertex effect on mass scale	20
Muon momentum scale	10
Remaining systematic uncertainties	70
Total	180

using a "boxlike" PDF defined as a double Fermi-Dirac function. This choice is compatible with the fact that for these uncertainties the data do not suggest a preferred value within the systematic error range. In this case the compatibility between the two masses increases to 7.5%, equivalent to 1.8σ. The compatibility between the two measurements increases to 11% (1.6σ) if the two signal strengths are set to the SM value of 1, instead of being treated as free parameters.

With respect to the value published in Ref. [15], the compatibility between the measurements from the individual channels has changed from 2.5σ to 2.0σ.

VIII. CONCLUSIONS

An improved measurement of the mass of the Higgs boson has been derived from a combined fit to the invariant mass spectra of the decay channels $H \to \gamma\gamma$ and $H \to ZZ^* \to 4\ell$. These measurements are based on the pp collision data sample recorded by the ATLAS experiment at the CERN Large Hadron Collider at center-of-mass energies of $\sqrt{s} = 7$ TeV and $\sqrt{s} = 8$ TeV, corresponding to an integrated luminosity of 25 fb^{-1}. As shown in Table V, the measured values of the Higgs boson mass for the $H \to \gamma\gamma$ and $H \to ZZ^* \to 4\ell$ channels are $125.98 \pm 0.42(\mathrm{stat}) \pm 0.28(\mathrm{syst})$ GeV and $124.51 \pm 0.52(\mathrm{stat}) \pm 0.06(\mathrm{syst})$ GeV, respectively. The compatibility between the mass measurements from the two individual channels is at the level of 2.0σ corresponding to a probability of 4.8%.

From the combination of these two channels, the value of $m_H = 125.36 \pm 0.37(\mathrm{stat}) \pm 0.18(\mathrm{syst})$ GeV is obtained.

TABLE V. Summary of Higgs boson mass measurements.

Channel	Mass measurement [GeV]
$H \to \gamma\gamma$	$125.98 \pm 0.42(\mathrm{stat}) \pm 0.28(\mathrm{syst}) = 125.98 \pm 0.50$
$H \to ZZ^* \to 4\ell$	$124.51 \pm 0.52(\mathrm{stat}) \pm 0.06(\mathrm{syst}) = 124.51 \pm 0.52$
Combined	$125.36 \pm 0.37(\mathrm{stat}) \pm 0.18(\mathrm{syst}) = 125.36 \pm 0.41$

These results are based on improved calibrations for photons, electrons and muons and on improved analysis techniques with respect to Ref. [15], and they supersede the previous results.

Upper limits on the total width of the Higgs boson are derived from fits to the mass spectra of the $H \to \gamma\gamma$ and $H \to ZZ^* \to 4\ell$ decay channels, under the assumption that there is no interference with background processes. In the $H \to \gamma\gamma$ channel, a 95% CL limit of 5.0 (6.2) GeV is observed (expected). In the $H \to ZZ^* \to 4\ell$ channel, a 95% CL limit of 2.6 (6.2) GeV is observed (expected).

ACKNOWLEDGMENTS

We thank CERN for the very successful operation of the LHC, as well as the support staff from our institutions without whom ATLAS could not be operated efficiently. We acknowledge the support of ANPCyT, Argentina; YerPhI, Armenia; ARC, Australia; BMWF and FWF, Austria; ANAS, Azerbaijan; SSTC, Belarus; CNPq and FAPESP, Brazil; NSERC, NRC and CFI, Canada; CERN; CONICYT, Chile; CAS, MOST and NSFC, China; COLCIENCIAS, Colombia; MSMT CR, MPO CR and VSC CR, Czech Republic; DNRF, DNSRC and Lundbeck Foundation, Denmark; EPLANET, ERC and NSRF, European Union; IN2P3-CNRS, CEA-DSM/IRFU, France; GNSF, Georgia; BMBF, DFG, HGF, MPG and AvH Foundation, Germany; GSRT and NSRF, Greece; ISF, MINERVA, GIF, I-CORE and Benoziyo Center, Israel; INFN, Italy; MEXT and JSPS, Japan; CNRST, Morocco; FOM and NWO, Netherlands; BRF and RCN, Norway; MNiSW and NCN, Poland; GRICES and FCT, Portugal; MNE/IFA, Romania; MES of Russia and ROSATOM, Russian Federation; JINR; MSTD, Serbia; MSSR, Slovakia; ARRS and MIZŠ, Slovenia; DST/NRF, South Africa; MINECO, Spain; SRC and Wallenberg Foundation, Sweden; SER, SNSF and Cantons of Bern and Geneva, Switzerland; NSC, Taiwan; TAEK, Turkey; STFC, the Royal Society and Leverhulme Trust, United Kingdom; DOE and NSF, United States of America. The crucial computing support from all WLCG partners is acknowledged gratefully, in particular, from CERN and the ATLAS Tier-1 facilities at TRIUMF (Canada), NDGF (Denmark, Norway, Sweden), CC-IN2P3 (France), KIT/GridKA (Germany), INFN-CNAF (Italy), NL-T1 (Netherlands), PIC (Spain), ASGC (Taiwan), RAL (UK) and BNL (USA), and in the Tier-2 facilities worldwide.

[1] ATLAS Collaboration, Phys. Lett. B **716**, 1 (2012).
[2] CMS Collaboration, Phys. Lett. B **716**, 30 (2012).
[3] F. Englert and R. Brout, Phys. Rev. Lett. **13**, 321 (1964).
[4] P. W. Higgs, Phys. Lett. **12**, 132 (1964).
[5] P. W. Higgs, Phys. Rev. Lett. **13**, 508 (1964).
[6] G. S. Guralnik, C. R. Hagen, and T. W. B. Kibble, Phys. Rev. Lett. **13**, 585 (1964).
[7] P. W. Higgs, Phys. Rev. **145**, 1156 (1966).
[8] T. W. B. Kibble, Phys. Rev. **155**, 1554 (1967).
[9] L. Evans and P. Bryant, JINST **3**, S08001 (2008).
[10] LHC Higgs Cross Section Working Group, *Handbook of LHC Higgs Cross Sections: 3. Higgs Properties*, edited by S. Heinemeyer, C. Mariotti, G. Passarino, and R. Tanaka (CERN, Geneva, 2013), p. 404 [arXiv:1307.1347].
[11] N. Kauer and G. Passarino, J. High Energy Phys. 08 (2012) 116.
[12] L. J. Dixon and M. S. Siu, Phys. Rev. Lett. **90**, 252001 (2003).
[13] L. J. Dixon and Y. Li, Phys. Rev. Lett. **111**, 111802 (2013).
[14] S. P. Martin, Phys. Rev. D **86**, 073016 (2012).
[15] ATLAS Collaboration, Phys. Lett. B **726**, 88 (2013).
[16] CMS Collaboration, Phys. Rev. D **89**, 092007 (2014).
[17] ATLAS Collaboration, arXiv:1408.7084.
[18] ATLAS Collaboration, arXiv:1408.5191.
[19] ATLAS Collaboration, arXiv:1407.5063.
[20] ATLAS Collaboration, arXiv:1407.3935.
[21] ATLAS Collaboration, JINST **3**, S08003 (2008).
[22] ATLAS Collaboration, Report No. ATLAS-CONF-2012-047, 2012, http://cds.cern.ch/record/1449796.
[23] H. Abreu *et al.*, JINST **5**, P09003 (2010).
[24] ATLAS Collaboration, JINST **7**, P01013 (2012).
[25] ATLAS Collaboration, Eur. Phys. J. C **72**, 1909 (2012).
[26] ATLAS Collaboration, arXiv:1404.4562.
[27] ATLAS Collaboration, Report No. ATLAS-CONF-2012-123, 2012, http://cds.cern.ch/record/1473426.
[28] M. Cacciari and G. P. Salam, Phys. Lett. B **659**, 119 (2008).
[29] D. de Florian, G. Ferrera, M. Grazzini, and D. Tommasini, J. High Energy Phys. 06 (2012) 132.
[30] M. Grazzini and H. Sargsyan, J. High Energy Phys. 09 (2013) 129.
[31] ATLAS Collaboration, Eur. Phys. J. C **73**, 2518 (2013).
[32] ATLAS Collaboration, Report No. ATLAS-CONF-2014-032, 2014, http://cds.cern.ch/record/1706245.
[33] ATLAS Collaboration, Eur. Phys. J. C **74**, 2941 (2014).
[34] LHC Higgs Cross Section Working Group, edited by S. Dittmaier, C. Mariotti, G. Passarino, and R. Tanaka, Reports No. CERN-2012-002, and No. 10.5170/CERN-2012-002, 2012 arXiv:1201.3084.
[35] A. Hocker *et al.*, *Proc. Sci.*, ACAT2007 (2007) 040 [arXiv:physics/0703039].
[36] J. Alwall, R. Frederix, S. Frixione, V. Hirschi, F. Maltoni, O. Mattelaer, H.-S. Shao, T. Stelzer, P. Torrielli, and M. Zaro, J. High Energy Phys. 07 (2014) 079.
[37] K. S. Cranmer, Comput. Phys. Commun. **136**, 198 (2001).
[38] L. A. Piegl and W. Tiller, *The Nurbs Book*, 2nd ed. (Springer, Berlin Heidelberg, 1997) Chap. B-Spline Basis Function.
[39] S. Schael *et al.* (ALEPH Collaboration, DELPHI Collaboration, L3 Collaboration, OPAL Collaboration, SLD Collaboration, LEP Electroweak Working Group, SLD Electroweak Group, and SLD Heavy Flavour Group), Phys. Rep. **427**, 257 (2006).
[40] ATLAS Collaboration, Phys. Rev. D **86**, 032003 (2012).
[41] ATLAS and CMS Collaborations, Reports No. ATL-PHYS-PUB-2011-011 and No. CERN-CMS-NOTE-2011-005, 2011, http://cds.cern.ch/record/1375842.
[42] L. Moneta *et al.*, *Proc. Sci.*, ACAT2010 (2010) 057 [arXiv:1009.1003].
[43] K. Cranmer *et al.*, Report No. CERN-OPEN-2012-016, 2012 [http://cdsweb.cern.ch/record/1456844].
[44] W. Verkerke and D. P. Kirkby, *The RooFit Toolkit for Data Modeling* eConf C 0303241, MOLT007 (2003) [arXiv:physics/0306116].
[45] G. Cowan, K. Cranmer, E. Gross, and O. Vitells, Eur. Phys. J. C **71**, 1554 (2011).

G. Aad,[84] B. Abbott,[112] J. Abdallah,[152] S. Abdel Khalek,[116] O. Abdinov,[11] R. Aben,[106] B. Abi,[113] S. H. Abidi,[159] M. Abolins,[89] O. S. AbouZeid,[159] H. Abramowicz,[154] H. Abreu,[153] R. Abreu,[30] Y. Abulaiti,[147a,147b] B. S. Acharya,[165a,165b,b] L. Adamczyk,[38a] D. L. Adams,[25] J. Adelman,[177] S. Adomeit,[99] T. Adye,[130] T. Agatonovic-Jovin,[13a] J. A. Aguilar-Saavedra,[125a,125f] M. Agustoni,[17] S. P. Ahlen,[22] F. Ahmadov,[64,c] G. Aielli,[134a,134b] H. Akerstedt,[147a,147b] T. P. A. Åkesson,[80] G. Akimoto,[156] A. V. Akimov,[95] G. L. Alberghi,[20a,20b] J. Albert,[170] S. Albrand,[55] M. J. Alconada Verzini,[70] M. Aleksa,[30] I. N. Aleksandrov,[64] C. Alexa,[26a] G. Alexander,[154] G. Alexandre,[49] T. Alexopoulos,[10] M. Alhroob,[165a,165c] G. Alimonti,[90a] L. Alio,[84] J. Alison,[31] B. M. M. Allbrooke,[18] L. J. Allison,[71] P. P. Allport,[73] J. Almond,[83] A. Aloisio,[103a,103b] A. Alonso,[36] F. Alonso,[70] C. Alpigiani,[75] A. Altheimer,[35] B. Alvarez Gonzalez,[89] M. G. Alviggi,[103a,103b] K. Amako,[65] Y. Amaral Coutinho,[24a] C. Amelung,[23] D. Amidei,[88] S. P. Amor Dos Santos,[125a,125c] A. Amorim,[125a,125b] S. Amoroso,[48] N. Amram,[154] G. Amundsen,[23] C. Anastopoulos,[140] L. S. Ancu,[49] N. Andari,[30] T. Andeen,[35] C. F. Anders,[58b] G. Anders,[30] K. J. Anderson,[31] A. Andreazza,[90a,90b] V. Andrei,[58a] X. S. Anduaga,[70] S. Angelidakis,[9] I. Angelozzi,[106] P. Anger,[44] A. Angerami,[35] F. Anghinolfi,[30] A. V. Anisenkov,[108] N. Anjos,[125a] A. Annovi,[47] A. Antonaki,[9] M. Antonelli,[47] A. Antonov,[97] J. Antos,[145b] F. Anulli,[133a] M. Aoki,[65] L. Aperio Bella,[18] R. Apolle,[119,d] G. Arabidze,[89] I. Aracena,[144] Y. Arai,[65] J. P. Araque,[125a] A. T. H. Arce,[45] J-F. Arguin,[94] S. Argyropoulos,[42] M. Arik,[19a] A. J. Armbruster,[30] O. Arnaez,[30]

V. Arnal,[81] H. Arnold,[48] M. Arratia,[28] O. Arslan,[21] A. Artamonov,[96] G. Artoni,[23] S. Asai,[156] N. Asbah,[42] A. Ashkenazi,[154] B. Åsman,[147a,147b] L. Asquith,[6] K. Assamagan,[25] R. Astalos,[145a] M. Atkinson,[166] N. B. Atlay,[142] B. Auerbach,[6] K. Augsten,[127] M. Aurousseau,[146b] G. Avolio,[30] G. Azuelos,[94,e] Y. Azuma,[156] M. A. Baak,[30] A. Baas,[58a] C. Bacci,[135a,135b] H. Bachacou,[137] K. Bachas,[155] M. Backes,[30] M. Backhaus,[30] J. Backus Mayes,[144] E. Badescu,[26a] P. Bagiacchi,[133a,133b] P. Bagnaia,[133a,133b] Y. Bai,[33a] T. Bain,[35] J. T. Baines,[130] O. K. Baker,[177] P. Balek,[128] F. Balli,[137] E. Banas,[39] Sw. Banerjee,[174] A. A. E. Bannoura,[176] V. Bansal,[170] H. S. Bansil,[18] L. Barak,[173] S. P. Baranov,[95] E. L. Barberio,[87] D. Barberis,[50a,50b] M. Barbero,[84] T. Barillari,[100] M. Barisonzi,[176] T. Barklow,[144] N. Barlow,[28] B. M. Barnett,[130] R. M. Barnett,[15] Z. Barnovska,[5] A. Baroncelli,[135a] G. Barone,[49] A. J. Barr,[119] F. Barreiro,[81] J. Barreiro Guimarães da Costa,[57] R. Bartoldus,[144] A. E. Barton,[71] P. Bartos,[145a] V. Bartsch,[150] A. Bassalat,[116] A. Basye,[166] R. L. Bates,[53] J. R. Batley,[28] M. Battaglia,[138] M. Battistin,[30] F. Bauer,[137] H. S. Bawa,[144,f] M. D. Beattie,[71] T. Beau,[79] P. H. Beauchemin,[162] R. Beccherle,[123a,123b] P. Bechtle,[21] H. P. Beck,[17] K. Becker,[176] S. Becker,[99] M. Beckingham,[171] C. Becot,[116] A. J. Beddall,[19c] A. Beddall,[19c] S. Bedikian,[177] V. A. Bednyakov,[64] C. P. Bee,[149] L. J. Beemster,[106] T. A. Beermann,[176] M. Begel,[25] K. Behr,[119] C. Belanger-Champagne,[86] P. J. Bell,[49] W. H. Bell,[49] G. Bella,[154] L. Bellagamba,[20a] A. Bellerive,[29] M. Bellomo,[85] K. Belotskiy,[97] O. Beltramello,[30] O. Benary,[154] D. Benchekroun,[136a] K. Bendtz,[147a,147b] N. Benekos,[166] Y. Benhammou,[154] E. Benhar Noccioli,[49] J. A. Benitez Garcia,[160b] D. P. Benjamin,[45] J. R. Bensinger,[23] K. Benslama,[131] S. Bentvelsen,[106] D. Berge,[106] E. Bergeaas Kuutmann,[16] N. Berger,[5] F. Berghaus,[170] J. Beringer,[15] C. Bernard,[22] P. Bernat,[77] C. Bernius,[78] F. U. Bernlochner,[170] T. Berry,[76] P. Berta,[128] C. Bertella,[84] G. Bertoli,[147a,147b] F. Bertolucci,[123a,123b] C. Bertsche,[112] D. Bertsche,[112] M. I. Besana,[90a] G. J. Besjes,[105] O. Bessidskaia,[147a,147b] M. F. Bessner,[42] N. Besson,[137] C. Betancourt,[48] S. Bethke,[100] W. Bhimji,[46] R. M. Bianchi,[124] L. Bianchini,[23] M. Bianco,[30] O. Biebel,[99] S. P. Bieniek,[77] K. Bierwagen,[54] J. Biesiada,[15] M. Biglietti,[135a] J. Bilbao De Mendizabal,[49] H. Bilokon,[47] M. Bindi,[54] S. Binet,[116] A. Bingul,[19c] C. Bini,[133a,133b] C. W. Black,[151] J. E. Black,[144] K. M. Black,[22] D. Blackburn,[139] R. E. Blair,[6] J.-B. Blanchard,[137] T. Blazek,[145a] I. Bloch,[42] C. Blocker,[23] W. Blum,[82,a] U. Blumenschein,[54] G. J. Bobbink,[106] V. S. Bobrovnikov,[108] S. S. Bocchetta,[80] A. Bocci,[45] C. Bock,[99] C. R. Boddy,[119] M. Boehler,[48] T. T. Boek,[176] J. A. Bogaerts,[30] A. G. Bogdanchikov,[108] A. Bogouch,[91,a] C. Bohm,[147a] J. Bohm,[126] V. Boisvert,[76] T. Bold,[38a] V. Boldea,[26a] A. S. Boldyrev,[98] M. Bomben,[79] M. Bona,[75] M. Boonekamp,[137] A. Borisov,[129] G. Borissov,[71] M. Borri,[83] S. Borroni,[42] J. Bortfeldt,[99] V. Bortolotto,[135a,135b] K. Bos,[106] D. Boscherini,[20a] M. Bosman,[12] H. Boterenbrood,[106] J. Boudreau,[124] J. Bouffard,[2] E. V. Bouhova-Thacker,[71] D. Boumediene,[34] C. Bourdarios,[116] N. Bousson,[113] S. Boutouil,[136d] A. Boveia,[31] J. Boyd,[30] I. R. Boyko,[64] J. Bracinik,[18] A. Brandt,[8] G. Brandt,[15] O. Brandt,[58a] U. Bratzler,[157] B. Brau,[85] J. E. Brau,[115] H. M. Braun,[176,a] S. F. Brazzale,[165a,165c] B. Brelier,[159] K. Brendlinger,[121] A. J. Brennan,[87] R. Brenner,[167] S. Bressler,[173] K. Bristow,[146c] T. M. Bristow,[46] D. Britton,[53] F. M. Brochu,[28] I. Brock,[21] R. Brock,[89] C. Bromberg,[89] J. Bronner,[100] G. Brooijmans,[35] T. Brooks,[76] W. K. Brooks,[32b] J. Brosamer,[15] E. Brost,[115] J. Brown,[55] P. A. Bruckman de Renstrom,[39] D. Bruncko,[145b] R. Bruneliere,[48] S. Brunet,[60] A. Bruni,[20a] G. Bruni,[20a] M. Bruschi,[20a] L. Bryngemark,[80] T. Buanes,[14] Q. Buat,[143] F. Bucci,[49] P. Buchholz,[142] R. M. Buckingham,[119] A. G. Buckley,[53] S. I. Buda,[26a] I. A. Budagov,[64] F. Buehrer,[48] L. Bugge,[118] M. K. Bugge,[118] O. Bulekov,[97] A. C. Bundock,[73] H. Burckhart,[30] S. Burdin,[73] B. Burghgrave,[107] S. Burke,[130] I. Burmeister,[43] E. Busato,[34] D. Büscher,[48] V. Büscher,[82] P. Bussey,[53] C. P. Buszello,[167] B. Butler,[57] J. M. Butler,[22] A. I. Butt,[3] C. M. Buttar,[53] J. M. Butterworth,[77] P. Butti,[106] W. Buttinger,[28] A. Buzatu,[53] M. Byszewski,[10] S. Cabrera Urbán,[168] D. Caforio,[20a,20b] O. Cakir,[4a] P. Calafiura,[15] A. Calandri,[137] G. Calderini,[79] P. Calfayan,[99] R. Calkins,[107] L. P. Caloba,[24a] D. Calvet,[34] S. Calvet,[34] R. Camacho Toro,[49] S. Camarda,[42] D. Cameron,[118] L. M. Caminada,[15] R. Caminal Armadans,[12] S. Campana,[30] M. Campanelli,[77] A. Campoverde,[149] V. Canale,[103a,103b] A. Canepa,[160a] M. Cano Bret,[75] J. Cantero,[81] R. Cantrill,[125a] T. Cao,[40] M. D. M. Capeans Garrido,[30] I. Caprini,[26a] M. Caprini,[26a] M. Capua,[37a,37b] R. Caputo,[82] R. Cardarelli,[134a] T. Carli,[30] G. Carlino,[103a] L. Carminati,[90a,90b] S. Caron,[105] E. Carquin,[32a] G. D. Carrillo-Montoya,[146c] J. R. Carter,[28] J. Carvalho,[125a,125c] D. Casadei,[77] M. P. Casado,[12] M. Casolino,[12] E. Castaneda-Miranda,[146b] A. Castelli,[106] V. Castillo Gimenez,[168] N. F. Castro,[125a] P. Catastini,[57] A. Catinaccio,[30] J. R. Catmore,[118] A. Cattai,[30] G. Cattani,[134a,134b] S. Caughron,[89] V. Cavaliere,[166] D. Cavalli,[90a] M. Cavalli-Sforza,[12] V. Cavasinni,[123a,123b] F. Ceradini,[135a,135b] B. Cerio,[45] K. Cerny,[128] A. S. Cerqueira,[24b] A. Cerri,[150] L. Cerrito,[75] F. Cerutti,[15] M. Cerv,[30] A. Cervelli,[17] S. A. Cetin,[19b] A. Chafaq,[136a] D. Chakraborty,[107] I. Chalupkova,[128] P. Chang,[166] B. Chapleau,[86] J. D. Chapman,[28] D. Charfeddine,[116] D. G. Charlton,[18] C. C. Chau,[159] C. A. Chavez Barajas,[150] S. Cheatham,[86] A. Chegwidden,[89] S. Chekanov,[6] S. V. Chekulaev,[160a] G. A. Chelkov,[64,g] M. A. Chelstowska,[88] C. Chen,[63] H. Chen,[25] K. Chen,[149] L. Chen,[33d,h] S. Chen,[33c] X. Chen,[146c] Y. Chen,[66] Y. Chen,[35] H. C. Cheng,[88] Y. Cheng,[31] A. Cheplakov,[64] R. Cherkaoui El Moursli,[136e] V. Chernyatin,[25,a] E. Cheu,[7]

L. Chevalier,[137] V. Chiarella,[47] G. Chiefari,[103a,103b] J. T. Childers,[6] A. Chilingarov,[71] G. Chiodini,[72a] A. S. Chisholm,[18] R. T. Chislett,[77] A. Chitan,[26a] M. V. Chizhov,[64] S. Chouridou,[9] B. K. B. Chow,[99] D. Chromek-Burckhart,[30] M. L. Chu,[152] J. Chudoba,[126] J. J. Chwastowski,[39] L. Chytka,[114] G. Ciapetti,[133a,133b] A. K. Ciftci,[4a] R. Ciftci,[4a] D. Cinca,[53] V. Cindro,[74] A. Ciocio,[15] P. Cirkovic,[13b] Z. H. Citron,[173] M. Citterio,[90a] M. Ciubancan,[26a] A. Clark,[49] P. J. Clark,[46] R. N. Clarke,[15] W. Cleland,[124] J. C. Clemens,[84] C. Clement,[147a,147b] Y. Coadou,[84] M. Cobal,[165a,165c] A. Coccaro,[139] J. Cochran,[63] L. Coffey,[23] J. G. Cogan,[144] J. Coggeshall,[166] B. Cole,[35] S. Cole,[107] A. P. Colijn,[106] J. Collot,[55] T. Colombo,[58c] G. Colon,[85] G. Compostella,[100] P. Conde Muiño,[125a,125b] E. Coniavitis,[48] M. C. Conidi,[12] S. H. Connell,[146b] I. A. Connelly,[76] S. M. Consonni,[90a,90b] V. Consorti,[48] S. Constantinescu,[26a] C. Conta,[120a,120b] G. Conti,[57] F. Conventi,[103a,i] M. Cooke,[15] B. D. Cooper,[77] A. M. Cooper-Sarkar,[119] N. J. Cooper-Smith,[76] K. Copic,[15] T. Cornelissen,[176] M. Corradi,[20a] F. Corriveau,[86,j] A. Corso-Radu,[164] A. Cortes-Gonzalez,[12] G. Cortiana,[100] G. Costa,[90a] M. J. Costa,[168] D. Costanzo,[140] D. Côté,[8] G. Cottin,[28] G. Cowan,[76] B. E. Cox,[83] K. Cranmer,[109] G. Cree,[29] S. Crépé-Renaudin,[55] F. Crescioli,[79] W. A. Cribbs,[147a,147b] M. Crispin Ortuzar,[119] M. Cristinziani,[21] V. Croft,[105] G. Crosetti,[37a,37b] C.-M. Cuciuc,[26a] T. Cuhadar Donszelmann,[140] J. Cummings,[177] M. Curatolo,[47] C. Cuthbert,[151] H. Czirr,[142] P. Czodrowski,[3] Z. Czyczula,[177] S. D'Auria,[53] M. D'Onofrio,[73] M. J. Da Cunha Sargedas De Sousa,[125a,125b] C. Da Via,[83] W. Dabrowski,[38a] A. Dafinca,[119] T. Dai,[88] O. Dale,[14] F. Dallaire,[94] C. Dallapiccola,[85] M. Dam,[36] A. C. Daniells,[18] M. Dano Hoffmann,[137] V. Dao,[48] G. Darbo,[50a] S. Darmora,[8] J. A. Dassoulas,[42] A. Dattagupta,[60] W. Davey,[21] C. David,[170] T. Davidek,[128] E. Davies,[119,d] M. Davies,[154] O. Davignon,[79] A. R. Davison,[77] P. Davison,[77] Y. Davygora,[58a] E. Dawe,[143] I. Dawson,[140] R. K. Daya-Ishmukhametova,[85] K. De,[8] R. de Asmundis,[103a] S. De Castro,[20a,20b] S. De Cecco,[79] N. De Groot,[105] P. de Jong,[106] H. De la Torre,[81] F. De Lorenzi,[63] L. De Nooij,[106] D. De Pedis,[133a] A. De Salvo,[133a] U. De Sanctis,[165a,165b] A. De Santo,[150] J. B. De Vivie De Regie,[116] W. J. Dearnaley,[71] R. Debbe,[25] C. Debenedetti,[138] B. Dechenaux,[55] D. V. Dedovich,[64] I. Deigaard,[106] J. Del Peso,[81] T. Del Prete,[123a,123b] F. Deliot,[137] C. M. Delitzsch,[49] M. Deliyergiyev,[74] A. Dell'Acqua,[30] L. Dell'Asta,[22] M. Dell'Orso,[123a,123b] M. Della Pietra,[103a,i] D. della Volpe,[49] M. Delmastro,[5] P. A. Delsart,[55] C. Deluca,[106] S. Demers,[177] M. Demichev,[64] A. Demilly,[79] S. P. Denisov,[129] D. Derendarz,[39] J. E. Derkaoui,[136d] F. Derue,[79] P. Dervan,[73] K. Desch,[21] C. Deterre,[42] P. O. Deviveiros,[106] A. Dewhurst,[130] S. Dhaliwal,[106] A. Di Ciaccio,[134a,134b] L. Di Ciaccio,[5] A. Di Domenico,[133a,133b] C. Di Donato,[103a,103b] A. Di Girolamo,[30] B. Di Girolamo,[30] A. Di Mattia,[153] B. Di Micco,[135a,135b] R. Di Nardo,[47] A. Di Simone,[48] R. Di Sipio,[20a,20b] D. Di Valentino,[29] F. A. Dias,[46] M. A. Diaz,[32a] E. B. Diehl,[88] J. Dietrich,[42] T. A. Dietzsch,[58a] S. Diglio,[84] A. Dimitrievska,[13a] J. Dingfelder,[21] C. Dionisi,[133a,133b] P. Dita,[26a] S. Dita,[26a] F. Dittus,[30] F. Djama,[84] T. Djobava,[51b] M. A. B. do Vale,[24c] A. Do Valle Wemans,[125a,125g] T. K. O. Doan,[5] D. Dobos,[30] C. Doglioni,[49] T. Doherty,[53] T. Dohmae,[156] J. Dolejsi,[128] Z. Dolezal,[128] B. A. Dolgoshein,[97,a] M. Donadelli,[24d] S. Donati,[123a,123b] P. Dondero,[120a,120b] J. Donini,[34] J. Dopke,[130] A. Doria,[103a] M. T. Dova,[70] A. T. Doyle,[53] M. Dris,[10] J. Dubbert,[88] S. Dube,[15] E. Dubreuil,[34] E. Duchovni,[173] G. Duckeck,[99] O. A. Ducu,[26a] D. Duda,[176] A. Dudarev,[30] F. Dudziak,[63] L. Duflot,[116] L. Duguid,[76] M. Dührssen,[30] M. Dunford,[58a] H. Duran Yildiz,[4a] M. Düren,[52] A. Durglishvili,[51b] M. Dwuznik,[38a] M. Dyndal,[38a] J. Ebke,[99] W. Edson,[2] N. C. Edwards,[46] W. Ehrenfeld,[21] T. Eifert,[144] G. Eigen,[14] K. Einsweiler,[15] T. Ekelof,[167] M. El Kacimi,[136c] M. Ellert,[167] S. Elles,[5] F. Ellinghaus,[82] N. Ellis,[30] J. Elmsheuser,[99] M. Elsing,[30] D. Emeliyanov,[130] Y. Enari,[156] O. C. Endner,[82] M. Endo,[117] R. Engelmann,[149] J. Erdmann,[177] A. Ereditato,[17] D. Eriksson,[147a] G. Ernis,[176] J. Ernst,[2] M. Ernst,[25] J. Ernwein,[137] D. Errede,[166] S. Errede,[166] E. Ertel,[82] M. Escalier,[116] H. Esch,[43] C. Escobar,[124] B. Esposito,[47] A. I. Etienvre,[137] E. Etzion,[154] H. Evans,[60] A. Ezhilov,[122] L. Fabbri,[20a,20b] G. Facini,[31] R. M. Fakhrutdinov,[129] S. Falciano,[133a] R. J. Falla,[77] J. Faltova,[128] Y. Fang,[33a] M. Fanti,[90a,90b] A. Farbin,[8] A. Farilla,[135a] T. Farooque,[12] S. Farrell,[15] S. M. Farrington,[171] P. Farthouat,[30] F. Fassi,[136e] P. Fassnacht,[30] D. Fassouliotis,[9] A. Favareto,[50a,50b] L. Fayard,[116] P. Federic,[145a] O. L. Fedin,[122,k] W. Fedorko,[169] M. Fehling-Kaschek,[48] S. Feigl,[30] L. Feligioni,[84] C. Feng,[33d] E. J. Feng,[6] H. Feng,[88] A. B. Fenyuk,[129] S. Fernandez Perez,[30] S. Ferrag,[53] J. Ferrando,[53] A. Ferrari,[167] P. Ferrari,[106] R. Ferrari,[120a] D. E. Ferreira de Lima,[53] A. Ferrer,[168] D. Ferrere,[49] C. Ferretti,[88] A. Ferretto Parodi,[50a,50b] M. Fiascaris,[31] F. Fiedler,[82] A. Filipčič,[74] M. Filipuzzi,[42] F. Filthaut,[105] M. Fincke-Keeler,[170] K. D. Finelli,[151] M. C. N. Fiolhais,[125a,125c] L. Fiorini,[168] A. Firan,[40] A. Fischer,[2] J. Fischer,[176] W. C. Fisher,[89] E. A. Fitzgerald,[23] M. Flechl,[48] I. Fleck,[142] P. Fleischmann,[88] S. Fleischmann,[176] G. T. Fletcher,[140] G. Fletcher,[75] T. Flick,[176] A. Floderus,[80] L. R. Flores Castillo,[174,l] A. C. Florez Bustos,[160b] M. J. Flowerdew,[100] A. Formica,[137] A. Forti,[83] D. Fortin,[160a] D. Fournier,[116] H. Fox,[71] S. Fracchia,[12] P. Francavilla,[79] M. Franchini,[20a,20b] S. Franchino,[30] D. Francis,[30] L. Franconi,[118] M. Franklin,[57] S. Franz,[61] M. Fraternali,[120a,120b] S. T. French,[28] C. Friedrich,[42] F. Friedrich,[44] D. Froidevaux,[30] J. A. Frost,[28] C. Fukunaga,[157] E. Fullana Torregrosa,[82] B. G. Fulsom,[144] J. Fuster,[168] C. Gabaldon,[55] O. Gabizon,[173] A. Gabrielli,[20a,20b]

A. Gabrielli,[133a,133b] S. Gadatsch,[106] S. Gadomski,[49] G. Gagliardi,[50a,50b] P. Gagnon,[60] C. Galea,[105] B. Galhardo,[125a,125c] E. J. Gallas,[119] V. Gallo,[17] B. J. Gallop,[130] P. Gallus,[127] G. Galster,[36] K. K. Gan,[110] J. Gao,[33b,h] Y. S. Gao,[144,f] F. M. Garay Walls,[46] F. Garberson,[177] C. García,[168] J. E. García Navarro,[168] M. Garcia-Sciveres,[15] R. W. Gardner,[31] N. Garelli,[144] V. Garonne,[30] C. Gatti,[47] G. Gaudio,[120a] B. Gaur,[142] L. Gauthier,[94] P. Gauzzi,[133a,133b] I. L. Gavrilenko,[95] C. Gay,[169] G. Gaycken,[21] E. N. Gazis,[10] P. Ge,[33d] Z. Gecse,[169] C. N. P. Gee,[130] D. A. A. Geerts,[106] Ch. Geich-Gimbel,[21] K. Gellerstedt,[147a,147b] C. Gemme,[50a] A. Gemmell,[53] M. H. Genest,[55] S. Gentile,[133a,133b] M. George,[54] S. George,[76] D. Gerbaudo,[164] A. Gershon,[154] H. Ghazlane,[136b] N. Ghodbane,[34] B. Giacobbe,[20a] S. Giagu,[133a,133b] V. Giangiobbe,[12] P. Giannetti,[123a,123b] F. Gianotti,[30] B. Gibbard,[25] S. M. Gibson,[76] M. Gilchriese,[15] T. P. S. Gillam,[28] D. Gillberg,[30] G. Gilles,[34] D. M. Gingrich,[3,e] N. Giokaris,[9] M. P. Giordani,[165a,165c] R. Giordano,[103a,103b] F. M. Giorgi,[20a] F. M. Giorgi,[16] P. F. Giraud,[137] D. Giugni,[90a] C. Giuliani,[48] M. Giulini,[58b] B. K. Gjelsten,[118] S. Gkaitatzis,[155] I. Gkialas,[155,m] L. K. Gladilin,[98] C. Glasman,[81] J. Glatzer,[30] P. C. F. Glaysher,[46] A. Glazov,[42] G. L. Glonti,[64] M. Goblirsch-Kolb,[100] J. R. Goddard,[75] J. Godfrey,[143] J. Godlewski,[30] C. Goeringer,[82] S. Goldfarb,[88] T. Golling,[177] D. Golubkov,[129] A. Gomes,[125a,125b,125d] L. S. Gomez Fajardo,[42] R. Gonçalo,[125a] J. Goncalves Pinto Firmino Da Costa,[137] L. Gonella,[21] S. González de la Hoz,[168] G. Gonzalez Parra,[12] S. Gonzalez-Sevilla,[49] L. Goossens,[30] P. A. Gorbounov,[96] H. A. Gordon,[25] I. Gorelov,[104] B. Gorini,[30] E. Gorini,[72a,72b] A. Gorišek,[74] E. Gornicki,[39] A. T. Goshaw,[6] C. Gössling,[43] M. I. Gostkin,[64] M. Gouighri,[136a] D. Goujdami,[136c] M. P. Goulette,[49] A. G. Goussiou,[139] C. Goy,[5] S. Gozpinar,[23] H. M. X. Grabas,[137] L. Graber,[54] I. Grabowska-Bold,[38a] P. Grafström,[20a,20b] K-J. Grahn,[42] J. Gramling,[49] E. Gramstad,[118] S. Grancagnolo,[16] V. Grassi,[149] V. Gratchev,[122] H. M. Gray,[30] E. Graziani,[135a] O. G. Grebenyuk,[122] Z. D. Greenwood,[78,n] K. Gregersen,[77] I. M. Gregor,[42] P. Grenier,[144] J. Griffiths,[8] A. A. Grillo,[138] K. Grimm,[71] S. Grinstein,[12,o] Ph. Gris,[34] Y. V. Grishkevich,[98] J.-F. Grivaz,[116] J. P. Grohs,[44] A. Grohsjean,[42] E. Gross,[173] J. Grosse-Knetter,[54] G. C. Grossi,[134a,134b] J. Groth-Jensen,[173] Z. J. Grout,[150] L. Guan,[33b] F. Guescini,[49] D. Guest,[177] O. Gueta,[154] C. Guicheney,[34] E. Guido,[50a,50b] T. Guillemin,[116] S. Guindon,[2] U. Gul,[53] C. Gumpert,[44] J. Gunther,[127] J. Guo,[35] S. Gupta,[119] P. Gutierrez,[112] N. G. Gutierrez Ortiz,[53] C. Gutschow,[77] N. Guttman,[154] C. Guyot,[137] C. Gwenlan,[119] C. B. Gwilliam,[73] A. Haas,[109] C. Haber,[15] H. K. Hadavand,[8] N. Haddad,[136e] P. Haefner,[21] S. Hageböck,[21] Z. Hajduk,[39] H. Hakobyan,[178] M. Haleem,[42] D. Hall,[119] G. Halladjian,[89] K. Hamacher,[176] P. Hamal,[114] K. Hamano,[170] M. Hamer,[54] A. Hamilton,[146a] S. Hamilton,[162] G. N. Hamity,[146c] P. G. Hamnett,[42] L. Han,[33b] K. Hanagaki,[117] K. Hanawa,[156] M. Hance,[15] P. Hanke,[58a] R. Hanna,[137] J. B. Hansen,[36] J. D. Hansen,[36] P. H. Hansen,[36] K. Hara,[161] A. S. Hard,[174] T. Harenberg,[176] F. Hariri,[116] S. Harkusha,[91] D. Harper,[88] R. D. Harrington,[46] O. M. Harris,[139] P. F. Harrison,[171] F. Hartjes,[106] M. Hasegawa,[66] S. Hasegawa,[102] Y. Hasegawa,[141] A. Hasib,[112] S. Hassani,[137] S. Haug,[17] M. Hauschild,[30] R. Hauser,[89] M. Havranek,[126] C. M. Hawkes,[18] R. J. Hawkings,[30] A. D. Hawkins,[80] T. Hayashi,[161] D. Hayden,[89] C. P. Hays,[119] H. S. Hayward,[73] S. J. Haywood,[130] S. J. Head,[18] T. Heck,[82] V. Hedberg,[80] L. Heelan,[8] S. Heim,[121] T. Heim,[176] B. Heinemann,[15] L. Heinrich,[109] J. Hejbal,[126] L. Helary,[22] C. Heller,[99] M. Heller,[30] S. Hellman,[147a,147b] D. Hellmich,[21] C. Helsens,[30] J. Henderson,[119] R. C. W. Henderson,[71] Y. Heng,[174] C. Hengler,[42] A. Henrichs,[177] A. M. Henriques Correia,[30] S. Henrot-Versille,[116] C. Hensel,[54] G. H. Herbert,[16] Y. Hernández Jiménez,[168] R. Herrberg-Schubert,[16] G. Herten,[48] R. Hertenberger,[99] L. Hervas,[30] G. G. Hesketh,[77] N. P. Hessey,[106] R. Hickling,[75] E. Higón-Rodriguez,[168] E. Hill,[170] J. C. Hill,[28] K. H. Hiller,[42] S. Hillert,[21] S. J. Hillier,[18] I. Hinchliffe,[15] E. Hines,[121] M. Hirose,[158] D. Hirschbuehl,[176] J. Hobbs,[149] N. Hod,[106] M. C. Hodgkinson,[140] P. Hodgson,[140] A. Hoecker,[30] M. R. Hoeferkamp,[104] F. Hoenig,[99] J. Hoffman,[40] D. Hoffmann,[84] J. I. Hofmann,[58a] M. Hohlfeld,[82] T. R. Holmes,[15] T. M. Hong,[121] L. Hooft van Huysduynen,[109] Y. Horii,[102] J-Y. Hostachy,[55] S. Hou,[152] A. Hoummada,[136a] J. Howard,[119] J. Howarth,[42] M. Hrabovsky,[114] I. Hristova,[16] J. Hrivnac,[116] T. Hryn'ova,[5] C. Hsu,[146c] P. J. Hsu,[82] S.-C. Hsu,[139] D. Hu,[35] X. Hu,[25] Y. Huang,[42] Z. Hubacek,[30] F. Hubaut,[84] F. Huegging,[21] T. B. Huffman,[119] E. W. Hughes,[35] G. Hughes,[71] M. Huhtinen,[30] T. A. Hülsing,[82] M. Hurwitz,[15] N. Huseynov,[64,c] J. Huston,[89] J. Huth,[57] G. Iacobucci,[49] G. Iakovidis,[10] I. Ibragimov,[142] L. Iconomidou-Fayard,[116] E. Ideal,[177] P. Iengo,[103a] O. Igonkina,[106] T. Iizawa,[172] Y. Ikegami,[65] K. Ikematsu,[142] M. Ikeno,[65] Y. Ilchenko,[31,cc] D. Iliadis,[155] N. Ilic,[159] Y. Inamaru,[66] T. Ince,[100] P. Ioannou,[9] M. Iodice,[135a] K. Iordanidou,[9] V. Ippolito,[57] A. Irles Quiles,[168] C. Isaksson,[167] M. Ishino,[67] M. Ishitsuka,[158] R. Ishmukhametov,[110] C. Issever,[119] S. Istin,[19a] J. M. Iturbe Ponce,[83] R. Iuppa,[134a,134b] J. Ivarsson,[80] W. Iwanski,[39] H. Iwasaki,[65] J. M. Izen,[41] V. Izzo,[103a] B. Jackson,[121] M. Jackson,[73] P. Jackson,[1] M. R. Jaekel,[30] V. Jain,[2] K. Jakobs,[48] S. Jakobsen,[30] T. Jakoubek,[126] J. Jakubek,[127] D. O. Jamin,[152] D. K. Jana,[78] E. Jansen,[77] H. Jansen,[30] J. Janssen,[21] M. Janus,[171] G. Jarlskog,[80] N. Javadov,[64,c] T. Javůrek,[48] L. Jeanty,[15] J. Jejelava,[51a,p] G.-Y. Jeng,[151] D. Jennens,[87] P. Jenni,[48,q] J. Jentzsch,[43] C. Jeske,[171] S. Jézéquel,[5] H. Ji,[174] J. Jia,[149] Y. Jiang,[33b] M. Jimenez Belenguer,[42] S. Jin,[33a] A. Jinaru,[26a] O. Jinnouchi,[158] M. D. Joergensen,[36]

K. E. Johansson,[147a,147b] P. Johansson,[140] K. A. Johns,[7] K. Jon-And,[147a,147b] G. Jones,[171] R. W. L. Jones,[71] T. J. Jones,[73] J. Jongmanns,[58a] P. M. Jorge,[125a,125b] K. D. Joshi,[83] J. Jovicevic,[148] X. Ju,[174] C. A. Jung,[43] R. M. Jungst,[30] P. Jussel,[61] A. Juste Rozas,[12,o] M. Kaci,[168] A. Kaczmarska,[39] M. Kado,[116] H. Kagan,[110] M. Kagan,[144] E. Kajomovitz,[45] C. W. Kalderon,[119] S. Kama,[40] A. Kamenshchikov,[129] N. Kanaya,[156] M. Kaneda,[30] S. Kaneti,[28] V. A. Kantserov,[97] J. Kanzaki,[65] B. Kaplan,[109] L. S. Kaplan,[174] A. Kapliy,[31] D. Kar,[53] K. Karakostas,[10] N. Karastathis,[10] M. Karnevskiy,[82] S. N. Karpov,[64] Z. M. Karpova,[64] K. Karthik,[109] V. Kartvelishvili,[71] A. N. Karyukhin,[129] L. Kashif,[174] G. Kasieczka,[58b] R. D. Kass,[110] A. Kastanas,[14] Y. Kataoka,[156] A. Katre,[49] J. Katzy,[42] V. Kaushik,[7] K. Kawagoe,[69] T. Kawamoto,[156] G. Kawamura,[54] S. Kazama,[156] V. F. Kazanin,[108] M. Y. Kazarinov,[64] R. Keeler,[170] R. Kehoe,[40] M. Keil,[54] J. S. Keller,[42] J. J. Kempster,[76] H. Keoshkerian,[5] O. Kepka,[126] B. P. Kerševan,[74] S. Kersten,[176] K. Kessoku,[156] J. Keung,[159] F. Khalil-zada,[11] H. Khandanyan,[147a,147b] A. Khanov,[113] A. Khodinov,[97] A. Khomich,[58a] T. J. Khoo,[28] G. Khoriauli,[21] A. Khoroshilov,[176] V. Khovanskiy,[96] E. Khramov,[64] J. Khubua,[51b] H. Y. Kim,[8] H. Kim,[147a,147b] S. H. Kim,[161] N. Kimura,[172] O. Kind,[16] B. T. King,[73] M. King,[168] R. S. B. King,[119] S. B. King,[169] J. Kirk,[130] A. E. Kiryunin,[100] T. Kishimoto,[66] D. Kisielewska,[38a] F. Kiss,[48] T. Kittelmann,[124] K. Kiuchi,[161] E. Kladiva,[145b] M. Klein,[73] U. Klein,[73] K. Kleinknecht,[82] P. Klimek,[147a,147b] A. Klimentov,[25] R. Klingenberg,[43] J. A. Klinger,[83] T. Klioutchnikova,[30] P. F. Klok,[105] E.-E. Kluge,[58a] P. Kluit,[106] S. Kluth,[100] E. Kneringer,[61] E. B. F. G. Knoops,[84] A. Knue,[53] D. Kobayashi,[158] T. Kobayashi,[156] M. Kobel,[44] M. Kocian,[144] P. Kodys,[128] P. Koevesarki,[21] T. Koffas,[29] E. Koffeman,[106] L. A. Kogan,[119] S. Kohlmann,[176] Z. Kohout,[127] T. Kohriki,[65] T. Koi,[144] H. Kolanoski,[16] I. Koletsou,[5] J. Koll,[89] A. A. Komar,[95,a] Y. Komori,[156] T. Kondo,[65] N. Kondrashova,[42] K. Köneke,[48] A. C. König,[105] S. König,[82] T. Kono,[65,r] R. Konoplich,[109,s] N. Konstantinidis,[77] R. Kopeliansky,[153] S. Koperny,[38a] L. Köpke,[82] A. K. Kopp,[48] K. Korcyl,[39] K. Kordas,[155] A. Korn,[77] A. A. Korol,[108,t] I. Korolkov,[12] E. V. Korolkova,[140] V. A. Korotkov,[129] O. Kortner,[100] S. Kortner,[100] V. V. Kostyukhin,[21] V. M. Kotov,[64] A. Kotwal,[45] C. Kourkoumelis,[9] V. Kouskoura,[155] A. Koutsman,[160a] R. Kowalewski,[170] T. Z. Kowalski,[38a] W. Kozanecki,[137] A. S. Kozhin,[129] V. Kral,[127] V. A. Kramarenko,[98] G. Kramberger,[74] D. Krasnopevtsev,[97] A. Krasznahorkay,[30] J. K. Kraus,[21] A. Kravchenko,[25] S. Kreiss,[109] M. Kretz,[58c] J. Kretzschmar,[73] K. Kreutzfeldt,[52] P. Krieger,[159] K. Kroeninger,[54] H. Kroha,[100] J. Kroll,[121] J. Kroseberg,[21] J. Krstic,[13a] U. Kruchonak,[64] H. Krüger,[21] T. Kruker,[17] N. Krumnack,[63] Z. V. Krumshteyn,[64] A. Kruse,[174] M. C. Kruse,[45] M. Kruskal,[22] T. Kubota,[87] S. Kuday,[4a] S. Kuehn,[48] A. Kugel,[58c] A. Kuhl,[138] T. Kuhl,[42] V. Kukhtin,[64] Y. Kulchitsky,[91] S. Kuleshov,[32b] M. Kuna,[133a,133b] J. Kunkle,[121] A. Kupco,[126] H. Kurashige,[66] Y. A. Kurochkin,[91] R. Kurumida,[66] V. Kus,[126] E. S. Kuwertz,[148] M. Kuze,[158] J. Kvita,[114] A. La Rosa,[49] L. La Rotonda,[37a,37b] C. Lacasta,[168] F. Lacava,[133a,133b] J. Lacey,[29] H. Lacker,[16] D. Lacour,[79] V. R. Lacuesta,[168] E. Ladygin,[64] R. Lafaye,[5] B. Laforge,[79] T. Lagouri,[177] S. Lai,[48] H. Laier,[58a] L. Lambourne,[77] S. Lammers,[60] C. L. Lampen,[7] W. Lampl,[7] E. Lançon,[137] U. Landgraf,[48] M. P. J. Landon,[75] V. S. Lang,[58a] A. J. Lankford,[164] F. Lanni,[25] K. Lantzsch,[30] S. Laplace,[79] C. Lapoire,[21] J. F. Laporte,[137] T. Lari,[90a] M. Lassnig,[30] P. Laurelli,[47] W. Lavrijsen,[15] A. T. Law,[138] P. Laycock,[73] O. Le Dortz,[79] E. Le Guirriec,[84] E. Le Menedeu,[12] T. LeCompte,[6] F. Ledroit-Guillon,[55] C. A. Lee,[152] H. Lee,[106] J. S. H. Lee,[117] S. C. Lee,[152] L. Lee,[177] G. Lefebvre,[79] M. Lefebvre,[170] F. Legger,[99] C. Leggett,[15] A. Lehan,[73] M. Lehmacher,[21] G. Lehmann Miotto,[30] X. Lei,[7] W. A. Leight,[29] A. Leisos,[155] A. G. Leister,[177] M. A. L. Leite,[24d] R. Leitner,[128] D. Lellouch,[173] B. Lemmer,[54] K. J. C. Leney,[77] T. Lenz,[21] G. Lenzen,[176] B. Lenzi,[30] R. Leone,[7] S. Leone,[123a,123b] K. Leonhardt,[44] C. Leonidopoulos,[46] S. Leontsinis,[10] C. Leroy,[94] C. G. Lester,[28] C. M. Lester,[121] M. Levchenko,[122] J. Levêque,[5] D. Levin,[88] L. J. Levinson,[173] M. Levy,[18] A. Lewis,[119] G. H. Lewis,[109] A. M. Leyko,[21] M. Leyton,[41] B. Li,[33b,u] B. Li,[84] H. Li,[149] H. L. Li,[31] L. Li,[45] L. Li,[33e] S. Li,[45] Y. Li,[33c,v] Z. Liang,[138] H. Liao,[34] B. Liberti,[134a] P. Lichard,[30] K. Lie,[166] J. Liebal,[21] W. Liebig,[14] C. Limbach,[21] A. Limosani,[87] S. C. Lin,[152,w] T. H. Lin,[82] F. Linde,[106] B. E. Lindquist,[149] J. T. Linnemann,[89] E. Lipeles,[121] A. Lipniacka,[14] M. Lisovyi,[42] T. M. Liss,[166] D. Lissauer,[25] A. Lister,[169] A. M. Litke,[138] B. Liu,[152] D. Liu,[152] J. B. Liu,[33b] K. Liu,[33b,x] L. Liu,[88] M. Liu,[45] M. Liu,[33b] Y. Liu,[33b] M. Livan,[120a,120b] S. S. A. Livermore,[119] A. Lleres,[55] J. Llorente Merino,[81] S. L. Lloyd,[75] F. Lo Sterzo,[152] E. Lobodzinska,[42] P. Loch,[7] W. S. Lockman,[138] T. Loddenkoetter,[21] F. K. Loebinger,[83] A. E. Loevschall-Jensen,[36] A. Loginov,[177] T. Lohse,[16] K. Lohwasser,[42] M. Lokajicek,[126] V. P. Lombardo,[5] B. A. Long,[22] J. D. Long,[88] R. E. Long,[71] L. Lopes,[125a] D. Lopez Mateos,[57] B. Lopez Paredes,[140] I. Lopez Paz,[12] J. Lorenz,[99] N. Lorenzo Martinez,[60] M. Losada,[163] P. Loscutoff,[15] X. Lou,[41] A. Lounis,[116] J. Love,[6] P. A. Love,[71] A. J. Lowe,[144,f] F. Lu,[33a] N. Lu,[88] H. J. Lubatti,[139] C. Luci,[133a,133b] A. Lucotte,[55] F. Luehring,[60] W. Lukas,[61] L. Luminari,[133a] O. Lundberg,[147a,147b] B. Lund-Jensen,[148] M. Lungwitz,[82] D. Lynn,[25] R. Lysak,[126] E. Lytken,[80] H. Ma,[25] L. L. Ma,[33d] G. Maccarrone,[47] A. Macchiolo,[100] J. Machado Miguens,[125a,125b] D. Macina,[30] D. Madaffari,[84] R. Madar,[48] H. J. Maddocks,[71] W. F. Mader,[44] A. Madsen,[167] M. Maeno,[8] T. Maeno,[25] E. Magradze,[54] K. Mahboubi,[48] J. Mahlstedt,[106] S. Mahmoud,[73] C. Maiani,[137]

C. Maidantchik,[24a] A. A. Maier,[100] A. Maio,[125a,125b,125d] S. Majewski,[115] Y. Makida,[65] N. Makovec,[116] P. Mal,[137,y] B. Malaescu,[79] Pa. Malecki,[39] V. P. Maleev,[122] F. Malek,[55] U. Mallik,[62] D. Malon,[6] C. Malone,[144] S. Maltezos,[10] V. M. Malyshev,[108] S. Malyukov,[30] J. Mamuzic,[13b] B. Mandelli,[30] L. Mandelli,[90a] I. Mandić,[74] R. Mandrysch,[62] J. Maneira,[125a,125b] A. Manfredini,[100] L. Manhaes de Andrade Filho,[24b] J. A. Manjarres Ramos,[160b] A. Mann,[99] P. M. Manning,[138] A. Manousakis-Katsikakis,[9] B. Mansoulie,[137] R. Mantifel,[86] L. Mapelli,[30] L. March,[168] J. F. Marchand,[29] G. Marchiori,[79] M. Marcisovsky,[126] C. P. Marino,[170] M. Marjanovic,[13a] C. N. Marques,[125a] F. Marroquim,[24a] S. P. Marsden,[83] Z. Marshall,[15] L. F. Marti,[17] S. Marti-Garcia,[168] B. Martin,[30] B. Martin,[89] T. A. Martin,[171] V. J. Martin,[46] B. Martin dit Latour,[14] H. Martinez,[137] M. Martinez,[12,o] S. Martin-Haugh,[130] A. C. Martyniuk,[77] M. Marx,[139] F. Marzano,[133a] A. Marzin,[30] L. Masetti,[82] T. Mashimo,[156] R. Mashinistov,[95] J. Masik,[83] A. L. Maslennikov,[108] I. Massa,[20a,20b] L. Massa,[20a,20b] N. Massol,[5] P. Mastrandrea,[149] A. Mastroberardino,[37a,37b] T. Masubuchi,[156] P. Mättig,[176] J. Mattmann,[82] J. Maurer,[26a] S. J. Maxfield,[73] D. A. Maximov,[108,t] R. Mazini,[152] S. M. Mazza,[90a,90b] L. Mazzaferro,[134a,134b] G. Mc Goldrick,[159] S. P. Mc Kee,[88] A. McCarn,[88] R. L. McCarthy,[149] T. G. McCarthy,[29] N. A. McCubbin,[130] K. W. McFarlane,[56,a] J. A. Mcfayden,[77] G. Mchedlidze,[54] S. J. McMahon,[130] R. A. McPherson,[170,j] A. Meade,[85] J. Mechnich,[106] M. Medinnis,[42] S. Meehan,[31] S. Mehlhase,[99] A. Mehta,[73] K. Meier,[58a] C. Meineck,[99] B. Meirose,[80] C. Melachrinos,[31] B. R. Mellado Garcia,[146c] F. Meloni,[17] A. Mengarelli,[20a,20b] S. Menke,[100] E. Meoni,[162] K. M. Mercurio,[57] S. Mergelmeyer,[21] N. Meric,[137] P. Mermod,[49] L. Merola,[103a,103b] C. Meroni,[90a] F. S. Merritt,[31] H. Merritt,[110] A. Messina,[30,z] J. Metcalfe,[25] A. S. Mete,[164] C. Meyer,[82] C. Meyer,[121] J-P. Meyer,[137] J. Meyer,[30] R. P. Middleton,[130] S. Migas,[73] L. Mijović,[21] G. Mikenberg,[173] M. Mikestikova,[126] M. Mikuž,[74] A. Milic,[30] D. W. Miller,[31] C. Mills,[46] A. Milov,[173] D. A. Milstead,[147a,147b] D. Milstein,[173] A. A. Minaenko,[129] I. A. Minashvili,[64] A. I. Mincer,[109] B. Mindur,[38a] M. Mineev,[64] Y. Ming,[174] L. M. Mir,[12] G. Mirabelli,[133a] T. Mitani,[172] J. Mitrevski,[99] V. A. Mitsou,[168] S. Mitsui,[65] A. Miucci,[49] P. S. Miyagawa,[140] J. U. Mjörnmark,[80] T. Moa,[147a,147b] K. Mochizuki,[84] S. Mohapatra,[35] W. Mohr,[48] S. Molander,[147a,147b] R. Moles-Valls,[168] K. Mönig,[42] C. Monini,[55] J. Monk,[36] E. Monnier,[84] J. Montejo Berlingen,[12] F. Monticelli,[70] S. Monzani,[133a,133b] R. W. Moore,[3] A. Moraes,[53] N. Morange,[62] D. Moreno,[82] M. Moreno Llácer,[54] P. Morettini,[50a] M. Morgenstern,[44] M. Morii,[57] S. Moritz,[82] A. K. Morley,[148] G. Mornacchi,[30] J. D. Morris,[75] L. Morvaj,[102] H. G. Moser,[100] M. Mosidze,[51b] J. Moss,[110] K. Motohashi,[158] R. Mount,[144] E. Mountricha,[25] S. V. Mouraviev,[95,a] E. J. W. Moyse,[85] S. Muanza,[84] R. D. Mudd,[18] F. Mueller,[58a] J. Mueller,[124] K. Mueller,[21] T. Mueller,[28] T. Mueller,[82] D. Muenstermann,[49] Y. Munwes,[154] J. A. Murillo Quijada,[18] W. J. Murray,[171,130] H. Musheghyan,[54] E. Musto,[153] A. G. Myagkov,[129,aa] M. Myska,[127] O. Nackenhorst,[54] J. Nadal,[54] K. Nagai,[61] R. Nagai,[158] Y. Nagai,[84] K. Nagano,[65] A. Nagarkar,[110] Y. Nagasaka,[59] M. Nagel,[100] A. M. Nairz,[30] Y. Nakahama,[30] K. Nakamura,[65] T. Nakamura,[156] I. Nakano,[111] H. Namasivayam,[41] G. Nanava,[21] R. Narayan,[58b] T. Nattermann,[21] T. Naumann,[42] G. Navarro,[163] R. Nayyar,[7] H. A. Neal,[88] P. Yu. Nechaeva,[95] T. J. Neep,[83] P. D. Nef,[144] A. Negri,[120a,120b] G. Negri,[30] M. Negrini,[20a] S. Nektarijevic,[49] A. Nelson,[164] T. K. Nelson,[144] S. Nemecek,[126] P. Nemethy,[109] A. A. Nepomuceno,[24a] M. Nessi,[30,bb] M. S. Neubauer,[166] M. Neumann,[176] R. M. Neves,[109] P. Nevski,[25] P. R. Newman,[18] D. H. Nguyen,[6] R. B. Nickerson,[119] R. Nicolaidou,[137] B. Nicquevert,[30] J. Nielsen,[138] N. Nikiforou,[35] A. Nikiforov,[16] V. Nikolaenko,[129,aa] I. Nikolic-Audit,[79] K. Nikolics,[49] K. Nikolopoulos,[18] P. Nilsson,[8] Y. Ninomiya,[156] A. Nisati,[133a] R. Nisius,[100] T. Nobe,[158] L. Nodulman,[6] M. Nomachi,[117] I. Nomidis,[29] S. Norberg,[112] M. Nordberg,[30] O. Novgorodova,[44] S. Nowak,[100] M. Nozaki,[65] L. Nozka,[114] K. Ntekas,[10] G. Nunes Hanninger,[87] T. Nunnemann,[99] E. Nurse,[77] F. Nuti,[87] B. J. O'Brien,[46] F. O'grady,[7] D. C. O'Neil,[143] V. O'Shea,[53] F. G. Oakham,[29,e] H. Oberlack,[100] T. Obermann,[21] J. Ocariz,[79] A. Ochi,[66] M. I. Ochoa,[77] S. Oda,[69] S. Odaka,[65] H. Ogren,[60] A. Oh,[83] S. H. Oh,[45] C. C. Ohm,[15] H. Ohman,[167] W. Okamura,[117] H. Okawa,[25] Y. Okumura,[31] T. Okuyama,[156] A. Olariu,[26a] A. G. Olchevski,[64] S. A. Olivares Pino,[46] D. Oliveira Damazio,[25] E. Oliver Garcia,[168] A. Olszewski,[39] J. Olszowska,[39] A. Onofre,[125a,125e] P. U. E. Onyisi,[31,cc] C. J. Oram,[160a] M. J. Oreglia,[31] Y. Oren,[154] D. Orestano,[135a,135b] N. Orlando,[72a,72b] C. Oropeza Barrera,[53] R. S. Orr,[159] B. Osculati,[50a,50b] R. Ospanov,[121] G. Otero y Garzon,[27] H. Otono,[69] M. Ouchrif,[136d] E. A. Ouellette,[170] F. Ould-Saada,[118] A. Ouraou,[137] K. P. Oussoren,[106] Q. Ouyang,[33a] A. Ovcharova,[15] M. Owen,[83] V. E. Ozcan,[19a] N. Ozturk,[8] K. Pachal,[119] A. Pacheco Pages,[12] C. Padilla Aranda,[12] M. Pagáčová,[48] S. Pagan Griso,[15] E. Paganis,[140] C. Pahl,[100] F. Paige,[25] P. Pais,[85] K. Pajchel,[118] G. Palacino,[160b] S. Palestini,[30] M. Palka,[38b] D. Pallin,[34] A. Palma,[125a,125b] J. D. Palmer,[18] Y. B. Pan,[174] E. Panagiotopoulou,[10] J. G. Panduro Vazquez,[76] P. Pani,[106] N. Panikashvili,[88] S. Panitkin,[25] D. Pantea,[26a] L. Paolozzi,[134a,134b] Th. D. Papadopoulou,[10] K. Papageorgiou,[155,m] A. Paramonov,[6] D. Paredes Hernandez,[34] M. A. Parker,[28] F. Parodi,[50a,50b] J. A. Parsons,[35] U. Parzefall,[48] E. Pasqualucci,[133a] S. Passaggio,[50a] A. Passeri,[135a] F. Pastore,[135a,135b,a] Fr. Pastore,[76] G. Pásztor,[29] S. Pataraia,[176] N. D. Patel,[151] J. R. Pater,[83] S. Patricelli,[103a,103b]

T. Pauly,[30] J. Pearce,[170] M. Pedersen,[118] S. Pedraza Lopez,[168] R. Pedro,[125a,125b] S. V. Peleganchuk,[108] D. Pelikan,[167] H. Peng,[33b] B. Penning,[31] J. Penwell,[60] D. V. Perepelitsa,[25] E. Perez Codina,[160a] M. T. Pérez García-Estañ,[168] V. Perez Reale,[35] L. Perini,[90a,90b] H. Pernegger,[30] R. Perrino,[72a] R. Peschke,[42] V. D. Peshekhonov,[64] K. Peters,[30] R. F. Y. Peters,[83] B. A. Petersen,[30] T. C. Petersen,[36] E. Petit,[42] A. Petridis,[147a,147b] C. Petridou,[155] E. Petrolo,[133a] F. Petrucci,[135a,135b] N. E. Pettersson,[158] R. Pezoa,[32b] P. W. Phillips,[130] G. Piacquadio,[144] E. Pianori,[171] A. Picazio,[49] E. Piccaro,[75] M. Piccinini,[20a,20b] R. Piegaia,[27] D. T. Pignotti,[110] J. E. Pilcher,[31] A. D. Pilkington,[77] J. Pina,[125a,125b,125d] M. Pinamonti,[165a,165c,dd] A. Pinder,[119] J. L. Pinfold,[3] A. Pingel,[36] B. Pinto,[125a] S. Pires,[79] M. Pitt,[173] C. Pizio,[90a,90b] L. Plazak,[145a] M.-A. Pleier,[25] V. Pleskot,[128] E. Plotnikova,[64] P. Plucinski,[147a,147b] S. Poddar,[58a] F. Podlyski,[34] R. Poettgen,[82] L. Poggioli,[116] D. Pohl,[21] M. Pohl,[49] G. Polesello,[120a] A. Policicchio,[37a,37b] R. Polifka,[159] A. Polini,[20a] C. S. Pollard,[45] V. Polychronakos,[25] K. Pommès,[30] L. Pontecorvo,[133a] B. G. Pope,[89] G. A. Popeneciu,[26b] D. S. Popovic,[13a] A. Poppleton,[30] X. Portell Bueso,[12] S. Pospisil,[127] K. Potamianos,[15] I. N. Potrap,[64] C. J. Potter,[150] C. T. Potter,[115] G. Poulard,[30] J. Poveda,[60] V. Pozdnyakov,[64] P. Pralavorio,[84] A. Pranko,[15] S. Prasad,[30] R. Pravahan,[8] S. Prell,[63] D. Price,[83] J. Price,[73] L. E. Price,[6] D. Prieur,[124] M. Primavera,[72a] M. Proissl,[46] K. Prokofiev,[47] F. Prokoshin,[32b] E. Protopapadaki,[137] S. Protopopescu,[25] J. Proudfoot,[6] M. Przybycien,[38a] H. Przysiezniak,[5] E. Ptacek,[115] D. Puddu,[135a,135b] E. Pueschel,[85] D. Puldon,[149] M. Purohit,[25,ee] P. Puzo,[116] J. Qian,[88] G. Qin,[53] Y. Qin,[83] A. Quadt,[54] D. R. Quarrie,[15] W. B. Quayle,[165a,165b] M. Queitsch-Maitland,[83] D. Quilty,[53] A. Qureshi,[160b] V. Radeka,[25] V. Radescu,[42] S. K. Radhakrishnan,[149] P. Radloff,[115] P. Rados,[87] F. Ragusa,[90a,90b] G. Rahal,[179] S. Rajagopalan,[25] M. Rammensee,[30] A. S. Randle-Conde,[40] C. Rangel-Smith,[167] K. Rao,[164] F. Rauscher,[99] T. C. Rave,[48] T. Ravenscroft,[53] M. Raymond,[30] A. L. Read,[118] N. P. Readioff,[73] D. M. Rebuzzi,[120a,120b] A. Redelbach,[175] G. Redlinger,[25] R. Reece,[138] K. Reeves,[41] L. Rehnisch,[16] H. Reisin,[27] M. Relich,[164] C. Rembser,[30] H. Ren,[33a] Z. L. Ren,[152] A. Renaud,[116] M. Rescigno,[133a] S. Resconi,[90a] O. L. Rezanova,[108,t] P. Reznicek,[128] R. Rezvani,[94] R. Richter,[100] M. Ridel,[79] P. Rieck,[16] J. Rieger,[54] M. Rijssenbeek,[149] A. Rimoldi,[120a,120b] M. Rimoldi,[90a,90b] L. Rinaldi,[20a] E. Ritsch,[61] I. Riu,[12] F. Rizatdinova,[113] E. Rizvi,[75] S. H. Robertson,[86,j] A. Robichaud-Veronneau,[86] D. Robinson,[28] J. E. M. Robinson,[83] A. Robson,[53] C. Roda,[123a,123b] L. Rodrigues,[30] S. Roe,[30] O. Røhne,[118] S. Rolli,[162] A. Romaniouk,[97] M. Romano,[20a,20b] E. Romero Adam,[168] N. Rompotis,[139] M. Ronzani,[48] L. Roos,[79] E. Ros,[168] S. Rosati,[133a] K. Rosbach,[49] M. Rose,[76] P. Rose,[138] P. L. Rosendahl,[14] O. Rosenthal,[142] V. Rossetti,[147a,147b] E. Rossi,[103a,103b] L. P. Rossi,[50a] R. Rosten,[139] M. Rotaru,[26a] I. Roth,[173] J. Rothberg,[139] D. Rousseau,[116] C. R. Royon,[137] A. Rozanov,[84] Y. Rozen,[153] X. Ruan,[146c] F. Rubbo,[12] I. Rubinskiy,[42] V. I. Rud,[98] C. Rudolph,[44] M. S. Rudolph,[159] F. Rühr,[48] A. Ruiz-Martinez,[30] Z. Rurikova,[48] N. A. Rusakovich,[64] A. Ruschke,[99] J. P. Rutherfoord,[7] N. Ruthmann,[48] Y. F. Ryabov,[122] M. Rybar,[128] G. Rybkin,[116] N. C. Ryder,[119] A. F. Saavedra,[151] S. Sacerdoti,[27] A. Saddique,[3] I. Sadeh,[154] H. F-W. Sadrozinski,[138] R. Sadykov,[64] F. Safai Tehrani,[133a] H. Sakamoto,[156] Y. Sakurai,[172] G. Salamanna,[135a,135b] A. Salamon,[134a] M. Saleem,[112] D. Salek,[106] P. H. Sales De Bruin,[139] D. Salihagic,[100] A. Salnikov,[144] J. Salt,[168] D. Salvatore,[37a,37b] F. Salvatore,[150] A. Salvucci,[105] A. Salzburger,[30] D. Sampsonidis,[155] A. Sanchez,[103a,103b] J. Sánchez,[168] V. Sanchez Martinez,[168] H. Sandaker,[14] R. L. Sandbach,[75] H. G. Sander,[82] M. P. Sanders,[99] M. Sandhoff,[176] T. Sandoval,[28] C. Sandoval,[163] R. Sandstroem,[100] D. P. C. Sankey,[130] A. Sansoni,[47] C. Santoni,[34] R. Santonico,[134a,134b] H. Santos,[125a] I. Santoyo Castillo,[150] K. Sapp,[124] A. Sapronov,[64] J. G. Saraiva,[125a,125d] B. Sarrazin,[21] G. Sartisohn,[176] O. Sasaki,[65] Y. Sasaki,[156] G. Sauvage,[5,a] E. Sauvan,[5] P. Savard,[159,e] D. O. Savu,[30] C. Sawyer,[119] L. Sawyer,[78,n] D. H. Saxon,[53] J. Saxon,[121] C. Sbarra,[20a] A. Sbrizzi,[3] T. Scanlon,[77] D. A. Scannicchio,[164] M. Scarcella,[151] V. Scarfone,[37a,37b] J. Schaarschmidt,[173] P. Schacht,[100] D. Schaefer,[30] R. Schaefer,[42] S. Schaepe,[21] S. Schaetzel,[58b] U. Schäfer,[82] A. C. Schaffer,[116] D. Schaile,[99] R. D. Schamberger,[149] V. Scharf,[58a] V. A. Schegelsky,[122] D. Scheirich,[128] M. Schernau,[164] M. I. Scherzer,[35] C. Schiavi,[50a,50b] J. Schieck,[99] C. Schillo,[48] M. Schioppa,[37a,37b] S. Schlenker,[30] E. Schmidt,[48] K. Schmieden,[30] C. Schmitt,[82] C. Schmitt,[99] S. Schmitt,[58b] B. Schneider,[17] Y. J. Schnellbach,[73] U. Schnoor,[44] L. Schoeffel,[137] A. Schoening,[58b] B. D. Schoenrock,[89] A. L. S. Schorlemmer,[54] M. Schott,[82] D. Schouten,[160a] J. Schovancova,[25] S. Schramm,[159] M. Schreyer,[175] C. Schroeder,[82] N. Schuh,[82] M. J. Schultens,[21] H.-C. Schultz-Coulon,[58a] H. Schulz,[16] M. Schumacher,[48] B. A. Schumm,[138] Ph. Schune,[137] C. Schwanenberger,[83] A. Schwartzman,[144] Ph. Schwegler,[100] Ph. Schwemling,[137] R. Schwienhorst,[89] J. Schwindling,[137] T. Schwindt,[21] M. Schwoerer,[5] F. G. Sciacca,[17] E. Scifo,[116] G. Sciolla,[23] W. G. Scott,[130] F. Scuri,[123a,123b] F. Scutti,[21] J. Searcy,[88] G. Sedov,[42] E. Sedykh,[122] S. C. Seidel,[104] A. Seiden,[138] F. Seifert,[127] J. M. Seixas,[24a] G. Sekhniaidze,[103a] S. J. Sekula,[40] K. E. Selbach,[46] D. M. Seliverstov,[122,a] G. Sellers,[73] N. Semprini-Cesari,[20a,20b] C. Serfon,[30] L. Serin,[116] L. Serkin,[54] T. Serre,[84] R. Seuster,[160a] H. Severini,[112] T. Sfiligoj,[74] F. Sforza,[100] A. Sfyrla,[30] E. Shabalina,[54] M. Shamim,[115] L. Y. Shan,[33a] R. Shang,[166] J. T. Shank,[22] M. Shapiro,[15] P. B. Shatalov,[96] K. Shaw,[165a,165b] C. Y. Shehu,[150] P. Sherwood,[77]

L. Shi,[152,ff] S. Shimizu,[66] C. O. Shimmin,[164] M. Shimojima,[101] M. Shiyakova,[64] A. Shmeleva,[95] M. J. Shochet,[31] D. Short,[119] S. Shrestha,[63] E. Shulga,[97] M. A. Shupe,[7] S. Shushkevich,[42] P. Sicho,[126] O. Sidiropoulou,[155] D. Sidorov,[113] A. Sidoti,[133a] F. Siegert,[44] Dj. Sijacki,[13a] J. Silva,[125a,125d] Y. Silver,[154] D. Silverstein,[144] S. B. Silverstein,[147a] V. Simak,[127] O. Simard,[5] Lj. Simic,[13a] S. Simion,[116] E. Simioni,[82] B. Simmons,[77] R. Simoniello,[90a,90b] M. Simonyan,[36] P. Sinervo,[159] N. B. Sinev,[115] V. Sipica,[142] G. Siragusa,[175] A. Sircar,[78] A. N. Sisakyan,[64,a] S. Yu. Sivoklokov,[98] J. Sjölin,[147a,147b] T. B. Sjursen,[14] H. P. Skottowe,[57] K. Yu. Skovpen,[108] P. Skubic,[112] M. Slater,[18] T. Slavicek,[127] K. Sliwa,[162] V. Smakhtin,[173] B. H. Smart,[46] L. Smestad,[14] S. Yu. Smirnov,[97] Y. Smirnov,[97] L. N. Smirnova,[98,gg] O. Smirnova,[80] K. M. Smith,[53] M. Smizanska,[71] K. Smolek,[127] A. A. Snesarev,[95] G. Snidero,[75] S. Snyder,[25] R. Sobie,[170,j] F. Socher,[44] A. Soffer,[154] D. A. Soh,[152,ff] C. A. Solans,[30] M. Solar,[127] J. Solc,[127] E. Yu. Soldatov,[97] U. Soldevila,[168] A. A. Solodkov,[129] A. Soloshenko,[64] O. V. Solovyanov,[129] V. Solovyev,[122] P. Sommer,[48] H. Y. Song,[33b] N. Soni,[1] A. Sood,[15] A. Sopczak,[127] B. Sopko,[127] V. Sopko,[127] V. Sorin,[12] M. Sosebee,[8] R. Soualah,[165a,165c] P. Soueid,[94] A. M. Soukharev,[108] D. South,[42] S. Spagnolo,[72a,72b] F. Spanò,[76] W. R. Spearman,[57] F. Spettel,[100] R. Spighi,[20a] G. Spigo,[30] M. Spousta,[128] T. Spreitzer,[159] B. Spurlock,[8] R. D. St. Denis,[53,a] S. Staerz,[44] J. Stahlman,[121] R. Stamen,[58a] E. Stanecka,[39] R. W. Stanek,[6] C. Stanescu,[135a] M. Stanescu-Bellu,[42] M. M. Stanitzki,[42] S. Stapnes,[118] E. A. Starchenko,[129] J. Stark,[55] P. Staroba,[126] P. Starovoitov,[42] R. Staszewski,[39] P. Stavina,[145a,a] P. Steinberg,[25] B. Stelzer,[143] H. J. Stelzer,[30] O. Stelzer-Chilton,[160a] H. Stenzel,[52] S. Stern,[100] G. A. Stewart,[53] J. A. Stillings,[21] M. C. Stockton,[86] M. Stoebe,[86] G. Stoicea,[26a] P. Stolte,[54] S. Stonjek,[100] A. R. Stradling,[8] A. Straessner,[44] M. E. Stramaglia,[17] J. Strandberg,[148] S. Strandberg,[147a,147b] A. Strandlie,[118] E. Strauss,[144] M. Strauss,[112] P. Strizenec,[145b] R. Ströhmer,[175] D. M. Strom,[115] R. Stroynowski,[40] S. A. Stucci,[17] B. Stugu,[14] N. A. Styles,[42] D. Su,[144] J. Su,[124] R. Subramaniam,[78] A. Succurro,[12] Y. Sugaya,[117] C. Suhr,[107] M. Suk,[127] V. V. Sulin,[95] S. Sultansoy,[4c] T. Sumida,[67] S. Sun,[57] X. Sun,[33a] J. E. Sundermann,[48] K. Suruliz,[140] G. Susinno,[37a,37b] M. R. Sutton,[150] Y. Suzuki,[65] M. Svatos,[126] S. Swedish,[169] M. Swiatlowski,[144] I. Sykora,[145a] T. Sykora,[128] D. Ta,[89] C. Taccini,[135a,135b] K. Tackmann,[42] J. Taenzer,[159] A. Taffard,[164] R. Tafirout,[160a] N. Taiblum,[154] H. Takai,[25] R. Takashima,[68] H. Takeda,[66] T. Takeshita,[141] Y. Takubo,[65] M. Talby,[84] A. A. Talyshev,[108,t] J. Y. C. Tam,[175] K. G. Tan,[87] J. Tanaka,[156] R. Tanaka,[116] S. Tanaka,[132] S. Tanaka,[65] A. J. Tanasijczuk,[143] B. B. Tannenwald,[110] N. Tannoury,[21] S. Tapprogge,[82] S. Tarem,[153] F. Tarrade,[29] G. F. Tartarelli,[90a] P. Tas,[128] M. Tasevsky,[126] T. Tashiro,[67] E. Tassi,[37a,37b] A. Tavares Delgado,[125a,125b] Y. Tayalati,[136d] F. E. Taylor,[93] G. N. Taylor,[87] W. Taylor,[160b] F. A. Teischinger,[30] M. Teixeira Dias Castanheira,[75] P. Teixeira-Dias,[76] K. K. Temming,[48] H. Ten Kate,[30] P. K. Teng,[152] J. J. Teoh,[117] S. Terada,[65] K. Terashi,[156] J. Terron,[81] S. Terzo,[100] M. Testa,[47] R. J. Teuscher,[159,j] J. Therhaag,[21] T. Theveneaux-Pelzer,[34] J. P. Thomas,[18] J. Thomas-Wilsker,[76] E. N. Thompson,[35] P. D. Thompson,[18] P. D. Thompson,[159] A. S. Thompson,[53] L. A. Thomsen,[36] E. Thomson,[121] M. Thomson,[28] W. M. Thong,[87] R. P. Thun,[88,a] F. Tian,[35] M. J. Tibbetts,[15] V. O. Tikhomirov,[95,hh] Yu. A. Tikhonov,[108,t] S. Timoshenko,[97] E. Tiouchichine,[84] P. Tipton,[177] S. Tisserant,[84] T. Todorov,[5] S. Todorova-Nova,[128] B. Toggerson,[7] J. Tojo,[69] S. Tokár,[145a] K. Tokushuku,[65] K. Tollefson,[89] L. Tomlinson,[83] M. Tomoto,[102] L. Tompkins,[31] K. Toms,[104] N. D. Topilin,[64] E. Torrence,[115] H. Torres,[143] E. Torró Pastor,[168] J. Toth,[84,ii] F. Touchard,[84] D. R. Tovey,[140] H. L. Tran,[116] T. Trefzger,[175] L. Tremblet,[30] A. Tricoli,[30] I. M. Trigger,[160a] S. Trincaz-Duvoid,[79] M. F. Tripiana,[12] W. Trischuk,[159] B. Trocmé,[55] C. Troncon,[90a] M. Trottier-McDonald,[143] M. Trovatelli,[135a,135b] P. True,[89] M. Trzebinski,[39] A. Trzupek,[39] C. Tsarouchas,[30] J. C-L. Tseng,[119] P. V. Tsiareshka,[91] D. Tsionou,[137] G. Tsipolitis,[10] N. Tsirintanis,[9] S. Tsiskaridze,[12] V. Tsiskaridze,[48] E. G. Tskhadadze,[51a] I. I. Tsukerman,[96] V. Tsulaia,[15] S. Tsuno,[65] D. Tsybychev,[149] A. Tudorache,[26a] V. Tudorache,[26a] A. N. Tuna,[121] S. A. Tupputi,[20a,20b] S. Turchikhin,[98,gg] D. Turecek,[127] I. Turk Cakir,[4d] R. Turra,[90a,90b] P. M. Tuts,[35] A. Tykhonov,[49] M. Tylmad,[147a,147b] M. Tyndel,[130] K. Uchida,[21] I. Ueda,[156] R. Ueno,[29] M. Ughetto,[84] M. Ugland,[14] M. Uhlenbrock,[21] F. Ukegawa,[161] G. Unal,[30] A. Undrus,[25] G. Unel,[164] F. C. Ungaro,[48] Y. Unno,[65] D. Urbaniec,[35] P. Urquijo,[87] G. Usai,[8] A. Usanova,[61] L. Vacavant,[84] V. Vacek,[127] B. Vachon,[86] N. Valencic,[106] S. Valentinetti,[20a,20b] A. Valero,[168] L. Valery,[34] S. Valkar,[128] E. Valladolid Gallego,[168] S. Vallecorsa,[49] J. A. Valls Ferrer,[168] W. Van Den Wollenberg,[106] P. C. Van Der Deijl,[106] R. van der Geer,[106] H. van der Graaf,[106] R. Van Der Leeuw,[106] D. van der Ster,[30] N. van Eldik,[30] P. van Gemmeren,[6] J. Van Nieuwkoop,[143] I. van Vulpen,[106] M. C. van Woerden,[30] M. Vanadia,[133a,133b] W. Vandelli,[30] R. Vanguri,[121] A. Vaniachine,[6] P. Vankov,[42] F. Vannucci,[79] G. Vardanyan,[178] R. Vari,[133a] E. W. Varnes,[7] T. Varol,[85] D. Varouchas,[79] A. Vartapetian,[8] K. E. Varvell,[151] F. Vazeille,[34] T. Vazquez Schroeder,[54] J. Veatch,[7] F. Veloso,[125a,125c] S. Veneziano,[133a] A. Ventura,[72a,72b] D. Ventura,[85] M. Venturi,[170] N. Venturi,[159] A. Venturini,[23] V. Vercesi,[120a] M. Verducci,[133a,133b] W. Verkerke,[106] J. C. Vermeulen,[106] A. Vest,[44] M. C. Vetterli,[143,e] O. Viazlo,[80] I. Vichou,[166] T. Vickey,[146c,jj] O. E. Vickey Boeriu,[146c] G. H. A. Viehhauser,[119] S. Viel,[169] R. Vigne,[30] M. Villa,[20a,20b] M. Villaplana Perez,[90a,90b]

E. Vilucchi,[47] M. G. Vincter,[29] V. B. Vinogradov,[64] J. Virzi,[15] I. Vivarelli,[150] F. Vives Vaque,[3] S. Vlachos,[10] D. Vladoiu,[99] M. Vlasak,[127] A. Vogel,[21] M. Vogel,[32a] P. Vokac,[127] G. Volpi,[123a,123b] M. Volpi,[87] H. von der Schmitt,[100] H. von Radziewski,[48] E. von Toerne,[21] V. Vorobel,[128] K. Vorobev,[97] M. Vos,[168] R. Voss,[30] J. H. Vossebeld,[73] N. Vranjes,[137] M. Vranjes Milosavljevic,[106] V. Vrba,[126] M. Vreeswijk,[106] T. Vu Anh,[48] R. Vuillermet,[30] I. Vukotic,[31] Z. Vykydal,[127] P. Wagner,[21] W. Wagner,[176] H. Wahlberg,[70] S. Wahrmund,[44] J. Wakabayashi,[102] J. Walder,[71] R. Walker,[99] W. Walkowiak,[142] R. Wall,[177] P. Waller,[73] B. Walsh,[177] C. Wang,[152,kk] C. Wang,[45] F. Wang,[174] H. Wang,[15] H. Wang,[40] J. Wang,[42] J. Wang,[33a] K. Wang,[86] R. Wang,[104] S. M. Wang,[152] T. Wang,[21] X. Wang,[177] C. Wanotayaroj,[115] A. Warburton,[86] C. P. Ward,[28] D. R. Wardrope,[77] M. Warsinsky,[48] A. Washbrook,[46] C. Wasicki,[42] P. M. Watkins,[18] A. T. Watson,[18] I. J. Watson,[151] M. F. Watson,[18] G. Watts,[139] S. Watts,[83] B. M. Waugh,[77] S. Webb,[83] M. S. Weber,[17] S. W. Weber,[175] J. S. Webster,[31] A. R. Weidberg,[119] P. Weigell,[100] B. Weinert,[60] J. Weingarten,[54] C. Weiser,[48] H. Weits,[106] P. S. Wells,[30] T. Wenaus,[25] D. Wendland,[16] Z. Weng,[152,ff] T. Wengler,[30] S. Wenig,[30] N. Wermes,[21] M. Werner,[48] P. Werner,[30] M. Wessels,[58a] J. Wetter,[162] K. Whalen,[29] A. White,[8] M. J. White,[1] R. White,[32b] S. White,[123a,123b] D. Whiteson,[164] D. Wicke,[176] F. J. Wickens,[130] W. Wiedenmann,[174] M. Wielers,[130] P. Wienemann,[21] C. Wiglesworth,[36] L. A. M. Wiik-Fuchs,[21] P. A. Wijeratne,[77] A. Wildauer,[100] M. A. Wildt,[42,ll] H. G. Wilkens,[30] J. Z. Will,[99] H. H. Williams,[121] S. Williams,[28] C. Willis,[89] S. Willocq,[85] A. Wilson,[88] J. A. Wilson,[18] I. Wingerter-Seez,[5] F. Winklmeier,[115] B. T. Winter,[21] M. Wittgen,[144] T. Wittig,[43] J. Wittkowski,[99] S. J. Wollstadt,[82] M. W. Wolter,[39] H. Wolters,[125a,125c] B. K. Wosiek,[39] J. Wotschack,[30] M. J. Woudstra,[83] K. W. Wozniak,[39] M. Wright,[53] M. Wu,[55] S. L. Wu,[174] X. Wu,[49] Y. Wu,[88] E. Wulf,[35] T. R. Wyatt,[83] B. M. Wynne,[46] S. Xella,[36] M. Xiao,[137] D. Xu,[33a] L. Xu,[33b,mm] B. Yabsley,[151] S. Yacoob,[146b,nn] R. Yakabe,[66] M. Yamada,[65] H. Yamaguchi,[156] Y. Yamaguchi,[117] A. Yamamoto,[65] K. Yamamoto,[63] S. Yamamoto,[156] T. Yamamura,[156] T. Yamanaka,[156] K. Yamauchi,[102] Y. Yamazaki,[66] Z. Yan,[22] H. Yang,[33e] H. Yang,[174] U. K. Yang,[83] Y. Yang,[110] S. Yanush,[92] L. Yao,[33a] W-M. Yao,[15] Y. Yasu,[65] E. Yatsenko,[42] K. H. Yau Wong,[21] J. Ye,[40] S. Ye,[25] A. L. Yen,[57] E. Yildirim,[42] M. Yilmaz,[4b] R. Yoosoofmiya,[124] K. Yorita,[172] R. Yoshida,[6] K. Yoshihara,[156] C. Young,[144] C. J. S. Young,[30] S. Youssef,[22] D. R. Yu,[15] J. Yu,[8] J. M. Yu,[88] J. Yu,[113] L. Yuan,[66] A. Yurkewicz,[107] I. Yusuff,[28,oo] B. Zabinski,[39] R. Zaidan,[62] A. M. Zaitsev,[129,aa] A. Zaman,[149] S. Zambito,[23] L. Zanello,[133a,133b] D. Zanzi,[100] C. Zeitnitz,[176] M. Zeman,[127] A. Zemla,[38a] K. Zengel,[23] O. Zenin,[129] T. Ženiš,[145a] D. Zerwas,[116] G. Zevi della Porta,[57] D. Zhang,[88] F. Zhang,[174] H. Zhang,[89] J. Zhang,[6] L. Zhang,[152] X. Zhang,[33d] Z. Zhang,[116] Z. Zhao,[33b] A. Zhemchugov,[64] J. Zhong,[119] B. Zhou,[88] L. Zhou,[35] N. Zhou,[164] C. G. Zhu,[33d] H. Zhu,[33a] J. Zhu,[88] Y. Zhu,[33b] X. Zhuang,[33a] K. Zhukov,[95] A. Zibell,[175] D. Zieminska,[60] N. I. Zimine,[64] C. Zimmermann,[82] R. Zimmermann,[21] S. Zimmermann,[21] S. Zimmermann,[48] Z. Zinonos,[54] M. Ziolkowski,[142] G. Zobernig,[174] A. Zoccoli,[20a,20b] M. zur Nedden,[16] G. Zurzolo,[103a,103b] V. Zutshi[107] and L. Zwalinski[30]

(ATLAS Collaboration)

[1]*Department of Physics, University of Adelaide, Adelaide, Australia*
[2]*Physics Department, SUNY Albany, Albany, New York, USA*
[3]*Department of Physics, University of Alberta, Edmonton AB, Canada*
[4a]*Department of Physics, Ankara University, Ankara, Turkey*
[4b]*Department of Physics, Gazi University, Ankara, Turkey*
[4c]*Division of Physics, TOBB University of Economics and Technology, Ankara, Turkey*
[4d]*Turkish Atomic Energy Authority, Ankara, Turkey*
[5]*LAPP, CNRS/IN2P3 and Université de Savoie, Annecy-le-Vieux, France*
[6]*High Energy Physics Division, Argonne National Laboratory, Argonne, Illinois, USA*
[7]*Department of Physics, University of Arizona, Tucson, Arizona, USA*
[8]*Department of Physics, The University of Texas at Arlington, Arlington, Texas, USA*
[9]*Physics Department, University of Athens, Athens, Greece*
[10]*Physics Department, National Technical University of Athens, Zografou, Greece*
[11]*Institute of Physics, Azerbaijan Academy of Sciences, Baku, Azerbaijan*
[12]*Institut de Física d'Altes Energies and Departament de Física de la Universitat Autònoma de Barcelona, Barcelona, Spain*
[13a]*Institute of Physics, University of Belgrade, Belgrade, Serbia*
[13b]*Vinca Institute of Nuclear Sciences, University of Belgrade, Belgrade, Serbia*
[14]*Department for Physics and Technology, University of Bergen, Bergen, Norway*
[15]*Physics Division, Lawrence Berkeley National Laboratory and University of California, Berkeley, California, USA*

[16]Department of Physics, Humboldt University, Berlin, Germany
[17]Albert Einstein Center for Fundamental Physics and Laboratory for High Energy Physics, University of Bern, Bern, Switzerland
[18]School of Physics and Astronomy, University of Birmingham, Birmingham, United Kingdom
[19a]Department of Physics, Bogazici University, Istanbul, Turkey
[19b]Department of Physics, Dogus University, Istanbul, Turkey
[19c]Department of Physics Engineering, Gaziantep University, Gaziantep, Turkey
[20a]INFN Sezione di Bologna, Bologna, Italy
[20b]Dipartimento di Fisica e Astronomia, Università di Bologna, Bologna, Italy
[21]Physikalisches Institut, University of Bonn, Bonn, Germany
[22]Department of Physics, Boston University, Boston, Massachusetts, USA
[23]Department of Physics, Brandeis University, Waltham, Massachusetts, USA
[24a]Universidade Federal do Rio De Janeiro COPPE/EE/IF, Rio de Janeiro, Brazil
[24b]Federal University of Juiz de Fora (UFJF), Juiz de Fora, Brazil
[24c]Federal University of Sao Joao del Rei (UFSJ), Sao Joao del Rei, Brazil
[24d]Instituto de Fisica, Universidade de Sao Paulo, Sao Paulo, Brazil
[25]Physics Department, Brookhaven National Laboratory, Upton, New York, USA
[26a]National Institute of Physics and Nuclear Engineering, Bucharest, Romania
[26b]National Institute for Research and Development of Isotopic and Molecular Technologies, Physics Department, Cluj Napoca, Romania
[26c]University Politehnica Bucharest, Bucharest, Romania
[26d]West University in Timisoara, Timisoara, Romania
[27]Departamento de Física, Universidad de Buenos Aires, Buenos Aires, Argentina
[28]Cavendish Laboratory, University of Cambridge, Cambridge, United Kingdom
[29]Department of Physics, Carleton University, Ottawa ON, Canada
[30]CERN, Geneva, Switzerland
[31]Enrico Fermi Institute, University of Chicago, Chicago, Illinois, USA
[32a]Departamento de Física, Pontificia Universidad Católica de Chile, Santiago, Chile
[32b]Departamento de Física, Universidad Técnica Federico Santa María, Valparaíso, Chile
[33a]Institute of High Energy Physics, Chinese Academy of Sciences, Beijing, China
[33b]Department of Modern Physics, University of Science and Technology of China, Anhui, China
[33c]Department of Physics, Nanjing University, Jiangsu, China
[33d]School of Physics, Shandong University, Shandong, China
[33e]Physics Department, Shanghai Jiao Tong University, Shanghai, China
[34]Laboratoire de Physique Corpusculaire, Clermont Université and Université Blaise Pascal and CNRS/IN2P3, Clermont-Ferrand, France
[35]Nevis Laboratory, Columbia University, Irvington, New York, USA
[36]Niels Bohr Institute, University of Copenhagen, Kobenhavn, Denmark
[37a]INFN Gruppo Collegato di Cosenza, Laboratori Nazionali di Frascati, Italy
[37b]Dipartimento di Fisica, Università della Calabria, Rende, Italy
[38a]AGH University of Science and Technology, Faculty of Physics and Applied Computer Science, Krakow, Poland
[38b]Marian Smoluchowski Institute of Physics, Jagiellonian University, Krakow, Poland
[39]The Henryk Niewodniczanski Institute of Nuclear Physics, Polish Academy of Sciences, Krakow, Poland
[40]Physics Department, Southern Methodist University, Dallas, Texas, USA
[41]Physics Department, University of Texas at Dallas, Richardson, Texas, USA
[42]DESY, Hamburg and Zeuthen, Germany
[43]Institut für Experimentelle Physik IV, Technische Universität Dortmund, Dortmund, Germany
[44]Institut für Kern- und Teilchenphysik, Technische Universität Dresden, Dresden, Germany
[45]Department of Physics, Duke University, Durham, North Carolina, USA
[46]SUPA - School of Physics and Astronomy, University of Edinburgh, Edinburgh, United Kingdom
[47]INFN Laboratori Nazionali di Frascati, Frascati, Italy
[48]Fakultät für Mathematik und Physik, Albert-Ludwigs-Universität, Freiburg, Germany
[49]Section de Physique, Université de Genève, Geneva, Switzerland
[50a]INFN Sezione di Genova, Genova, Italy
[50b]Dipartimento di Fisica, Università di Genova, Genova, Italy
[51a]E. Andronikashvili Institute of Physics, Iv. Javakhishvili Tbilisi State University, Tbilisi, Georgia
[51b]High Energy Physics Institute, Tbilisi State University, Tbilisi, Georgia
[52]II Physikalisches Institut, Justus-Liebig-Universität Giessen, Giessen, Germany
[53]SUPA - School of Physics and Astronomy, University of Glasgow, Glasgow, United Kingdom

[54]*II Physikalisches Institut, Georg-August-Universität, Göttingen, Germany*
[55]*Laboratoire de Physique Subatomique et de Cosmologie, Université Grenoble-Alpes, CNRS/IN2P3, Grenoble, France*
[56]*Department of Physics, Hampton University, Hampton, Virginia, USA*
[57]*Laboratory for Particle Physics and Cosmology, Harvard University, Cambridge, Massachusetts, USA*
[58a]*Kirchhoff-Institut für Physik, Ruprecht-Karls-Universität Heidelberg, Heidelberg, Germany*
[58b]*Physikalisches Institut, Ruprecht-Karls-Universität Heidelberg, Heidelberg, Germany*
[58c]*ZITI Institut für technische Informatik, Ruprecht-Karls-Universität Heidelberg, Mannheim, Germany*
[59]*Faculty of Applied Information Science, Hiroshima Institute of Technology, Hiroshima, Japan*
[60]*Department of Physics, Indiana University, Bloomington, Indiana, USA*
[61]*Institut für Astro- und Teilchenphysik, Leopold-Franzens-Universität, Innsbruck, Austria*
[62]*University of Iowa, Iowa City, Iowa, USA*
[63]*Department of Physics and Astronomy, Iowa State University, Ames, Iowa, USA*
[64]*Joint Institute for Nuclear Research, JINR Dubna, Dubna, Russia*
[65]*KEK, High Energy Accelerator Research Organization, Tsukuba, Japan*
[66]*Graduate School of Science, Kobe University, Kobe, Japan*
[67]*Faculty of Science, Kyoto University, Kyoto, Japan*
[68]*Kyoto University of Education, Kyoto, Japan*
[69]*Department of Physics, Kyushu University, Fukuoka, Japan*
[70]*Instituto de Física La Plata, Universidad Nacional de La Plata and CONICET, La Plata, Argentina*
[71]*Physics Department, Lancaster University, Lancaster, United Kingdom*
[72a]*INFN Sezione di Lecce, Lecce, Italy*
[72b]*Dipartimento di Matematica e Fisica, Università del Salento, Lecce, Italy*
[73]*Oliver Lodge Laboratory, University of Liverpool, Liverpool, United Kingdom*
[74]*Department of Physics, Jožef Stefan Institute and University of Ljubljana, Ljubljana, Slovenia*
[75]*School of Physics and Astronomy, Queen Mary University of London, London, United Kingdom*
[76]*Department of Physics, Royal Holloway University of London, Surrey, United Kingdom*
[77]*Department of Physics and Astronomy, University College London, London, United Kingdom*
[78]*Louisiana Tech University, Ruston, Louisiana, USA*
[79]*Laboratoire de Physique Nucléaire et de Hautes Energies, UPMC and Université Paris-Diderot and CNRS/IN2P3, Paris, France*
[80]*Fysiska institutionen, Lunds universitet, Lund, Sweden*
[81]*Departamento de Fisica Teorica C-15, Universidad Autonoma de Madrid, Madrid, Spain*
[82]*Institut für Physik, Universität Mainz, Mainz, Germany*
[83]*School of Physics and Astronomy, University of Manchester, Manchester, United Kingdom*
[84]*CPPM, Aix-Marseille Université and CNRS/IN2P3, Marseille, France*
[85]*Department of Physics, University of Massachusetts, Amherst, Massachusetts, USA*
[86]*Department of Physics, McGill University, Montreal QC, Canada*
[87]*School of Physics, University of Melbourne, Victoria, Australia*
[88]*Department of Physics, The University of Michigan, Ann Arbor, Michigan, USA*
[89]*Department of Physics and Astronomy, Michigan State University, East Lansing, Michigan, USA*
[90a]*INFN Sezione di Milano, Milano, Italy*
[90b]*Dipartimento di Fisica, Università di Milano, Milano, Italy*
[91]*B. I. Stepanov Institute of Physics, National Academy of Sciences of Belarus, Minsk, Republic of Belarus*
[92]*National Scientific and Educational Centre for Particle and High Energy Physics, Minsk, Republic of Belarus*
[93]*Department of Physics, Massachusetts Institute of Technology, Cambridge, Massachusetts, USA*
[94]*Group of Particle Physics, University of Montreal, Montreal, Québec, Canada*
[95]*P. N. Lebedev Institute of Physics, Academy of Sciences, Moscow, Russia*
[96]*Institute for Theoretical and Experimental Physics (ITEP), Moscow, Russia*
[97]*Moscow Engineering and Physics Institute (MEPhI), Moscow, Russia*
[98]*D. V. Skobeltsyn Institute of Nuclear Physics, M. V. Lomonosov Moscow State University, Moscow, Russia*
[99]*Fakultät für Physik, Ludwig-Maximilians-Universität München, München, Germany*
[100]*Max-Planck-Institut für Physik (Werner-Heisenberg-Institut), München, Germany*
[101]*Nagasaki Institute of Applied Science, Nagasaki, Japan*
[102]*Graduate School of Science and Kobayashi-Maskawa Institute, Nagoya University, Nagoya, Japan*
[103a]*INFN Sezione di Napoli, Napoli, Italy*
[103b]*Dipartimento di Fisica, Università di Napoli, Napoli, Italy*
[104]*Department of Physics and Astronomy, University of New Mexico, Albuquerque, New Mexico, USA*

[105]Institute for Mathematics, Astrophysics and Particle Physics, Radboud University Nijmegen/Nikhef, Nijmegen, Netherlands
[106]Nikhef National Institute for Subatomic Physics and University of Amsterdam, Amsterdam, Netherlands
[107]Department of Physics, Northern Illinois University, DeKalb, Illinois, USA
[108]Budker Institute of Nuclear Physics, SB RAS, Novosibirsk, Russia
[109]Department of Physics, New York University, New York, New York, USA
[110]Ohio State University, Columbus, Ohio, USA
[111]Faculty of Science, Okayama University, Okayama, Japan
[112]Homer L. Dodge Department of Physics and Astronomy, University of Oklahoma, Norman, Oklahoma, USA
[113]Department of Physics, Oklahoma State University, Stillwater, Oklahoma, USA
[114]Palacký University, RCPTM, Olomouc, Czech Republic
[115]Center for High Energy Physics, University of Oregon, Eugene, Oregon, USA
[116]LAL, Université Paris-Sud and CNRS/IN2P3, Orsay, France
[117]Graduate School of Science, Osaka University, Osaka, Japan
[118]Department of Physics, University of Oslo, Oslo, Norway
[119]Department of Physics, Oxford University, Oxford, United Kingdom
[120a]INFN Sezione di Pavia, Pavia, Italy
[120b]Dipartimento di Fisica, Università di Pavia, Pavia, Italy
[121]Department of Physics, University of Pennsylvania, Philadelphia, Pennsylvania, USA
[122]Petersburg Nuclear Physics Institute, Gatchina, Russia
[123a]INFN Sezione di Pisa, Pisa, Italy
[123b]Dipartimento di Fisica E. Fermi, Università di Pisa, Pisa, Italy
[124]Department of Physics and Astronomy, University of Pittsburgh, Pittsburgh, Pennsylvania, USA
[125a]Laboratorio de Instrumentacao e Fisica Experimental de Particulas - LIP, Lisboa, Portugal
[125b]Faculdade de Ciências, Universidade de Lisboa, Lisboa, Portugal
[125c]Department of Physics, University of Coimbra, Coimbra, Portugal
[125d]Centro de Física Nuclear da Universidade de Lisboa, Lisboa, Portugal
[125e]Departamento de Fisica, Universidade do Minho, Braga, Portugal
[125f]Departamento de Fisica Teorica y del Cosmos and CAFPE, Universidad de Granada, Granada (Spain), Portugal
[125g]Dep Fisica and CEFITEC of Faculdade de Ciencias e Tecnologia, Universidade Nova de Lisboa, Caparica, Portugal
[126]Institute of Physics, Academy of Sciences of the Czech Republic, Praha, Czech Republic
[127]Czech Technical University in Prague, Praha, Czech Republic
[128]Faculty of Mathematics and Physics, Charles University in Prague, Praha, Czech Republic
[129]State Research Center Institute for High Energy Physics, Protvino, Russia
[130]Particle Physics Department, Rutherford Appleton Laboratory, Didcot, United Kingdom
[131]Physics Department, University of Regina, Regina, Saskatchewan, Canada
[132]Ritsumeikan University, Kusatsu, Shiga, Japan
[133a]INFN Sezione di Roma, Roma, Italy
[133b]Dipartimento di Fisica, Sapienza Università di Roma, Roma, Italy
[134a]INFN Sezione di Roma Tor Vergata, Roma, Italy
[134b]Dipartimento di Fisica, Università di Roma Tor Vergata, Roma, Italy
[135a]INFN Sezione di Roma Tre, Roma, Italy
[135b]Dipartimento di Matematica e Fisica, Università Roma Tre, Roma, Italy
[136a]Faculté des Sciences Ain Chock, Réseau Universitaire de Physique des Hautes Energies - Université Hassan II, Casablanca, Morocco
[136b]Centre National de l'Energie des Sciences Techniques Nucleaires, Rabat, Morocco
[136c]Faculté des Sciences Semlalia, Université Cadi Ayyad, LPHEA-Marrakech, Morocco
[136d]Faculté des Sciences, Université Mohamed Premier and LPTPM, Oujda, Morocco
[136e]Faculté des sciences, Université Mohammed V-Agdal, Rabat, Morocco
[137]DSM/IRFU (Institut de Recherches sur les Lois Fondamentales de l'Univers), CEA Saclay (Commissariat à l'Energie Atomique et aux Energies Alternatives), Gif-sur-Yvette, France
[138]Santa Cruz Institute for Particle Physics, University of California Santa Cruz, Santa Cruz, California, USA
[139]Department of Physics, University of Washington, Seattle, Washington, USA
[140]Department of Physics and Astronomy, University of Sheffield, Sheffield, United Kingdom
[141]Department of Physics, Shinshu University, Nagano, Japan
[142]Fachbereich Physik, Universität Siegen, Siegen, Germany

[143]*Department of Physics, Simon Fraser University, Burnaby, British Columbia, Canada*
[144]*SLAC National Accelerator Laboratory, Stanford, California, USA*
[145a]*Faculty of Mathematics, Physics & Informatics, Comenius University, Bratislava, Slovak Republic*
[145b]*Department of Subnuclear Physics, Institute of Experimental Physics of the Slovak Academy of Sciences, Kosice, Slovak Republic*
[146a]*Department of Physics, University of Cape Town, Cape Town, South Africa*
[146b]*Department of Physics, University of Johannesburg, Johannesburg, South Africa*
[146c]*School of Physics, University of the Witwatersrand, Johannesburg, South Africa*
[147a]*Department of Physics, Stockholm University, Stockholm, Sweden*
[147b]*The Oskar Klein Centre, Stockholm, Sweden*
[148]*Physics Department, Royal Institute of Technology, Stockholm, Sweden*
[149]*Departments of Physics & Astronomy and Chemistry, Stony Brook University, Stony Brook, New York, USA*
[150]*Department of Physics and Astronomy, University of Sussex, Brighton, United Kingdom*
[151]*School of Physics, University of Sydney, Sydney, Australia*
[152]*Institute of Physics, Academia Sinica, Taipei, Taiwan*
[153]*Department of Physics, Technion: Israel Institute of Technology, Haifa, Israel*
[154]*Raymond and Beverly Sackler School of Physics and Astronomy, Tel Aviv University, Tel Aviv, Israel*
[155]*Department of Physics, Aristotle University of Thessaloniki, Thessaloniki, Greece*
[156]*International Center for Elementary Particle Physics and Department of Physics, The University of Tokyo, Tokyo, Japan*
[157]*Graduate School of Science and Technology, Tokyo Metropolitan University, Tokyo, Japan*
[158]*Department of Physics, Tokyo Institute of Technology, Tokyo, Japan*
[159]*Department of Physics, University of Toronto, Toronto, Ontario, Canada*
[160a]*TRIUMF, Vancouver, British Columbia, Canada*
[160b]*Department of Physics and Astronomy, York University, Toronto, Ontario, Canada*
[161]*Faculty of Pure and Applied Sciences, University of Tsukuba, Tsukuba, Japan*
[162]*Department of Physics and Astronomy, Tufts University, Medford, Massachusetts, USA*
[163]*Centro de Investigaciones, Universidad Antonio Narino, Bogota, Colombia*
[164]*Department of Physics and Astronomy, University of California Irvine, Irvine, California, USA*
[165a]*INFN Gruppo Collegato di Udine, Sezione di Trieste, Udine, Italy*
[165b]*ICTP, Trieste, Italy*
[165c]*Dipartimento di Chimica, Fisica e Ambiente, Università di Udine, Udine, Italy*
[166]*Department of Physics, University of Illinois, Urbana, Illinois, USA*
[167]*Department of Physics and Astronomy, University of Uppsala, Uppsala, Sweden*
[168]*Instituto de Física Corpuscular (IFIC) and Departamento de Física Atómica, Molecular y Nuclear and Departamento de Ingeniería Electrónica and Instituto de Microelectrónica de Barcelona (IMB-CNM), University of Valencia and CSIC, Valencia, Spain*
[169]*Department of Physics, University of British Columbia, Vancouver, British Columbia, Canada*
[170]*Department of Physics and Astronomy, University of Victoria, Victoria, British Columbia, Canada*
[171]*Department of Physics, University of Warwick, Coventry, United Kingdom*
[172]*Waseda University, Tokyo, Japan*
[173]*Department of Particle Physics, The Weizmann Institute of Science, Rehovot, Israel*
[174]*Department of Physics, University of Wisconsin, Madison, Wisconsin, USA*
[175]*Fakultät für Physik und Astronomie, Julius-Maximilians-Universität, Würzburg, Germany*
[176]*Fachbereich C Physik, Bergische Universität Wuppertal, Wuppertal, Germany*
[177]*Department of Physics, Yale University, New Haven, Connecticut, USA*
[178]*Yerevan Physics Institute, Yerevan, Armenia*
[179]*Centre de Calcul de l'Institut National de Physique Nucléaire et de Physique des Particules (IN2P3), Villeurbanne, France*

[a]Deceased.
[b]Also at Department of Physics, King's College London, London, United Kingdom.
[c]Also at Institute of Physics, Azerbaijan Academy of Sciences, Baku, Azerbaijan.
[d]Also at Particle Physics Department, Rutherford Appleton Laboratory, Didcot, United Kingdom.
[e]Also at TRIUMF, Vancouver BC, Canada.
[f]Also at Department of Physics, California State University, Fresno CA, United States of America.
[g]Also at Tomsk State University, Tomsk, Russia.
[h]Also at CPPM, Aix-Marseille Université and CNRS/IN2P3, Marseille, France.
[i]Also at Università di Napoli Parthenope, Napoli, Italy.

[j]Also at Institute of Particle Physics (IPP), Canada.
[k]Also at Department of Physics, St. Petersburg State Polytechnical University, St. Petersburg, Russia.
[l]Also at Chinese University of Hong Kong, China.
[m]Also at Department of Financial and Management Engineering, University of the Aegean, Chios, Greece.
[n]Also at Louisiana Tech University, Ruston LA, United States of America.
[o]Also at Institucio Catalana de Recerca i Estudis Avancats, ICREA, Barcelona, Spain.
[p]Also at Institute of Theoretical Physics, Ilia State University, Tbilisi, Georgia.
[q]Also at CERN, Geneva, Switzerland.
[r]Also at Ochadai Academic Production, Ochanomizu University, Tokyo, Japan.
[s]Also at Manhattan College, New York NY, United States of America.
[t]Also at Novosibirsk State University, Novosibirsk, Russia.
[u]Also at Institute of Physics, Academia Sinica, Taipei, Taiwan.
[v]Also at LAL, Université Paris-Sud and CNRS/IN2P3, Orsay, France.
[w]Also at Academia Sinica Grid Computing, Institute of Physics, Academia Sinica, Taipei, Taiwan.
[x]Also at Laboratoire de Physique Nucléaire et de Hautes Energies, UPMC and Université Paris-Diderot and CNRS/IN2P3, Paris, France.
[y]Also at School of Physical Sciences, National Institute of Science Education and Research, Bhubaneswar, India.
[z]Also at Dipartimento di Fisica, Sapienza Università di Roma, Roma, Italy.
[aa]Also at Moscow Institute of Physics and Technology State University, Dolgoprudny, Russia.
[bb]Also at Section de Physique, Université de Genève, Geneva, Switzerland.
[cc]Also at Department of Physics, The University of Texas at Austin, Austin TX, United States of America.
[dd]Also at International School for Advanced Studies (SISSA), Trieste, Italy.
[ee]Also at Department of Physics and Astronomy, University of South Carolina, Columbia SC, United States of America.
[ff]Also at School of Physics and Engineering, Sun Yat-sen University, Guangzhou, China.
[gg]Also at Faculty of Physics, M. V. Lomonosov Moscow State University, Moscow, Russia.
[hh]Also at Moscow Engineering and Physics Institute (MEPhI), Moscow, Russia.
[ii]Also at Institute for Particle and Nuclear Physics, Wigner Research Centre for Physics, Budapest, Hungary.
[jj]Also at Department of Physics, Oxford University, Oxford, United Kingdom.
[kk]Also at Department of Physics, Nanjing University, Jiangsu, China.
[ll]Also at Institut für Experimentalphysik, Universität Hamburg, Hamburg, Germany.
[mm]Also at Department of Physics, The University of Michigan, Ann Arbor MI, United States of America.
[nn]Also at Discipline of Physics, University of KwaZulu-Natal, Durban, South Africa.
[oo]Also at University of Malaya, Department of Physics, Kuala Lumpur, Malaysia.